The Mean First-Reaction Time on a Thin Filament in a 3-D Domain

Denis S. Grebenkov [*], Theodore Kolokolnikov [†], Alan E. Lindsay [‡§], Michael J. Ward [¶]

October 28, 2026

Abstract

We study the mean first-reaction time (MFRT) of a Brownian particle in a bounded three-dimensional domain Ω with a reflecting boundary $\partial\Omega$, that contains a thin reactive filament. The filament is a tube of cross-sectional diameter $\varepsilon \ll 1$ around a smooth closed curve Γ, and its surface is partially reactive with reactivity b. As $\varepsilon \to 0$ the filament reduces to a line source in the outer problem. Its cross-section enters only through a logarithmic reactive capacitance $d_c(b)$, so that the MFRT is $\mathcal{O}(-\log[\varepsilon d_c])$. This contrasts with the $\mathcal{O}(\varepsilon^{-1})$ scaling for spatially localized traps of radius ε. Using matched asymptotic expansions, we derive a Fredholm integral equation on Γ for the line density of the reactive flux. It sums all powers of $\nu \equiv -1/\log[\varepsilon d_c]$ and involves two geometric quantities: the regular part R of the Neumann Green's function, which encodes the interaction of Γ with $\partial\Omega$, and an intrinsic self-energy of Γ that depends only on its shape. The framework extends to multiple filaments, splitting probabilities, a spatially heterogeneous diffusivity, and the principal eigenvalue of the Laplacian. For the unit sphere we solve the integral equation with a simple trapezoidal Nyström scheme, and we validate the predictions for rings, linked rings and torus knots against full 3-D finite-element solutions. For an equatorial ring we obtain the MFRT in closed form and determine the optimal ring radius. We compare it with the optimal radius for N small targets equally spaced on a ring. Finally, we show that fragmenting a filament into N small microtraps is asymptotically equivalent to a continuous filament with an effective radius determined by a periodic capacitance problem. This result connects the logarithmic scaling of filaments to the algebraic scaling of point-like traps.

Key words: Matched asymptotic expansions, filament, Neumann Green's function, mean first-reaction time, intrinsic self-energy, integral equation, logarithmic reactive capacitance.

1 Introduction

The first time a diffusing particle or agent hits a reactive target is a fundamental quantity with applications in ecology, cell biology and physics [14, 28, 57]. In a cellular setting, the diffusing agent may be a signaling molecule that is transported by diffusion to a reactive site (e.g. receptor) to complete or initiate a biological event [3, 7, 9, 21, 56]. In an ecological setting, first passage time theory is an essential tool for characterizing the time needed for individuals to find a mate, food or refuge.

[*]Laboratoire de Physique de la Matiére Condensée, CNRS – Ecole Polytechnique, Institut Polytechnique de Paris, 91120 Palaiseau, France. Email: denis.grebenkov@polytechnique.edu

[†]Dept. of Mathematics, Dalhousie University, Halifax, Nova Scotia, B3H 4R2, Canada. Email: tkolokol@mathstat.dal.ca

[‡]NSF-Simons National Institute for Theory and Mathematics in Biology, Chicago IL.

[§]Dept. of Applied and Computational Mathematics and Statistics, University of Notre Dame, Notre Dame, IN, 46556, USA. Email: a.lindsay@nd.edu

[¶]Department of Mathematics, University of British Columbia, Vancouver, British Columbia, V6T 1Z2, Canada. Email: ward@math.ubc.ca (corresponding author)

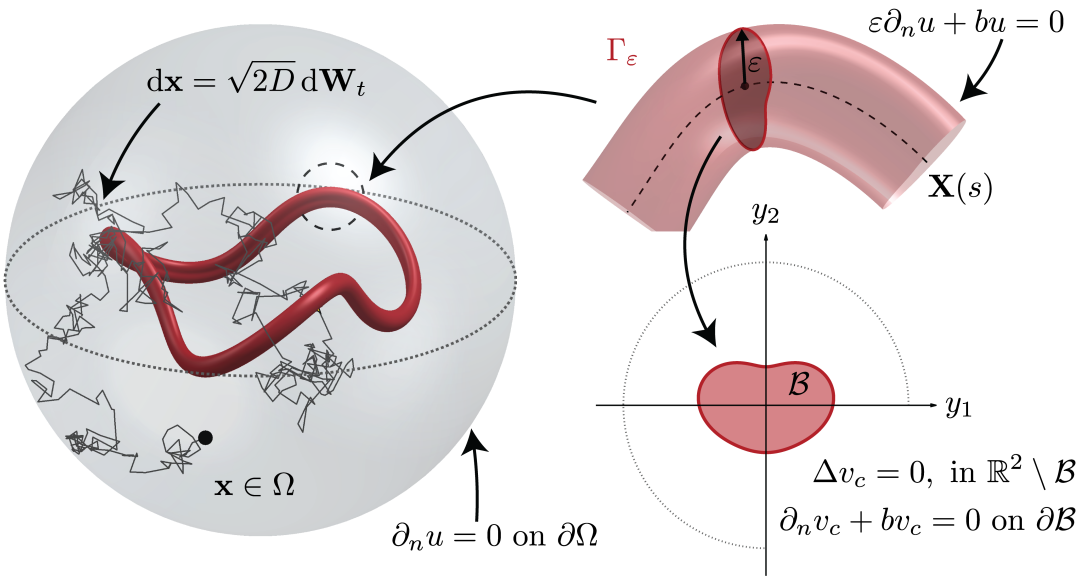


Figure 1: Illustration of the considered first-reaction problem of a 3-D Brownian particle on a thin closed filament Γ_ε. The enclosing region $\Omega \subset \mathbb{R}^3$ has reflecting boundary conditions on $\partial\Omega$. The centerline of the filament is given by a simple curve $\boldsymbol{X}(s)$ and the fixed cross-sectional rescaled profile is given by $\mathcal{B}$.

In many of these examples the reactive sites are small regions centered on fixed separated points. Examples include receptors on the cell membrane [16, 43] or trafficking by nuclear pore complexes, the small apertures on the nucleus whose role is to transport cargo between the cytoplasm and nucleoplasm [4, 34, 35]. When the target regions are small balls centered around fixed points, an extensive literature determining the arrival statistics of diffusing molecules exists [3, 6, 40, 41, 46, 55, 56].

In this work we develop an extension of this theory to a class of important biological structures characterized by elongated, thin targets. Prominent examples include microtubule filaments, actin fibers and strands of DNA [8, 15, 47, 49, 52]. Related studies of ecological-scale transport have examined how arrival statistics are influenced by linear features such as roads, utility lines or fire breaks [19, 33, 48]. In 3-D problems in cell biology, these filamentous structures provide essential functionality by modulating search and signaling processes [38, 51]. The goal of this paper is to present an asymptotic analysis of the 3-D mean first-reaction time of a diffusing molecule to thin closed filaments in the limit of vanishing width. Before stating our main results, we describe the geometric scenario under consideration.

We let $\Omega \subset \mathbb{R}^3$ be a bounded domain with smooth reflecting boundary $\partial\Omega$, and we let $\Gamma \subset \Omega$ be a smooth simple closed curve parameterized in terms of arclength s as $\mathbf{X}(s)$, where $s \in [0, L)$ and $L = |\Gamma|$ is the length of the curve (see Fig. 1). The curve is assumed to lie completely within Ω in the sense that $\mathrm{dist}(\Gamma, \partial\Omega) = \mathcal{O}(1)$. Around Γ we place a reactive thin filament of diameter $\mathcal{O}(\varepsilon)$ with a specified cross-sectional shape $\mathcal{B}_\varepsilon$. We assume the filament is well separated from itself, in the sense that if two points $\mathbf{X}(s)$ and $\mathbf{X}(s')$ are separated by an $\mathcal{O}(1)$ arclength along Γ, then $|\mathbf{X}(s) - \mathbf{X}(s')| = \mathcal{O}(1)$. To characterize the tubular geometry around Γ we introduce the so-called Bishop frame [5, 32] which is used extensively in slender body theory [39, 50, 53, 54]. We let $\mathbf{T}(s) = \mathbf{X}'(s)$ be the unit tangent vector of the centerline and

we define two unit vectors $\mathbf{M}_1(s)$ and $\mathbf{M}_2(s)$ in the plane orthogonal to $\mathbf{T}(s)$, so that $\{\mathbf{T}(s), \mathbf{M}_1(s), \mathbf{M}_2(s)\}$ form an orthonormal basis. To ensure that the reference frame along the curve does not twist, we enforce that $\mathbf{M}_1'(s)\cdot\mathbf{M}_2(s) = 0$ and $\mathbf{M}_2'(s)\cdot\mathbf{M}_1(s) = 0$. The reactive filament is locally defined by

$$\Gamma_\varepsilon = \left\{ \mathbf{X}(s) + \eta_1 \mathbf{M}_1(s) + \eta_2 \mathbf{M}_2(s) \in \mathbb{R}^3 \;\middle|\; s \in [0, L),\ (\eta_1, \eta_2) \in \mathcal{B}_\varepsilon \right\} . \tag{1.1}$$

The mean first-reaction time (MFRT) $u(\mathbf{x})$ of a particle, initially at position $\mathbf{x} \in \Omega \backslash \Gamma_\varepsilon$, undergoing Brownian motion with diffusivity D, with a reactive filament Γ_ε satisfies

$$\Delta_{\mathbf{x}} u = -\frac{1}{D}, \quad \mathbf{x} \in \Omega \setminus \Gamma_\varepsilon, \qquad \varepsilon \partial_n u + b u = 0, \quad \mathbf{x} \in \partial\Gamma_\varepsilon, \qquad \partial_n u = 0, \quad \mathbf{x} \in \partial\Omega . \tag{1.2}$$

Here $b > 0$ is the reactivity of the filament. The strong reaction case $b \gg 1$ results in an instantaneous reaction when the particle reaches Γ_ε while the weak reaction limit $b \ll 1$ requires a particle to spend a long time near Γ_ε for a reaction to occur. The quantity ∂_n denotes the outward normal derivative. The global MFRT (GMFRT) is defined as the spatially averaged MFRT over a uniform distribution of the initial point,

$$\bar{u} = \frac{1}{|\Omega \setminus \Gamma_\varepsilon|} \int_{\Omega \setminus \Gamma_\varepsilon} u(\mathbf{x}) \, \mathrm{d}\mathbf{x} . \tag{1.3}$$

We will use the method of matched asymptotic expansions to analyze (1.2) in the limit $\varepsilon \to 0$ of small filament diameter and determine $\bar{u}$. Our asymptotic analysis leads to a Fredholm integral equation of the second kind for the strength of a line singularity, which we refer to as the line density supported on Γ, and a coupling condition to determine $\bar{u}$. The derivation of our integral equation for the line density involves the Neumann Green's function $G(\mathbf{x}; \boldsymbol{\xi})$ in Ω, which for $\boldsymbol{\xi} \in \Omega$ is given as the unique solution to

$$\Delta_{\mathbf{x}} G = \frac{1}{|\Omega|} - \delta(\mathbf{x} - \boldsymbol{\xi}), \quad \mathbf{x} \in \Omega ; \qquad \partial_n G = 0, \quad \mathbf{x} \in \partial\Omega ; \qquad \int_\Omega G(\mathbf{x}; \boldsymbol{\xi}) \, \mathrm{d}\mathbf{x} = 0 . \tag{1.4a}$$

It can be decomposed into a singular part and a smooth regular part $R(\mathbf{x}; \boldsymbol{\xi})$ as

$$G(\mathbf{x}; \boldsymbol{\xi}) = \frac{1}{4\pi |\mathbf{x} - \boldsymbol{\xi}|} + R(\mathbf{x}; \boldsymbol{\xi}) . \tag{1.4b}$$

The Neumann Green's function is known analytically when Ω is a sphere [13] and can be computed numerically for general shapes [12, 44]. In terms of this Neumann Green's function, in Sec. 2 we use inner-outer asymptotic matching to show that the line density and the GMFRT $\bar{u}$ are determined in terms of the solution to a Fredholm integral equation defined over the centerline Γ of the filament.

As an example of our results, we derive in Sec. 2.3 the behavior of the GMFRT for a single reactive filament to be

$$\bar{u} \sim \frac{|\Omega|}{2\pi D |\Gamma|} \left(-\log[\varepsilon d_c(b)] + \frac{2\pi}{|\Gamma|} \int_\Gamma \int_\Gamma R\left(\mathbf{X}(s); \mathbf{X}(s')\right) \, \mathrm{d}s \, \mathrm{d}s' + \frac{1}{2|\Gamma|} \int_\Gamma \mathcal{E}(s) \, \mathrm{d}s + \mathcal{O}(\nu) \right) , \qquad \nu = \frac{-1}{\log[\varepsilon d_c]}, \tag{1.5}$$

as $\varepsilon \to 0$. Here d_c is the logarithmic reactive capacitance, which is equal to $e^{-1/b}$ for a circular cross-section. For general cross-sectional profiles $\mathcal{B}$ and reactivities b, we provide in Appendix A an algorithm to calculate d_c. A notable feature of (1.5) is the scaling law $\bar{u} = \mathcal{O}(\log \varepsilon)$ as $\varepsilon \to 0$, which is the typical 2-D scaling law for point absorbers [40], and not the $\bar{u} = \mathcal{O}(\varepsilon^{-1})$ behavior associated with absorbers centered around discrete points in 3-D domains [13]. In (1.5) the term $\int_\Gamma \int_\Gamma R\left(\mathbf{X}(s); \mathbf{X}(s')\right) \, \mathrm{d}s \, \mathrm{d}s'$ describes the interaction of

the filament with the domain Ω while $\int_\Gamma \mathcal{E}(s)\,\mathrm{d}s$ describes the interaction of the filament with itself through an *intrinsic self-energy* term $\mathcal{E}(s)$ that we define in (2.17) and which depends only on Γ.

Our approach parallels slender-body theory for potential and Stokes flow [2, 31, 37], in which a thin body is replaced by a line distribution of singularities whose strength satisfies an integral equation with a local logarithmic term and a nonlocal interaction along the centerline; see [39, 50, 53] for its rigorous justification and connection to boundary integral methods. We remark that in [24] and [23] a finite element method was used to numerically compute solutions to Poisson-type problems with pre-specified line densities after analytically extracting an appropriate singular behavior from the solution to be computed.

In Sec. 2.4 we extend the analysis to N disjoint filaments $\Gamma_{\varepsilon,j}$ with centerlines Γ_j of length L_j, cross-sections $\mathcal{B}_j$ and reactivities b_j. Our main result (Proposition 3) is that $\bar{u} \sim \chi$ and away from the filaments, the solution of (1.2) is given by

$$u(\mathbf{x}) \sim \chi - 2\pi \sum_{j=1}^{N} \int_{\Gamma_j} A_j(s)\, G(\mathbf{x}; \mathbf{X}_j(s))\, \mathrm{d}s, \qquad \mathrm{dist}(\mathbf{x}, \Gamma_j) \gg \varepsilon, \quad j = 1, \ldots, N.$$

The line densities $A_j(s)$ on Γ_j and the constant χ solve the coupled system

$$\mathcal{K}_j A_j + \sum_{\substack{i=1 \\ i \neq j}}^{N} \mathcal{G}_{ji} A_i = \chi\,, \quad j = 1, \ldots, N\,; \qquad \sum_{j=1}^{N} \int_{\Gamma_j} A_j(s)\, \mathrm{d}s = \frac{|\Omega|}{2\pi D}\,. \tag{1.6}$$

The self-interaction operator $\mathcal{K}_j$ on Γ_j and the coupling operator $\mathcal{G}_{ji}$ between filaments Γ_i and Γ_j are

$$(\mathcal{K}_j A)(s) \equiv \Big(\frac{1}{\nu_j} + \frac{\mathcal{E}_j(s)}{2}\Big) A(s) - \frac{1}{2} \int_{\Gamma_j} \frac{A(s) - A(s')}{|\mathbf{X}_j(s) - \mathbf{X}_j(s')|}\, \mathrm{d}s' + 2\pi \int_{\Gamma_j} A(s')\, R\big(\mathbf{X}_j(s); \mathbf{X}_j(s')\big)\, \mathrm{d}s'\,, \tag{1.7a}$$

$$(\mathcal{G}_{ji} A)(s) \equiv 2\pi \int_{\Gamma_i} A(s')\, G\big(\mathbf{X}_j(s); \mathbf{X}_i(s')\big)\, \mathrm{d}s'\,, \tag{1.7b}$$

with $\nu_j = -1/\log[\varepsilon d_c(b_j)]$ and $\mathcal{E}_j$ the intrinsic self-energy of Γ_j. The local term $1/\nu_j$ carries information on the cross-sectional profile $\mathcal{B}_j$ and reactivity b_j and the self-energy terms are determined by the shape of Γ_j. The terms involving R and G encode information on a filament's interaction with the domain and with each other, respectively. The line density $A_j(s)$ represents the local flux arriving at the cross-section of the filament j at s.

The methods we develop here can be applied to several related problems in first passage time theory. For example, the so called *splitting probability* $\phi_k(\mathbf{x})$ is defined as the probability that a searcher starting at $\mathbf{x}$ is absorbed by filament k before any other and it has been used extensively in source detection and signaling problems [18, 43, 45]. The splitting probabilities satisfy the elliptic problem,

$$\Delta \phi_k = 0\,, \quad \mathbf{x} \in \Omega \setminus \cup_{j=1}^{N} \Gamma_{\varepsilon,j}\,; \qquad \partial_n \phi_k = 0\,, \quad \mathbf{x} \in \partial\Omega\,, \tag{1.8a}$$

$$\varepsilon \partial_n \phi_k + b_j\,(\phi_k - \delta_{jk}) = 0\,, \qquad \mathbf{x} \in \partial\Gamma_{\varepsilon,j}\,, \quad j \in \{1, \ldots, N\}\,, \tag{1.8b}$$

with $\phi_k = \delta_{jk}$ on $\partial\Gamma_{\varepsilon,j}$ when $b_j = \infty$ and where δ_{jk} is the Kronecker symbol. In Sec. 2.5, we derive an asymptotic solution (Proposition 4) to (1.8) in the limit as $\varepsilon \to 0$ in which the solution is expressed in terms of densities supported over the centerlines Γ_j for $j = 1, \ldots, N$ which solve a system related (1.6) but with a modified right-hand side.

In Sec. 3 we analyze scenarios where the bounding domain is a sphere and the filaments are arranged circular rings of radius $0 < r_0 < 1$. In the case of a single ring centered at the origin, or two rings arranged symmetrically on the planes $z = \pm z_0$, we are able to solve the integral system in closed form. In doing so, we identify GMFRT optimizing configurations at finite r_0 values where r_0 is the radius of the rings.

In Sec. 4, we describe an implementation of the trapezoidal rule to discretize and solve the coupled integral equation system (1.6). The accuracy of the expansions is confirmed by full finite element solutions of the $\varepsilon > 0$ problems (1.2) and (1.8). We show results on several non-ring filaments and identify shielding behavior, in which distal sections of highly undulating filaments exhibit locally reduced capture rates.

In Sec. 5, we demonstrate the potential for our approach to extend to related problems in capture theory. One such problem concerns the determination of the MFRT $u(\mathbf{x})$ when the environment has a spatially varying diffusivity $D(\mathbf{x}) > 0$ (see [42]). In Sec. 5.1, we consider the problem (assuming an Itô interpretation)

$$\Delta u = -\frac{1}{D(\mathbf{x})}\,, \quad \mathbf{x} \in \Omega \setminus \Gamma_\varepsilon\,; \qquad \varepsilon \partial_n u + bu = 0\,, \quad \mathbf{x} \in \partial\Gamma_\varepsilon\,; \qquad \partial_n u = 0\,, \quad \mathbf{x} \in \partial\Omega\,. \tag{1.9}$$

We determine in the limit as $\varepsilon \to 0$ a corresponding reduction of (1.9) to an integral equation supported on the filament centerline. A second problem considered is the determination of the principal eigenvalue λ_0 and eigenfunction $u_0(\mathbf{x})$ of the Laplacian for a domain with a reactive filament. These quantities solve

$$\Delta u_0 + \lambda_0 u_0 = 0\,, \quad \mathbf{x} \in \Omega \setminus \Gamma_\varepsilon\,; \qquad \varepsilon \partial_n u_0 + b u_0 = 0\,, \quad \mathbf{x} \in \partial\Gamma_\varepsilon\,; \qquad \partial_n u_0 = 0\,, \quad \mathbf{x} \in \partial\Omega\,. \tag{1.10}$$

The principal eigenvalue is simple (multiplicity 1) and the corresponding eigenfunction can be chosen positive. The survival probability of the Brownian particle is proportional to $e^{-D\lambda_0 t}$ and so $D\lambda_0 \propto 1/\bar{u}$. In Sec. 5.2 we derive a log-summed expansion of solutions to (1.10) which is accurate to all orders in $\nu = -1/\log[\varepsilon d_c]$. This result is a hybrid numerical asymptotic solution formulated in terms of a nonlinear problem for λ_0 involving the associated Helmholtz Green's function. A two-term expansion of λ_0 and the associated eigenfunction in terms of ν is developed that gives an explicit, but slower converging expression involving the Neumann Green's function (1.4).

In Sec. 6 we investigate the fragmentation of a single absorbing filament into multiple absorbing micro-traps. We derive and solve a new periodic capacitance problem, which captures the transition between the $\bar{u} = \mathcal{O}(\log \varepsilon)$ scaling behavior of the MFRT with an absorbing filament and a $\bar{u} = \mathcal{O}(\sigma^{-1})$ scaling regime of the MFRT with multiple point absorbers of radius $\mathcal{O}(\sigma)$. Finally, in Sec. 7, we summarize results and discuss a few avenues for future study arising from this work.

2 Asymptotic reduction to an integral equation

2.1 Inner solution

We first consider the inner (or local) solution for (1.2) near the filament. In terms of the tubular coordinate system (1.1), the Laplacian of an arbitrary function $\Phi(\mathbf{x})$ transforms to (see Appendix A and [32])

$$\Delta_{\mathbf{x}}\Phi = (\partial_{\eta_1\eta_1} + \partial_{\eta_2\eta_2})\,\Phi - \frac{\kappa_1}{h_s}\partial_{\eta_1}\Phi - \frac{\kappa_2}{h_s}\partial_{\eta_2}\Phi + \frac{1}{h_s^2}\partial_{ss}\Phi + \frac{1}{h_s^3}\left(\eta_1\kappa_1' + \eta_2\kappa_2'\right)\partial_s\Phi\,, \tag{2.1}$$

where the scale factor is $h_s = 1 - \kappa_1\eta_1 - \kappa_2\eta_2$. Here $\kappa_1 = \kappa_1(s)$ and $\kappa_2 = \kappa_2(s)$ are the curvatures along each respective normal direction, defined by $\mathbf{M}_1'(s) = -\kappa_1(s)\mathbf{T}(s)$ and $\mathbf{M}_2'(s) = -\kappa_2(s)\mathbf{T}(s)$, where $\mathbf{T}(s) = \mathbf{X}'(s)$

is the unit tangent along the filament centerline. A sufficient condition for this local description to be valid all along the filament is that $\sqrt{\eta_1^2+\eta_2^2} < 1/\kappa(s)$ for $0 \le s \le L$, where $\kappa(s) \equiv \sqrt{\kappa_1^2+\kappa_2^2} = |\mathbf{X}''(s)|$ is the curvature of the filament centerline.

Upon re-scaling the normal plane by ε by defining $y_1 = \eta_1/\varepsilon$ and $y_2 = \eta_2/\varepsilon$, and labeling the inner variable $\mathbf{y} = (y_1, y_2)^T$ and $|\mathbf{y}| = \rho \equiv \sqrt{y_1^2+y_2^2}$, we use (2.1) to obtain that the MFRT in (1.2) near the filament, written as $v(y_1, y_2, s)$ in the inner variables, satisfies

$$\Delta_{\mathbf{x}} u = \frac{1}{\varepsilon^2}\Delta_{\mathbf{y}} v - \frac{\kappa_1}{\varepsilon} v_{y_1} - \frac{\kappa_2}{\varepsilon} v_{y_2} + \mathcal{O}(1) = -\frac{1}{D}\,. \tag{2.2}$$

As a result, by expanding $v = v_0 + \varepsilon v_1 + \ldots$, we obtain that the local solution near the filament is a 2-D harmonic solution $\Delta_{\mathbf{y}} v_0 = 0$. In terms of the local variable $\mathbf{y}$, we denote the rescaled filament cross-section as $\mathcal{B} \equiv \mathcal{B}_\varepsilon/\varepsilon$.

The canonical inner problem associated with the filament cross-section is, at each point s on Γ, the following exterior problem in $\mathbb{R}^2$ for $v_c(\mathbf{y})$, which is made unique by prescribing a unit logarithmic growth at infinity:

$$\begin{gathered} \Delta_{\mathbf{y}} v_c = 0\,, \quad \mathbf{y} \in \mathbb{R}^2 \setminus \mathcal{B}\,, \\ \partial_n v_c + b v_c = 0\,, \quad \mathbf{y} \in \partial\mathcal{B}\,; \qquad v_c \sim \log|\mathbf{y}| - \log\left[d_c(b)\right] + o(1)\,, \quad \text{as} \quad |\mathbf{y}| \to \infty\,, \end{gathered} \tag{2.3}$$

where ∂_n points into $\mathcal{B}$. We refer to the constant $d_c(b)$ as the *logarithmic reactive capacitance* of $\mathcal{B}$.

We remark that since the filament has a uniform cross-section, the rescaled shape $\mathcal{B}$ and hence $d_c(b)$ is independent of the position s along the filament centerline. In addition, since $d_c(b)$ is invariant under rotations of $\mathcal{B}$, we can allow for the filament centerline $\mathbf{X}(s)$ to exhibit twist, without influencing $d_c(b)$.

Only for a few special cases is $d_c(b)$ known analytically. When $\mathcal{B}$ is the unit disk we have $d_c(b) = e^{-1/b}$. When $b = \infty$, $d_c(\infty)$ can be determined in terms of the conformal map of $\mathcal{B}$ to the unit disk. In Table 1 of [41] explicit formulas for $d_c(\infty)$ are given for various simple choices of $\mathcal{B}$. However, no such results are typically available for finite reactivities for non-circular shapes. In Appendix §A.1 we provide a methodology to numerically determine $d_c(b)$ from a Steklov eigenfunction representation, as well as its behavior for $b \ll 1$.

In terms of the canonical solution v_c, the leading-order inner solution is taken as

$$v_0 = A(s) v_c\,, \tag{2.4}$$

for some strength $A(s)$ that depends on the position along the filament, and which must be determined by matching to the outer solution. In this way, the far-field behavior of the inner solution, written in the outer variable $\mathbf{y} = \boldsymbol{\eta}/\varepsilon$, is

$$v = A(s)\left(\log\left(|\boldsymbol{\eta}|/\varepsilon\right) - \log\left[d_c(b)\right]\right) + o(1) = A(s)\log|\boldsymbol{\eta}| + A(s)/\nu + o(1)\,, \quad \text{where} \quad \nu \equiv -1/\log[\varepsilon d_c(b)]\,. \tag{2.5}$$

By applying the 2-D divergence theorem on (2.3) we identify that

$$A(s) = -\frac{1}{2\pi}\int_{\partial\mathcal{B}} \partial_n v_0 \,\mathrm{d}\ell\,, \tag{2.6}$$

where $\mathrm{d}\ell$ represents arclength along $\partial\mathcal{B}$. The far-field behavior (2.5) will provide the matching condition for the outer solution constructed in §2.2.

To interpret the role of $A(s)$, we estimate the diffusive flux J into the filament through its boundary. In terms of the tubular coordinates (1.1), and where ℓ_ε denotes arclength along $\partial\mathcal{B}_\varepsilon$, we have

$$J = \int_{\partial\Gamma_\varepsilon} (-D\partial_n u)\,\mathrm{d}S = -D\int_\Gamma \left(\int_{\partial\mathcal{B}_\varepsilon} (1-\kappa_1(s)\eta_1 - \kappa_2(s)\eta_2)\,\partial_\eta u\,\mathrm{d}\ell_\varepsilon\right)\mathrm{d}s\,, \tag{2.7}$$

where the curvature terms arise from the Jacobian between tubular and Cartesian coordinates. In terms of the inner variables $y_1 = \eta_1/\varepsilon$, $y_2 = \eta_2/\varepsilon$, $d\ell_\varepsilon = \varepsilon d\ell$, $v \sim v_0$, $\partial_\eta = \varepsilon^{-1}\partial_n$, and using (2.6) in (2.7), we obtain to leading-order, after neglecting the $\mathcal{O}(\varepsilon)$ curvature terms in (2.7), that

$$J \sim -D\int_\Gamma \left(\int_{\partial\mathcal{B}} \partial_n v_0\,\mathrm{d}\ell\right)\mathrm{d}s = 2\pi D\int_\Gamma A(s)\,\mathrm{d}s\,. \tag{2.8}$$

This relates the total flux across the boundary of the filament to a line integral of the unknown $A(s)$ along the filament centerline.

Finally, we remark that if the filament has a variable cross-section and non-uniform reactivity along the filament centerline, then we need only replace $b = b(s)$ and $\partial\mathcal{B} = \partial\mathcal{B}(s)$ in (2.3) to obtain a parameterized 2-D inner problem, for which $d_c = d_c(s)$ can be readily computed numerically at each fixed s using the Steklov methodology in Appendix A.1. We will not pursue this simple generalization of our theory in the analysis below.

2.2 Outer solution

In the limit $\varepsilon \to 0$, the filament shrinks to its centerline: $\Gamma_\varepsilon \to \Gamma$. As a result, the outer solution exhibits a line singularity of strength $A(s)$ to be determined self-consistently. In other words, when $\mathbf{x}$ approaches any point of Γ, the solution becomes singular. A common way to incorporate such a line singularity on the "degenerate boundary" Γ consists in introducing Dirac δ sources along Γ:

$$\Delta_{\mathbf{x}} u = -\frac{1}{D} + 2\pi\int_\Gamma A(s')\delta(\mathbf{x}-\mathbf{X}(s'))\,\mathrm{d}s'\,, \quad \mathbf{x}\in\Omega\setminus\Gamma\,; \qquad \partial_n u = 0\,, \quad \mathbf{x}\in\partial\Omega\,, \tag{2.9a}$$

where we refer to $A(s)$ as the *line density*. In this way, upon matching the far-field behavior (2.5) of the inner solution near the filament to the outer solution, defined at $\mathcal{O}(1)$ distances from the filament, we obtain

$$u - A(s)\log|\mathbf{x}-\mathbf{X}(s)| \to \frac{A(s)}{\nu} \quad \text{as} \quad \mathbf{x}\to\mathbf{X}(s)\,, \quad s\in[0,L]\,. \tag{2.9b}$$

The specification of the regular part of the singularity behavior in (2.9b) is a constraint that will yield an integral equation $A(s)$ that is accurate to all orders in the logarithmic gauge $\nu = -1/\log[\varepsilon d_c]$.

Upon applying the divergence theorem to (2.9a) we derive that

$$-\frac{|\Omega|}{D} + 2\pi\int_\Gamma A(s')\left(\int_\Omega \delta\big(\mathbf{x}-\mathbf{X}(s')\big)\,\mathrm{d}\mathbf{x}\right)\mathrm{d}s' = 0\,,$$

which provides the constraint

$$\int_\Gamma A(s)\,\mathrm{d}s = \frac{|\Omega|}{2\pi D}\,. \tag{2.10}$$

Assuming that (2.10) holds, we now represent the solution to (2.9) in terms of the Neumann Green's function G of (1.4). By using Green's second identity we derive that

$$0 = \int_\Omega (G\Delta_{\mathbf{x}'}u - u\Delta_{\mathbf{x}'}G)\ \mathrm{d}\mathbf{x}' = -\frac{1}{D}\int_\Omega G(\mathbf{x}';\mathbf{x})\,\mathrm{d}\mathbf{x}' + 2\pi\int_\Gamma A(s')\left(\int_\Omega G(\mathbf{x}';\mathbf{x})\delta(\mathbf{x}'-\mathbf{X}(s'))\,\mathrm{d}\mathbf{x}'\right)\ \mathrm{d}s' - \frac{1}{|\Omega|}\int_\Omega u(\mathbf{x}')\,\mathrm{d}\mathbf{x}' + u(\mathbf{x})\,.$$

Since $G(\mathbf{x}';\mathbf{x}) = G(\mathbf{x};\mathbf{x}')$ and $\int_\Omega G(\mathbf{x};\mathbf{x}')\ \mathrm{d}\mathbf{x} = 0$, we obtain in terms of an unknown constant χ that

$$u(\mathbf{x}) = \chi - 2\pi\int_\Gamma A(s')G(\mathbf{x};\mathbf{X}(s'))\,\mathrm{d}s'\,, \quad \text{for} \quad \mathbf{x}\notin\Gamma\,. \tag{2.11}$$

Since the volume of the filament Γ_ε is $\mathcal{O}(\varepsilon^2)$, and $\int_\Omega G(\mathbf{x};\mathbf{x}')\ \mathrm{d}\mathbf{x} = 0$, we conclude from (1.3) and (2.11) that the *global MFRT* is

$$\bar{u} = \chi + o(1). \tag{2.12}$$

The order of the error estimate in (2.12) arises from neglecting the effect of the $\mathcal{O}(\varepsilon)$ curvature correction in the inner region.

Next, we will derive an integral equation formulation for $A(s)$ and the constant χ by ensuring that the regular part of the singularity structure in (2.9b) is satisfied.

To do so, we use (1.4b) to isolate the singular part of G. Upon substituting (1.4b) into (2.11) we obtain that

$$u(\mathbf{x}) = \chi - \frac{1}{2}\int_\Gamma \frac{A(s')}{|\mathbf{x}-\mathbf{X}(s')|}\,\mathrm{d}s' - 2\pi\int_\Gamma A(s')R(\mathbf{x};\mathbf{X}(s'))\,\mathrm{d}s'\,, \quad \text{for} \quad \mathbf{x}\notin\Gamma\,. \tag{2.13}$$

We now let $\mathbf{X}(s)$ be any target point on Γ and we let $\mathbf{x} = \mathbf{X}_\eta(s)$ be any point at a distance η from $\mathbf{X}(s)$ in the normal plane to Γ at $\mathbf{X}(s)$. In the limit $\eta\to 0$, we observe that the second integral in (2.13) has a well-defined limit, while the first integral is divergent. As such, we write $A(s') = (A(s')-A(s)) + A(s)$ in (2.13) in order to obtain an integrand with a removable singularity. Therefore, as $\mathbf{x} = \mathbf{X}_\eta(s)\to\mathbf{X}(s)$ we have

$$u(\mathbf{x}) \sim \chi - \frac{A(s)}{2}\left(\int_\Gamma \frac{1}{|\mathbf{x}-\mathbf{X}(s')|}\,\mathrm{d}s'\right) + \frac{1}{2}\int_\Gamma \frac{A(s)-A(s')}{|\mathbf{X}(s)-\mathbf{X}(s')|}\,\mathrm{d}s' - 2\pi\int_\Gamma A(s')R(\mathbf{X}(s);\mathbf{X}(s'))\,\mathrm{d}s'\,. \tag{2.14}$$

In Appendix B we establish the leading-order singular behavior

$$\int_\Gamma \frac{\mathrm{d}s'}{|\mathbf{X}_\eta(s)-\mathbf{X}(s')|} \sim -2\log\eta + \mathcal{O}(1)\,, \quad \text{as} \quad \eta\to 0\,. \tag{2.15}$$

As a result, we conclude that (2.14) has the following asymptotic behavior as $\mathbf{X}_\eta(s)\to\mathbf{X}(s)$:

$$u \sim A(s)\log\eta + \chi - \frac{1}{2}A(s)\mathcal{E}(s) + \frac{1}{2}\int_\Gamma \frac{A(s)-A(s')}{|\mathbf{X}(s)-\mathbf{X}(s')|}\,\mathrm{d}s' - 2\pi\int_\Gamma A(s')R(\mathbf{X}(s);\mathbf{X}(s'))\,\mathrm{d}s'\,. \tag{2.16}$$

Here $\mathcal{E}(s)$, referred to as the *intrinsic self-energy of the curve* Γ, is defined by

$$\mathcal{E}(s) \equiv \lim_{\eta\to 0}\left(\int_\Gamma \frac{\mathrm{d}s'}{|\mathbf{X}_\eta(s)-\mathbf{X}(s')|} + 2\log\eta\right)\,. \tag{2.17}$$

In Appendix B we calculate $\mathcal{E}(s)$ when Γ is a planar loop and we provide a numerical algorithm to compute it for an arbitrary simple closed curve. Finally, to obtain our integral equation for $A(s)$ we enforce from (2.9b) that the limiting behavior in (2.16) must satisfy $u\sim A(s)\log\eta + A(s)/\nu$ as $|\mathbf{X}_\eta(s)-\mathbf{X}(s)| = \eta\to 0$. We summarize our result in the following proposition:

Proposition 1. *Let Γ be any smooth simple closed curve in Ω parameterized by arclength as $\mathbf{X}(s)$, which has an $\mathcal{O}(\varepsilon)$ cross-sectional diameter. In the limit $\varepsilon \to 0$, the asymptotic solution to* (1.2) *in the outer region at $\mathcal{O}(1)$ distances from Γ is*

$$u(\mathbf{x}) \sim \chi - 2\pi \int_\Gamma A(s) G(\mathbf{x}; \mathbf{X}(s))\, \mathrm{d}s\,, \quad \textit{for} \quad \mathbf{x} \notin \Gamma\,, \tag{2.18}$$

where the line density $A(s)$ and the asymptotic approximation χ to the volume-averaged GMFRT $\bar{u}$ are solutions to the integral equation, defined for all $s \in [0, L]$ with $L = |\Gamma|$, by

$$(\mathcal{K}A)(s) \equiv \frac{A(s)}{\nu} + \frac{1}{2} A(s)\mathcal{E}(s) - \frac{1}{2}\int_\Gamma \frac{A(s) - A(s')}{|\mathbf{X}(s) - \mathbf{X}(s')|}\, \mathrm{d}s' + 2\pi \int_\Gamma A(s') R(\mathbf{X}(s); \mathbf{X}(s'))\, \mathrm{d}s' = \chi\,, \tag{2.19}$$

subject to the constraint $\int_\Gamma A(s)\, \mathrm{d}s = |\Omega|/(2\pi D)$. In (2.18) *and* (2.19)*, G is the Neumann Green's function with regular part R satisfying* (1.4)*, while $\mathcal{E}(s)$ is the intrinsic self-energy of Γ defined by* (2.17)*. In addition, $\nu = -1/\log[\varepsilon d_c]$, where $d_c = d_c(b)$ is the logarithmic reactive capacitance of the rescaled cross-sectional shape $\mathcal{B}$ of the filament Γ_ε, as defined by the exterior 2-D problem* (2.3)*.*

We remark that (2.19) is a Fredholm integral equation of the second kind on Γ. By solving (2.19) numerically as $A = A(s;\nu)$ and $\chi = \chi(\nu)$ it effectively sums all powers of the logarithmic gauge function ν. A related approach to sum logarithmic expansions in 2-D domains with spatially localized defects was initially undertaken in [58]. Through the logarithmic reactive capacitance $d_c(b)$, this gauge function encodes the reactivity b of the boundary of the filament and its cross-sectional shape $\mathcal{B}$. Recall that in Appendix A.1 it is shown how to numerically compute $d_c(b)$ by using a Steklov representation. Moreover, in (2.19) we emphasize that $\mathcal{E}(s)$ is independent of the shape of the confining domain Ω and describes only the interaction of the curve Γ with itself. The effect of Ω, and the relative position of Γ within Ω, is encoded in (2.19) by the regular part R of the Neumann Green's function.

2.3 A two-term approximation

We now determine a more explicit two-term asymptotic approximation for χ in powers of ν. To do so, in (2.19) and (2.10) we expand $A(s;\nu)$ and $\chi(\nu)$ as

$$A(s;\nu) = A_0(s) + \nu A_1(s) + \dots\,, \qquad \chi(\nu) = \frac{\chi_0}{\nu} + \chi_1 + \dots\,. \tag{2.20}$$

From the leading terms in (2.19), we obtain that $A_0 = \chi_0$ for all s. From the constraint (2.10), we get

$$A_0 = \chi_0 = \frac{|\Omega|}{2\pi D|\Gamma|}\,. \tag{2.21}$$

At next order, we obtain from (2.19) and (2.10) that

$$\chi_1 = 2\pi A_0 \int_\Gamma R\left(\mathbf{X}(s); \mathbf{X}(s')\right)\, \mathrm{d}s' + A_1(s) + \frac{1}{2} A_0 \mathcal{E}(s)\,, \qquad \int_\Gamma A_1\, \mathrm{d}s = 0\,. \tag{2.22}$$

To isolate the constant χ_1, we integrate the first equation in (2.22) over Γ to conclude that

$$\chi_1 = \frac{A_0}{|\Gamma|}\left(2\pi \int_\Gamma \int_\Gamma R\left(\mathbf{X}(s); \mathbf{X}(s')\right)\, \mathrm{d}s\, \mathrm{d}s' + \frac{1}{2}\int_\Gamma \mathcal{E}(s)\, \mathrm{d}s\right). \tag{2.23}$$

Upon substituting χ_1 back into (2.22), we determine $A_1 = A_1(s)$ as

$$A_1 = -\frac{A_0}{2}\left(\mathcal{E}(s) - \frac{1}{|\Gamma|}\int_\Gamma \mathcal{E}(s)\,\mathrm{d}s\right) - 2\pi A_0\left(\int_\Gamma R\left(\mathbf{X}(s);\mathbf{X}(s')\right)\,\mathrm{d}s' - \frac{1}{|\Gamma|}\int_\Gamma\int_\Gamma R\left(\mathbf{X}(s);\mathbf{X}(s')\right)\,\mathrm{d}s\,\mathrm{d}s'\right), \tag{2.24}$$

where A_0 is given in (2.21). We summarize the results of our two-term expansion for the volume-averaged MFRT χ and the outer solution in (2.18) as follows:

Proposition 2. *In the limit $\nu \to 0$, we have the explicit two-term approximation:*

$$\chi \sim \frac{|\Omega|}{2\pi D|\Gamma|\nu}\left(1 + \frac{2\pi\nu}{|\Gamma|}\int_\Gamma\int_\Gamma R\left(\mathbf{X}(s);\mathbf{X}(s')\right)\,\mathrm{d}s\,\mathrm{d}s' + \frac{\nu}{2|\Gamma|}\int_\Gamma \mathcal{E}(s)\,\mathrm{d}s + \mathcal{O}(\nu^2)\right), \tag{2.25a}$$

where $|\Gamma| = L$. The corresponding outer solution for $\mathbf{x} \notin \Gamma$ is

$$u(\mathbf{x}) \sim \frac{|\Omega|}{2\pi D|\Gamma|\nu}\left(1 + \frac{2\pi\nu}{|\Gamma|}\int_\Gamma\int_\Gamma R\left(\mathbf{X}(s);\mathbf{X}(s')\right)\,\mathrm{d}s\,\mathrm{d}s' + \frac{\nu}{2|\Gamma|}\int_\Gamma \mathcal{E}(s)\,\mathrm{d}s - 2\pi\nu\int_\Gamma G\left(\mathbf{x};\mathbf{X}(s)\right)\,\mathrm{d}s + \mathcal{O}(\nu^2)\right). \tag{2.25b}$$

From (2.25a) we observe that this two-term expansion depends on the average of both the intrinsic self-energy of Γ and of the regular part of the Neumann Green's function.

2.4 Multiple non-intersecting thin filaments

We now extend our asymptotic theory to derive a coupled set of integral equations for the case of multiple non-intersecting simple closed curves.

We let Γ_i for $i \in \{1,\dots,N\}$ be N smooth, simple, and closed non-intersecting curves with $\Gamma_i \subset \Omega$ and $\mathrm{dist}(\Gamma_i,\Gamma_j) > 0$ for $i \neq j$. Each curve Γ_i is parameterized by $\mathbf{X}_i(s_i)$ where s_i with $0 \le s_i \le L_i$, is arclength along Γ_i, and L_i is the length of Γ_i. Each thin filament $\Gamma_{\varepsilon,i}$ around the centerline Γ_i is assumed to have a uniform cross-section $\varepsilon\mathcal{B}_i$ at each $s_i \in [0,L_i]$, but its shape $\mathcal{B}_i$ may be different for each filament. We assume that the boundary of each filament has a uniform reactivity b_i. With the local geometry defined as similar to (1.1), we obtain N canonical inner problems for each filament, with each given by the solution to (see (2.3))

$$\begin{aligned} &\Delta_{\mathbf{y}} v_{ci} = 0\,, \quad \mathbf{y} \in \mathbb{R}^2 \setminus \mathcal{B}_i\,, \\ &\partial_n v_{ci} + b_i v_{ci} = 0\,, \quad \mathbf{y} \in \partial\mathcal{B}_i\,; \qquad v_{ci} \sim \log|\mathbf{y}| - \log\left[d_{ci}(b_i)\right] + o(1)\,, \quad \text{as} \quad |\mathbf{y}| \to \infty\,. \end{aligned} \tag{2.26}$$

For Γ_i, the far-field of v_{ci} provides a matching condition written in terms of outer variables and a line density $A_i(s_i)$ as (see (2.5))

$$v_i \sim A_i(s_i)\left(\log\left(\eta/\varepsilon\right) - \log\left[d_{ci}(b_i)\right]\right) \sim A_i(s_i)\log\eta + A_i(s_i)/\nu_i\,, \qquad \forall s_i \in [0,L_i]\,, \tag{2.27}$$

where $\nu_i \equiv -1/\log[\varepsilon d_{ci}(b_i)]$ and $\eta = |\mathbf{x} - \mathbf{X}_i(s_i)|$ is the perpendicular distance from any given target point $\mathbf{X}_i(s_i)$ on the i-th filament. Upon matching the inner solution near each filament to the outer solution, we obtain in place of (2.9) that the outer solution satisfies

$$\Delta_{\mathbf{x}} u = -\frac{1}{D} + 2\pi\sum_{i=1}^N \int_{\Gamma_i} A_i(s_i')\delta(\mathbf{x} - \mathbf{X}_i(s_i'))\,\mathrm{d}s_i'\,, \quad \mathbf{x} \in \Omega \setminus \cup_{i=1}^N \Gamma_i\,; \quad \partial_n u = 0\,, \quad \mathbf{x} \in \partial\Omega\,, \tag{2.28a}$$

$$u - A_i(s_i)\log|\mathbf{x} - \mathbf{X}_i(s_i)| \to \frac{A_i(s_i)}{\nu_i} \quad \text{as} \quad \mathbf{x} \to \mathbf{X}_i(s_i)\,, \quad s_i \in [0,L_i]\,, \quad i \in \{1,\dots,N\}\,. \tag{2.28b}$$

Our goal is to derive a coupled set of integral equations for the line densities $A_i(s_i)$ from enforcing the N constraints obtained from the regular parts of the singularity structures in (2.28b). Upon applying the divergence theorem to (2.28a) we readily derive that

$$\sum_{i=1}^{N} \int_{\Gamma_i} A_i(s_i)\, \mathrm{d}s_i = \frac{|\Omega|}{2\pi D}\,. \tag{2.29}$$

In place of (2.11) the outer solution is now represented in terms of the Neumann Green's function G and an unknown constant χ by

$$u(\mathbf{x}) = \chi - 2\pi \sum_{i=1}^{N} \int_{\Gamma_i} A_i(s_i') G(\mathbf{x}; \mathbf{X}_i(s_i'))\, \mathrm{d}s_i'\,, \quad \text{for} \quad \mathbf{x} \notin \cup_{i=1}^{N} \Gamma_i\,, \tag{2.30}$$

where the global MFRT is related to χ by

$$\bar{u} = \chi + o(1)\,. \tag{2.31}$$

For each fixed $j \in \{1, \ldots, N\}$, we decompose G into its singular part and regular part as

$$G\big(\mathbf{x}; \mathbf{X}_j(s_j')\big) = \frac{1}{4\pi |\mathbf{x} - \mathbf{X}_j(s_j')|} + R\big(\mathbf{x}; \mathbf{X}_j(s_j')\big)\,, \tag{2.32}$$

in order to reduce (2.30) to

$$\begin{aligned} u(\mathbf{x}) = \chi &- \frac{1}{2} \int_{\Gamma_j} \frac{A_j(s_j')}{|\mathbf{x} - \mathbf{X}_j(s_j')|}\, \mathrm{d}s_j' - 2\pi \int_{\Gamma_j} A_j(s_j') R(\mathbf{x}; \mathbf{X}_j(s_j'))\, \mathrm{d}s_j' \\ &- 2\pi \sum_{\substack{i=1 \\ i \neq j}}^{N} \int_{\Gamma_i} A_i(s_i') G\big(\mathbf{x}; \mathbf{X}_i(s_i')\big)\, \mathrm{d}s_i'\,, \quad \text{for} \quad \mathbf{x} \notin \cup_{i=1}^{N} \Gamma_i\,. \end{aligned} \tag{2.33}$$

We now fix a target point $\mathbf{X}_j(s_j)$ on Γ_j and we let $\mathbf{x} = \mathbf{X}_{\eta,j}(s_j)$ denote any point at a distance η from $\mathbf{X}_j(s_j)$ in the normal plane to Γ_j at $\mathbf{X}_j(s_j)$. As similar to the analysis in (2.14)-(2.16) for a single filament, we obtain in the limit $\eta \to 0$ that in place of (2.16) we now have

$$\begin{aligned} u \sim A_j(s_j) \log \eta + \chi - \frac{1}{2} A_j(s_j) \mathcal{E}_j(s_j) &+ \frac{1}{2} \int_{\Gamma_j} \frac{A_j(s_j) - A_j(s_j')}{|\mathbf{X}_j(s_j) - \mathbf{X}_j(s_j')|}\, \mathrm{d}s_j' - 2\pi \int_{\Gamma_j} A_j(s_j') R(\mathbf{X}_j(s_j); \mathbf{X}_j(s_j'))\, \mathrm{d}s_j' \\ &- 2\pi \sum_{\substack{i=1 \\ i \neq j}}^{N} \int_{\Gamma_i} A_i(s_i') G\big(\mathbf{X}_j(s_j); \mathbf{X}_i(s_i')\big)\, \mathrm{d}s_i'\,, \quad \text{as} \quad \mathbf{X}_{\eta,j}(s_j) \to \mathbf{X}_j(s_j)\,. \end{aligned} \tag{2.34}$$

Here $\mathcal{E}_j(s_j)$, is *intrinsic self-energy of* Γ_j defined by

$$\mathcal{E}_j(s_j) \equiv \lim_{\eta \to 0^+} \left(\int_{\Gamma_j} \frac{\mathrm{d}s_j'}{|\mathbf{X}_{\eta,j}(s_j) - \mathbf{X}_j(s_j')|} + 2 \log \eta \right)\,. \tag{2.35}$$

Finally, to obtain our coupled set of integral equations for the line densities $A_j(s_j)$ for $j \in \{1, \ldots, N\}$ and χ, we enforce from (2.28b) that the limiting behavior in (2.34) must satisfy $u \sim A_j(s_j) \log \eta + A(s_j)/\nu_j$ as $|\mathbf{X}_{\eta,j}(s_j) - \mathbf{X}_j(s_j)| = \eta \to 0$. We summarize our result in the following proposition:

Proposition 3. *Let $\cup_{j=1}^{N} \Gamma_j$ be a collection of smooth, simple, non-intersecting closed curves in Ω parameterized by arclength as $\mathbf{X}_j(s_j)$ for $j \in \{1, \ldots, N\}$ with dist$(\Gamma_i, \Gamma_j) = \mathcal{O}(1)$ for $i \neq j$. Assume that each*

filament centered around Γ_j has an $\mathcal{O}(\varepsilon)$ cross-sectional diameter and a uniform shape $\varepsilon\mathcal{B}_j$. In the limit $\varepsilon \to 0$, the asymptotic solution to (1.2) *in the outer region at $\mathcal{O}(1)$ distances from $\cup_{j=1}^N \Gamma_j$ is*

$$u(\mathbf{x}) = \chi - 2\pi \sum_{j=1}^{N} \int_{\Gamma_j} A_j(s_j) G(\mathbf{x}; \mathbf{X}_j(s_j))\, \mathrm{d}s_j\,, \quad \textit{for} \quad \mathbf{x} \notin \cup_{j=1}^N \Gamma_j\,, \tag{2.36}$$

where the line densities $A_j(s_j)$ for $j \in \{1,\dots,N\}$ and the asymptotic approximation χ to the GMFRT $\bar{u}$ are solutions to the coupled 1-D Fredholm integral equations of the second kind, defined for all $s_j \in [0, L_j]$ by

$$\mathcal{K}_j A_j + \sum_{\substack{i=1 \\ i\neq j}}^{N} \mathcal{G}_{ji} A_i = \chi, \quad j = 1,\dots,N; \qquad \sum_{j=1}^{N} \int_{\Gamma_j} A_j(s_j)\, \mathrm{d}s_j = \frac{|\Omega|}{2\pi D}, \tag{2.37}$$

where the integral operators $\mathcal{K}_j$ and $\mathcal{G}_{ji}$ are defined in (1.7). *In* (2.36) *G is the Neumann Green's function with regular part R satisfying* (1.4).

2.5 Splitting probabilities

In this subsection we describe an extension of our analysis to determine the splitting probabilities for the case of N filaments $\Gamma_{\varepsilon,j}$ for $j \in \{1,\dots,N\}$. We again assume that the centerlines Γ_j for $j \in \{1,\dots,N\}$ are a collection of non-intersecting, smooth and simple closed curves. Let $\phi_k(\mathbf{x})$ be the probability that a searcher starting at $\mathbf{x}$ is absorbed by filament k before any other. Then, $\phi_k(\mathbf{x})$ satisfies

$$\Delta_{\mathbf{x}} \phi_k = 0\,, \quad \mathbf{x} \in \Omega \setminus \cup_{j=1}^N \Gamma_{\varepsilon,j}\,; \qquad \partial_n \phi_k = 0\,, \quad \mathbf{x} \in \partial\Omega\,, \tag{2.38a}$$

$$\varepsilon \partial_n \phi_k + b_j\,(\phi_k - \delta_{jk}) = 0\,, \qquad \mathbf{x} \in \partial\Gamma_{\varepsilon,j}\,, \quad j \in \{1,\dots,N\}\,, \tag{2.38b}$$

with $\phi_k = \delta_{jk}$ on $\partial\Gamma_{\varepsilon,j}$ when $b_j = \infty$ and where δ_{jk} is the Kronecker symbol. The analysis outlined in the previous section can be applied in an identical fashion to solve (2.38). The solvability condition is altered by the homogeneous nature of the right-hand side of (2.38a) and an extra constant term is introduced by the boundary condition (2.38b). The result is summarized as follows:

Proposition 4. *Let $\cup_{j=1}^N \Gamma_j$ be a collection of smooth, simple, non-intersecting closed curves in Ω parameterized by arclength as $\mathbf{X}_j(s_j)$ for $j \in \{1,\dots,N\}$ with dist$(\Gamma_i, \Gamma_j) = \mathcal{O}(1)$ for $i \neq j$. Assume that each filament centered around Γ_j has an $\mathcal{O}(\varepsilon)$ cross-sectional diameter and a uniform shape $\varepsilon\mathcal{B}_j$. In the limit $\varepsilon \to 0$, the asymptotic solution to* (2.38) *in the outer region at $\mathcal{O}(1)$ distances from $\cup_{j=1}^N \Gamma_j$ takes the form*

$$\phi_k(\mathbf{x}) \sim \bar{\phi}_k - 2\pi \sum_{j=1}^{N} \int_{\Gamma_j} B_{kj}(s_j)\, G\big(\mathbf{x}; \mathbf{X}_j(s_j)\big)\, \mathrm{d}s_j\,, \quad \mathbf{x} \in \Omega \setminus \cup_{j=1}^N \Gamma_j\,, \tag{2.39}$$

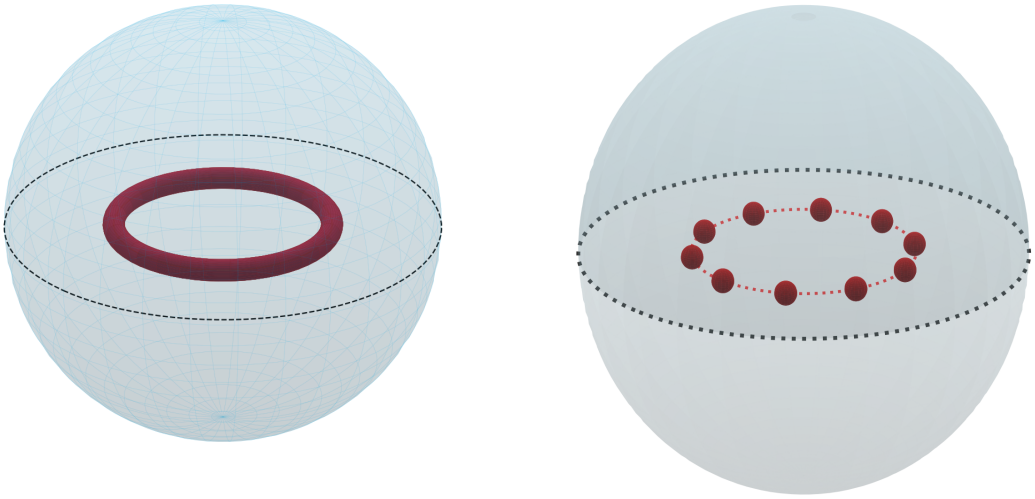
where $B_{kj}(s_j)$ for $j \in 1,\dots,N$ are the line densities of on Γ_j for the k-th splitting probability. The quantity $\bar{\phi}_k$ is the leading-order volume average of ϕ_k over all starting locations. The line densities satisfy a system of coupled 1-D Fredholm integral equations with a constraint, defined for all $s_j \in [0, L_j]$ by

$$\mathcal{K}_j B_{kj} + \sum_{\substack{i=1 \\ i\neq j}}^{N} \mathcal{G}_{ji} B_{ki} = \bar{\phi}_k - \delta_{jk}, \quad j = 1,\dots,N; \qquad \sum_{j=1}^{N} \int_{\Gamma_j} B_{kj}(s_j)\, \mathrm{d}s_j = 0, \tag{2.40}$$

where the integral operators $\mathcal{K}_j$ and $\mathcal{G}_{ji}$ are defined in (1.7).

3 Closed-form solution: A concentric circular filament in a sphere

To illustrate our analysis, we first consider a simple example where Ω is the unit sphere, with $|\Omega| = 4\pi/3$, and where Γ is a simple closed circular ring of radius $r_0 < 1$ in the equatorial plane centered at the origin, so that $L = |\Gamma| = 2\pi r_0$ (see Fig. 2(a) for a schematic). In this case, it is shown in Appendix B.1 that its intrinsic self-energy has the constant value $\mathcal{E} = 2\log(8r_0)$.



(a) Unit sphere with filament *(b) Unit sphere with balls*

Figure 2: Left: The unit sphere with a thin filament (torus) of circular cross-section with radius $\varepsilon = 0.05$ centered concentrically on the equatorial plane. The distance from the centerline of the filament to the origin is $r_0 = 0.5$. Right: $N = 10$ small spheres of a common radius $\sigma = 0.05$ equidistantly spaced on a concentric ring of radius $r_0 = 0.5$ within the unit sphere.

For the unit sphere, the regular part $R(\mathbf{x};\xi)$ of the Neumann Green's function $G(\mathbf{x};\boldsymbol{\xi})$ satisfying (1.4), as derived in Appendix A of [13], is

$$R(\mathbf{x};\boldsymbol{\xi}) = \frac{1}{4\pi|\mathbf{x}/|\mathbf{x}| - |\mathbf{x}|\boldsymbol{\xi}|} + \frac{1}{4\pi}\log\left(\frac{2}{1 - \mathbf{x}\cdot\boldsymbol{\xi} + |\mathbf{x}/|\mathbf{x}| - |\mathbf{x}|\boldsymbol{\xi}|}\right) + \frac{1}{8\pi}\left(|\mathbf{x}|^2 + |\boldsymbol{\xi}|^2\right) - \frac{7}{10\pi}\,. \tag{3.1}$$

Since the ring lies concentrically on the equatorial plane, it follows by symmetry that the line density $A(s)$ is independent of position along the ring. As a result, since $A(s) = A$ for all $s \in [0, L]$, we obtain from the constraint (2.10) that

$$A = \frac{|\Omega|}{2\pi D|\Gamma|} = \frac{1}{3\pi D r_0}\,. \tag{3.2}$$

As a result, we obtain from (2.19) upon using $\mathcal{E} = 2\log(8r_0)$ that

$$\bar{u} \sim \chi = \frac{1}{3\pi D}\left[\frac{1}{r_0}\left(-\log(\varepsilon d_c)\right) + \frac{\log(8r_0)}{r_0} + \mathcal{J}\right], \quad \text{where} \quad \mathcal{J} \equiv \frac{2\pi}{r_0}\int_\Gamma R\left(\mathbf{X}(s);\mathbf{X}(s')\right)\,\mathrm{d}s'\,, \tag{3.3}$$

where $\mathbf{X}(s) = r_0\left(\cos(s/r_0), \sin(s/r_0), 0\right)^T$ is the parameterization of the circular ring in terms of arclength s. By symmetry it follows that the integral $\mathcal{J}$ is independent of s.

To evaluate $\mathcal{J}$ it is convenient to introduce ϕ and ϕ' by $s = r_0\phi$ and $s' = r_0\phi'$, so that

$$\mathcal{J} = 2\pi \int_0^{2\pi} R\left(\mathbf{X}(r_0\phi); \mathbf{X}(r_0\phi')\right)\, \mathrm{d}\phi' \,. \tag{3.4}$$

To evaluate $R\left(\mathbf{X}(r_0\phi); \mathbf{X}(r_0\phi')\right)$ from (3.1) we first calculate that

$$\mathbf{X}(r_0\phi)\cdot\mathbf{X}(r_0\phi') = r_0^2\cos\left(\phi-\phi'\right)\,, \qquad \left|\frac{\mathbf{X}(r_0\phi)}{|\mathbf{X}(r_0\phi)|} - \mathbf{X}(r_0\phi')\,|\mathbf{X}(r_0\phi)|\right| = \left(r_0^4 + 1 - 2r_0^2\cos\left(\phi-\phi'\right)\right)^{1/2}\,,$$

so that from (3.1) we get

$$\begin{aligned} 2\pi R\left(\mathbf{X}(r_0\phi); \mathbf{X}(r_0\phi')\right) = {} & \frac{1}{2\left(r_0^4+1-2r_0^2\cos\left(\phi-\phi'\right)\right)^{1/2}} + \frac{1}{2}\left(r_0^2 - \frac{14}{5} + \log 2\right) \\ & - \frac{1}{2}\log\left[1 - r_0^2\cos\left(\phi-\phi'\right) + \left(r_0^4+1-2r_0^2\cos\left(\phi-\phi'\right)\right)^{1/2}\right]\,. \end{aligned} \tag{3.5}$$

Upon substituting (3.5) into (3.4) we get

$$\mathcal{J} = \frac{1}{2}I(r_0) + \pi\left(r_0^2 - \frac{14}{5} + \log 2\right) - \frac{1}{2}J(r_0)\,, \tag{3.6}$$

where we have defined

$$I(r_0) \equiv \int_0^{2\pi} \frac{\mathrm{d}\psi}{\left(r_0^4+1-2r_0^2\cos\psi\right)^{1/2}}\,, \quad J(r_0) \equiv \int_0^{2\pi} \log\left[1 - r_0^2\cos\psi + \left(r_0^4+1-2r_0^2\cos\psi\right)^{1/2}\right]\,\mathrm{d}\psi\,. \tag{3.7}$$

Next, we evaluate $I(r_0)$ in terms of the complete elliptic integral of the first kind of modulus m: $K(m) \equiv \int_0^{\pi/2} d\phi/\sqrt{1-m^2\sin^2\phi}$. To do so, we let $\cos\psi = 2\cos^2(\psi/2) - 1$ and then set $\phi = \psi/2$. We obtain that

$$I(r_0) = 4\int_0^{\pi/2} \frac{\mathrm{d}\phi}{\left[(r_0^2+1)^2 - 4r_0^2\cos^2\phi\right]^{1/2}} = \frac{4}{1+r_0^2}K\left(\frac{2r_0}{1+r_0^2}\right) = 4K\left(r_0^2\right)\,, \tag{3.8}$$

where we used the Landen transformation to obtain the last equality in (3.8).

Upon using (3.8) in (3.6) and recalling (3.3), we conclude that

$$\bar{u} \sim \chi = \frac{1}{3\pi D}\mathcal{F}_\varepsilon(r_0)\,, \tag{3.9a}$$

where $\mathcal{F}_\varepsilon(r_0)$ is defined by

$$\mathcal{F}_\varepsilon(r_0) \equiv \frac{\log(a_\varepsilon r_0)}{r_0} + 2K\left(r_0^2\right) + \pi\left(r_0^2 + \log 2 - \frac{14}{5}\right) - \frac{1}{2}J(r_0)\,, \quad \text{with} \quad a_\varepsilon \equiv \frac{8}{\varepsilon d_c}\,. \tag{3.9b}$$

Here $J(r_0)$ as defined in (3.7). From an evaluation of $J(r_0)$ by the trapezoidal rule, in Fig. 3A we plot $\mathcal{F}_\varepsilon(r_0)$ on $\mathcal{O}(\varepsilon) \ll r_0 \ll 1-\mathcal{O}(\varepsilon)$ for several values of εd_c. This numerical evidence suggests that there is an optimum ring radius $r_0 = r_{0\,\min}$ at which $\mathcal{F}_\varepsilon(r_0)$ is minimized. From (3.9a), this optimum value determines the optimal location of a concentric equatorial ring that minimizes the global MFRT $\bar{u}$ in the unit sphere to all logarithmic orders.

In Appendix C we prove that $\mathcal{F}_\varepsilon(r_0)$ has a unique minimum $r_{0\,\min}$ on $\mathcal{O}(\varepsilon) \ll r_0 \ll 1-\mathcal{O}(\varepsilon)$ and determine an approximation to $r_{0\,\min}$ for $\varepsilon d_c \ll 1$. The result derived in Appendix C is summarized as follows:

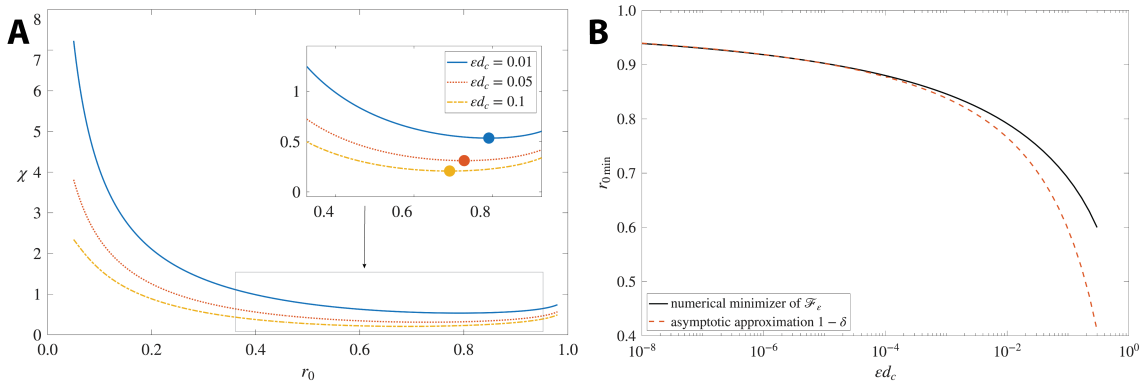


Figure 3: The exactly solvable one-ring case. Panel A: The MFRT $\bar{u} \sim \chi$, defined in (3.9)*, versus the ring radius r_0 for three values of εd_c when $D = 1$. The minimizing radii $r_{0\,\min}$ is highlighted for each case by a solid dot . Panel B: The minimizing ring radius $r_{0\,\min}$ against εd_c from the numerical minimization of $\mathcal{F}_\varepsilon$ (solid line) and the asymptotic approximation $r_{0\,\min} \sim 1 - \delta$ (dashed line) given in Proposition 5.*

Proposition 5. *In the limit $\varepsilon \to 0$, there is a unique centerline radius $r_0 = r_{0\,\min}$ of a concentric equatorial filament that minimizes the global MFRT inside the unit sphere. The optimal MFRT is*

$$\bar{u}_{\min} \sim \chi_{\min} = \frac{1}{3\pi D}\mathcal{F}_\varepsilon(r_{0\,\min}) \quad \text{with} \quad \mathcal{F}_\varepsilon(r_0) \equiv \frac{\log(a_\varepsilon r_0)}{r_0} + 2K\left(r_0^2\right) + \pi\left(r_0^2 + \log 2 - \frac{14}{5}\right) - \frac{1}{2}J(r_0)\,, \quad (3.10)$$

where r_{0min} is the unique root on $\mathcal{O}\left(1/a_\varepsilon\right) \ll r_0 \ll 1 - \mathcal{O}\left(1/a_\varepsilon\right)$ of $\mathcal{C}_\varepsilon(r_0) = 0$ given in (C.6)*. Here $J(r_0)$ is defined in* (3.7) *and $a_\varepsilon = 8/(\varepsilon d_c)$. For $a_\varepsilon \gg 1$, we have the explicit approximation*

$$r_{0\,\min} \sim 1 - \frac{1}{\log a_\varepsilon} - \frac{[\log(4\log a_\varepsilon) + 1/2]}{(\log a_\varepsilon)^2}\,. \quad (3.11)$$

Although the optimal ring radius tends to the boundary of the unit sphere as ε decreases, the requirement that $r_{0\,\min} \ll 1 - \mathcal{O}\left(1/a_\varepsilon\right)$ is never violated. In addition, (3.11) shows that the optimal ring radius depends on the local geometry and reactivity of the filament cross-section through its logarithmic reactive capacitance $d_c = d_c(b)$. Finally, we remark that as r_0 increases the surface area of the filament $4\pi^2\varepsilon r_0$ increases, but is still $\mathcal{O}(\varepsilon)$ for any $r_0 = \mathcal{O}(1)$.

In Table 1 we show that the approximate root (3.11) provides an increasingly adequate approximation to the numerically computed root of $\mathcal{C}_\varepsilon(r_0) = 0$ as εd_c decreases. The prediction for the minimum of the MFRT as obtained from (3.11) and the numerically computed root are also favorably compared in Table 1. See also the agreement shown in Fig. 3B.

εd_c	$r_{0\,\min}$ (num)	$r_{0\,\min}$ (asy)	% error for $r_{0\,\min}$	$\chi_{\min}$ (num)	$\chi_{\min}$ (asy)
0.05	0.7290	0.6667	8.55%	0.3109	0.3187
0.02	0.7680	0.7307	4.86%	0.4406	0.4439
0.01	0.7914	0.7657	3.25%	0.5349	0.5367
0.005	0.8110	0.7931	2.21%	0.6267	0.6277
0.0025	0.8276	0.8151	1.52%	0.7164	0.7170

Table 1: Comparison of the asymptotic result (3.11) *for the optimal ring radius with the numerically computed root of $\mathcal{C}_\varepsilon(r_0) = 0$, given in* (C.6)*, for several values of εd_c. The last two columns show a favorable comparison for the optimal MFRT given in* (3.10) *with either the approximate root or the numerically computed root.*

3.1 Optimization of a ring pattern of small spheres

We now compare results from our previous analysis for the MFRT for a thin equatorial filament in the unit sphere to a related problem where there are N small identical perfectly absorbing targets equidistantly spaced on a concentric ring of radius r_0 within the unit sphere. A schematic of the geometry is shown in Fig. 2(b) when the targets are small spheres. In a 3-D domain punctured by N such small targets, the MFRT $u(\mathbf{x})$ satisfies

$$\Delta u = -\frac{1}{D}\,, \quad \mathbf{x} \in \Omega \setminus \Omega_a\,, \tag{3.12a}$$

$$\partial_n u = 0\,, \quad \mathbf{x} \in \partial\Omega\,; \qquad u = 0\,, \quad \mathbf{x} \in \partial\Omega_a \equiv \cup_{j=1}^N \partial\Omega_{\sigma,j}\,, \tag{3.12b}$$

where $\Omega_{\sigma,j}$ is a small 3-D target of diameter $\mathcal{O}(\sigma)$ centered at $\mathbf{x}_j \in \Omega$, and $\Omega_a = \cup_{j=1}^N \Omega_{\sigma,j}$. We assume that the targets are well-separated in the sense that $\text{dist}(\mathbf{x}_j, \mathbf{x}_k) \gg \mathcal{O}(\sigma)\ \ \forall j \neq k$ and $\text{dist}(\mathbf{x}_j, \partial\Omega) \gg \mathcal{O}(\sigma)$. The volume averaged MFRT, denoted by $\bar{u}$, is defined by

$$\bar{u} \equiv \frac{1}{|\Omega \setminus \Omega_a|} \int_{\Omega\setminus\Omega_a} u(\mathbf{x})\, \mathrm{d}\mathbf{x}\,. \tag{3.13}$$

For the small target limit $\sigma \to 0$, by using the method of matched asymptotic expansions it was derived in Principal Result 3.1 of [13] that

$$\bar{u} \sim \chi_{\text{ball}} = \frac{|\Omega|}{4\pi D}\left[\frac{1}{\sigma N C} + p(\mathbf{x}_1,\ldots,\mathbf{x}_N) + o(1)\right]\,; \quad p(\mathbf{x}_1,\ldots,\mathbf{x}_N) \equiv \frac{4\pi}{N^2}\sum_{j=1}^N \left(R(\mathbf{x}_j;\mathbf{x}_j) + \sum_{\substack{i=1\\ i\neq j}}^N G(\mathbf{x}_i;\mathbf{x}_j)\right)\,, \tag{3.14}$$

where $G(\mathbf{x};\boldsymbol{\xi})$ is the Neumann Green's function with regular part $R(\boldsymbol{\xi};\boldsymbol{\xi})$ (see (1.4)). Here C is the capacitance of the rescaled target $\Omega_0 = \Omega_{\sigma,j}/\sigma$, defined in terms of the far-field behavior of the canonical local problem

$$\Delta_{\mathbf{y}} w_c = 0\,, \quad \mathbf{y} \in \mathbb{R}^3 \setminus \Omega_0\,; \qquad w_c = 1\,, \quad \mathbf{y} \in \partial\Omega_0\,; \qquad w_c = \frac{C}{|\mathbf{y}|} + \mathcal{O}(|\mathbf{y}|^{-2}) \quad \text{as} \quad |\mathbf{y}| \to \infty\,, \tag{3.15}$$

When Ω_0 is the unit ball we have $C = 1$, while $C = 2/\pi$ when Ω_0 is a flat disk of unit radius.

Now suppose that the N identical traps are equidistantly spaced on a concentric ring of radius r_0 within the unit sphere and are centered at $\mathbf{x}_j = r_0\,(\cos\theta_j, \sin\theta_j, 0)^T$ with $\theta_j = 2\pi(j-1)/N$ for $j \in \{1,\ldots,N\}$. Since this pattern has a cyclic symmetry in the sphere, (3.14) reduces to

$$p(\mathbf{x}_1,\ldots,\mathbf{x}_N) = \frac{4\pi}{N}\left(R(\mathbf{x}_1;\mathbf{x}_1) + \sum_{j=2}^N G(\mathbf{x}_1;\mathbf{x}_j)\right)\,. \tag{3.16}$$

From (3.1) we calculate that

$$4\pi R(\mathbf{x}_1,\mathbf{x}_1) = \frac{1}{(1-r_0^2)} - \log(1-r_0^2) + r_0^2 - \frac{14}{5}\,, \tag{3.17}$$

while for $j \in \{2,\ldots,N\}$, we have

$$4\pi G(\mathbf{x}_1;\mathbf{x}_j) = \frac{1}{|\mathbf{x}_1-\mathbf{x}_j|} + \frac{1}{r_{c,j}} + \log\left(\frac{2}{1-\mathbf{x}_1\cdot\mathbf{x}_j + r_{c,j}}\right) + \frac{1}{2}\left(|\mathbf{x}_1|^2 + |\mathbf{x}_j|^2\right) - \frac{14}{5} \quad \text{where} \quad r_{c,j} \equiv \Big|\frac{\mathbf{x}_1}{|\mathbf{x}_1|} - \mathbf{x}_j|\mathbf{x}_1|\Big|\,. \tag{3.18}$$

Since $\theta_1 = 0$, we calculate that

$$\mathbf{x}_1 \cdot \mathbf{x}_j = r_0^2 \cos(\theta_j)\,, \qquad |\mathbf{x}_1 - \mathbf{x}_j| = 2r_0 \sin\left(\frac{\theta_j}{2}\right)\,, \qquad r_{c,j} = \sqrt{r_0^4 - 2r_0^2\cos\theta_j + 1}\,. \tag{3.19}$$

In order that the small traps are well-separated on the ring, we require that $2\sigma N \ll 2\pi r_0$, so that $\sigma N \ll \pi r_0$.

Upon substituting (3.19) into (3.18), and absorbing the regular part (3.17) into the $j = 1$ term, (3.16) becomes solely a function of N and the ring radius r_0. We summarize our result as follows:

Proposition 6. *For N identical small targets equidistantly spaced on a concentric ring of radius r_0 inside the unit sphere, the volume-averaged MFRT is given for $\sigma \to 0$ by*

$$\bar{u} \sim \chi_{ball} = \frac{|\Omega|}{4\pi D}\left[\frac{1}{\sigma N C} + P_N(r_0) + o(1)\right]\,, \tag{3.20a}$$

where $|\Omega| = 4\pi/3$ and

$$P_N(r_0) \equiv r_0^2 - \frac{14}{5} + \log 2 + \frac{\mathcal{S}_N}{2r_0 N} + \frac{1}{N}\left(\sum_{j=1}^{N}\frac{1}{r_{c,j}} - \log\left(1 - r_0^2\cos\theta_j + r_{c,j}\right)\right)\,. \tag{3.20b}$$

Here $r_{c,j}$ is given in (3.19), $\theta_j = 2\pi(j-1)/N$ for $j \in \{1,\ldots,N\}$, and $\mathcal{S}_N$ is the discrete sum

$$\mathcal{S}_N \equiv \sum_{j=1}^{N-1}\frac{1}{\sin\left(\pi j/N\right)}\,. \tag{3.20c}$$

Since there are no analytical formulas for the discrete sums in (3.20b), the optimal ring radius r_{opt} for a given N is obtained by a numerical line search to determine the minimum of $P_N(r_0)$ on $0 < r_0 < 1$, with the results shown in Table 3. The numerical results in the second column of Table 3 suggest that r_{opt} tends very slowly to the boundary as N increases. In order to estimate the optimal ring radius for $N \gg 1$, we need the following lemma, as proved in Appendix D, for the behavior of S_N for large N.

Lemma 1. *For $N \gg 1$, we have*

$$\mathcal{S}_N = \mathcal{S}_{NA} - \frac{\pi}{36N} + \mathcal{O}(N^{-3})\,, \qquad \textit{where} \quad \mathcal{S}_{NA} \equiv \frac{2N}{\pi}\left[\log\left(\frac{2N}{\pi}\right) + \gamma_e\right]\,. \tag{3.21}$$

Here $\gamma_e \approx 0.5772$ is Euler's constant.

In Table 2 we show that the simple approximation $\mathcal{S}_{NA}$ in (3.21) compares very favorably with the discrete sum $\mathcal{S}_N$ even for $N = 4$.

To analyze the large N limit of (3.20), but under the well-separated assumption that $\sigma N \ll \pi r_0$, we simply approximate the discrete sums in (3.20b) by their corresponding Riemann sums and we use $\mathcal{S}_{NA}$ for $\mathcal{S}_N$. The Riemann sums are identified by recalling the two integrals $I(r_0)$ and $J_0(r_0)$ in (3.7) and (3.8). In this way, for large N we conclude that

$$\bar{u} \sim \chi_{\rm ball} = \frac{1}{3\pi D}\left(\frac{\pi}{\sigma N C} + \mathcal{F}_N(r_0)\right)\,, \tag{3.22a}$$

where $\mathcal{F}_N(r_0)$ is defined by

$$\mathcal{F}_N(r_0) \equiv \frac{\log(a_N)}{r_0} + 2K\left(r_0^2\right) + \pi\left(r_0^2 + \log 2 - \frac{14}{5}\right) - \frac{1}{2}J(r_0)\,, \qquad a_N \equiv \frac{2Ne^{\gamma_e}}{\pi}\,. \tag{3.22b}$$

N	$\mathcal{S}_N$	$\mathcal{S}_{NA}$	Percent error (%)
4	3.828	3.850	0.566%
6	7.309	7.324	0.198%
8	11.219	11.230	0.097%
10	15.450	15.459	0.056%
20	39.738	39.742	0.011%
40	97.134	97.136	0.002%

Table 2: Comparison between exact sum $\mathcal{S}_N$ and its large-N asymptotics $\mathcal{S}_{NA}$ in (3.21)*. We observe that even for $N = 4$, the error in the approximation is less than* 1%*.*

N	r_{opt} (3.20b)	r_{opt} (3.22b)
2	0.4289	0.4798
4	0.5613	0.5740
6	0.6095	0.6133
8	0.6357	0.6369
10	0.6529	0.6537
20	0.6967	0.6969
40	0.7315	0.7320
60	0.7488	0.7492
80	0.7600	0.7603
100	0.7681	0.7685

Table 3: Optimal ring radius for N small targets equidistantly-spaced on a concentric ring obtained from minimizing either the discrete sum $P_N(r_0)$ in (3.20b) *or its large-N approximation $\mathcal{F}_N(r_0)$ in* (3.22b)*. Remarkably, we observe that the large-N approximation* (3.22b) *agrees with the discrete optimum in* (3.20b) *to within 5×10^{-4} for $N \geq 10$ (and to within* 0.013 *already when $N = 4$).*

We remark that $\mathcal{F}_N(r_0)$ is identical to (3.10) for the filament problem if a_N is replaced by $a_\varepsilon r_0$. As such, we can repeat an almost identical analysis as done for an equatorial ring filament to establish that there is an optimal ring radius for $N \gg 1$ equidistantly spaced small targets that is close to the boundary of the sphere. In the third column of Table 3 we show that the minimizer of $\mathcal{F}_N(r_0)$ provides a close approximation to that obtained for the discrete sum $P_N(r_0)$ even when N is only moderately large.

For $N \gg 1$, we can derive an analytical scaling law for the optimal radius by repeating a similar analysis as for the thin filament. We find for large N that

$$r_{opt} = 1 - \frac{1}{\log a_N} - \frac{[\log(\log a_N) + \log 4 - 1/2]}{(\log a_N)^2}\,. \tag{3.23}$$

In particular if we set $N = \mathcal{O}(\sigma^{-1})$, we observe that the optimal ring radius is $\mathcal{O}(-1/\log\sigma)$ close to the boundary; a result that is qualitatively the same as that derived in (3.11) for the thin filament. However, since $\log(a_N)$ is not very large unless N is very large, (3.23) does not compare very favorably at moderate values of N with the results shown in Table 3.

Finally, we compare our MFRT result for $N \gg 1$ small perfectly absorbing targets, each of diameter $\mathcal{O}(\sigma)$, that are uniformly spaced on a ring with that obtained earlier for an equatorial filament of circular cross-section of radius ε with a perfectly absorbing boundary. For this filament, we set $d_c = 1$, $L = 2\pi r_0$,

and $(3\pi D r_0)^{-1} = |\Omega|/(2\pi DL)$ in (3.9) to obtain

$$\chi_{\rm filam} = \frac{|\Omega|}{2\pi DL}\left(\underbrace{-\log\varepsilon + \log\left(\frac{4L}{\pi}\right)}+u_b\right), \quad u_b \equiv 2r_0K(r_0^2) + \pi r_0(r_0^2+\log 2 - 14/5) - \frac{r_0}{2}J(r_0)\,. \quad (3.24)$$

The corresponding result for $N \gg 1$ small targets on the ring, as obtained from (3.22), can be written as

$$\chi_{\rm ball} = \frac{|\Omega|}{2\pi DL}\left(\underbrace{\frac{L}{2\sigma NC} + \log\left(\frac{2N}{\pi}\right) + \gamma_e}+u_b\right). \quad (3.25)$$

Upon equating the underlined terms in (3.24) and (3.25) we observe that $N \gg 1$ identical small targets of diameter $\mathcal{O}(\sigma)$ will yield asymptotically the same GMFRT as that for a filament of cross-sectional radius ε, when

$$\varepsilon = \frac{2L}{N}\exp\left(-\frac{L}{2\sigma NC} - \gamma_e\right). \quad (3.26)$$

In §6 we perform a more detailed and general analysis of the fragmentation of a filament of length L into N localized uniformly spaced small targets. We will show that the relation (3.26) can be derived from the analysis of a new inner problem in the *transition* scaling regime $\mathcal{O}(\sigma) \ll L/N \ll \mathcal{O}(1)$ that exists between well-separated and closely-spaced targets.

4 Trapezoidal Nyström discretization of the boundary integral equation

In this section we describe a boundary integral method for the solution of the system (2.37) based on the trapezoidal rule. The first step is to decompose the system into filament self-interacting terms and filament coupling terms. For a density $A(s)$ on a filament Γ_j, with the self-filament integral operator $\mathcal{K}_j$ by

$$(\mathcal{K}_jA)(s) \equiv \frac{A(s)}{\nu_j} + \frac{1}{2}A(s)\,\mathcal{E}_j(s) - \frac{1}{2}\int_{\Gamma_j}\frac{A(s)-A(s')}{|\mathbf{X}_j(s)-\mathbf{X}_j(s')|}\,{\rm d}s' + 2\pi\int_{\Gamma_j}A(s')\,R\big(\mathbf{X}_j(s);\mathbf{X}_j(s')\big)\,{\rm d}s', \quad (4.1)$$

for $s \in [0, L_j]$ and L_j is the length of the j^{th} filament. For a line density $A(s)$, the coupling terms between filaments Γ_i and Γ_j for $i \neq j$ is

$$\big(\mathcal{G}_{ji}A\big)(s) \equiv 2\pi\int_{\Gamma_i}A(s')\,G\big(\mathbf{X}_j(s);\mathbf{X}_i(s')\big)\,{\rm d}s'. \quad (4.2)$$

We now describe a trapezoidal rule for the discretization of the integral operators (4.1)-(4.2) and the numerical solution of (2.37). Our method is adapted to the case of simple closed curves. We subdivide the j^{th} filament Γ_j into M_j equally spaced nodes in terms of arc-length, by writing

$$h_j = \frac{L_j}{M_j}\,, \quad s_{j,p} = p\,h_j\,, \quad \mathbf{X}_{j,p} = \mathbf{X}_j(s_{j,p})\,, \qquad p = 1,\ldots,M_j\,. \quad (4.3)$$

In this setting, the trapezoid rule applied to a periodic function $f(s)$ on the filament Γ_j is

$$\int_{\Gamma_j}f(s)\,{\rm d}s = h_j\sum_{p=1}^{M_j}f(s_{j,p})\,. \quad (4.4)$$

The unknowns are $A_{j,p} = A_j(s_{j,p})$ and χ. Along each point on the curve, we employ the following notation

$$r_{pq}^{ji} = |\mathbf{X}_{j,p} - \mathbf{X}_{i,q}|\,, \qquad R_{pq}^{ji} = R(\mathbf{X}_{j,p}; \mathbf{X}_{i,q})\,, \qquad G_{pq}^{ji} = G(\mathbf{X}_{j,p}; \mathbf{X}_{i,q})\,. \tag{4.5}$$

We now focus on the discretization of the operator $\mathcal{K}_j$ for $j = 1, \ldots, N$ as defined in (4.1). We first recall the reduced form of the self-energy term $\mathcal{E}_j(s)$ as derived in (B.17) of Appendix B.2

$$\mathcal{E}_j(s) = 2\log\left(\frac{4L_j}{\pi}\right) + \int_{\Gamma_j}\left[\frac{1}{|\mathbf{X}_j(s) - \mathbf{X}_j(s')|} - \frac{\pi/L_j}{\left|\sin\left(\pi(s-s')/L_j\right)\right|}\right] \mathrm{d}s'\,. \tag{4.6}$$

Let $d_{pq}^j = (L_j/\pi)\,|\sin(\pi(s_{j,p} - s_{j,q})/L_j)|$ be the chord between nodes p and q on Γ_j. Then applying the trapezoidal rule to the first two terms of (4.1) yields

$$\begin{aligned}\frac{1}{2}A_{j,p}\mathcal{E}_{j,p} - \frac{h_j}{2}\sum_{\substack{q=1\\q\neq p}}^{M_j}\frac{A_{j,p} - A_{j,q}}{r_{pq}^{jj}} &= \frac{1}{2}A_{j,p}\left[2\log\frac{4L_j}{\pi} + h_j\sum_{\substack{q=1\\q\neq p}}^{M_j}\left(\frac{1}{r_{pq}^{jj}} - \frac{1}{d_{pq}^{j}}\right)\right] - \frac{h_j}{2}\sum_{\substack{q=1\\q\neq p}}^{M_j}\frac{A_{j,p} - A_{j,q}}{r_{pq}^{jj}} \\ &= \beta_j\, A_{j,p} + \frac{h_j}{2}\sum_{\substack{q=1\\q\neq p}}^{M_j}\frac{A_{j,q}}{r_{pq}^{jj}}\,,\end{aligned} \tag{4.7}$$

where after canceling the terms $A_{j,p}/r_{pq}^{jj}$, the remaining diagonal term is of form

$$\beta_j \equiv \log\left(\frac{4L_j}{\pi}\right) - \frac{h_j}{2}\sum_{\substack{q=1\\q\neq p}}^{M_j}\frac{1}{d_{pq}^{j}}\,, \tag{4.8}$$

and can be evaluated once per filament. The remaining smooth terms featuring the regular part R in $\mathcal{K}_j$ and the coupling terms $\mathcal{G}_{ji}$ are smooth and treated by a simple application of (4.4). The discretization of (2.37) for each $j = 1, \ldots, N$ and $p = 1, \ldots, M_j$ is then,

$$\Big(\frac{1}{\nu_j} + \beta_j\Big)A_{j,p} + \frac{h_j}{2}\sum_{\substack{q=1\\q\neq p}}^{M_j}\frac{A_{j,q}}{r_{pq}^{jj}} + 2\pi h_j\sum_{q=1}^{M_j}R_{pq}^{jj}A_{j,q} + 2\pi\sum_{\substack{i=1\\i\neq j}}^{N}h_i\sum_{q=1}^{M_i}G_{pq}^{ji}A_{i,q} = \chi\,, \tag{4.9}$$

together with the discrete form of the constraint,

$$\sum_{j=1}^{N}h_j\sum_{p=1}^{M_j}A_{j,p} = \frac{|\Omega|}{2\pi D}\,. \tag{4.10}$$

This system of linear equations can be compactly represented in block form as,

$$\begin{pmatrix}\mathsf{M}_{11} & \cdots & \mathsf{M}_{1N} & -\mathbf{e}\\ \vdots & \ddots & \vdots & \vdots\\ \mathsf{M}_{N1} & \cdots & \mathsf{M}_{NN} & -\mathbf{e}\\ h_1\mathbf{e}^T & \cdots & h_N\mathbf{e}^T & 0\end{pmatrix}\begin{pmatrix}\mathbf{A}_1\\ \vdots\\ \mathbf{A}_N\\ \chi\end{pmatrix} = \begin{pmatrix}\mathbf{0}\\ \vdots\\ \mathbf{0}\\ |\Omega|/(2\pi D)\end{pmatrix}\,, \tag{4.11}$$

where $\mathbf{A}_j = (A_{j,1}, \ldots, A_{j,M_j})^T$ and $\mathbf{e} = (1, \ldots, 1)^T$. Each block matrix M_{ji} (of size $M_j \times M_i$) is given elementwise as

$$\big(\mathsf{M}_{ji}\big)_{pq} = \begin{cases}\Big(\frac{1}{\nu_j} + \beta_j\Big)\delta_{pq} + h_j\left[\frac{1-\delta_{pq}}{2r_{pq}^{jj}} + 2\pi R_{pq}^{jj}\right], & i = j,\\ h_i\left[\frac{1}{2r_{pq}^{ji}} + 2\pi R_{pq}^{ji}\right], & i \neq j\end{cases} \qquad \begin{pmatrix}p = 1, \ldots, M_j\\ q = 1, \ldots, M_i\end{pmatrix}. \tag{4.12}$$

This system of dense equations is solved directly for the discretized line strengths $\{\mathbf{A}_j\}_{j=1}^N$ and constant χ. The outer solution (2.36) away from the filaments can then be evaluated with the same weights:

$$u(\mathbf{x}) \approx \chi - 2\pi \sum_{j=1}^{N} h_j \sum_{q=1}^{M_i} A_{j,q}\, G(\mathbf{x}; \mathbf{X}_{j,q}), \qquad \text{dist}(\mathbf{x}, \Gamma_j) \gg \mathcal{O}(\varepsilon) \quad j = 1, \ldots, N. \tag{4.13}$$

The equivalent discretization scheme for the splitting probabilities $\phi_k(\mathbf{x})$ described in Proposition 4 is

$$\begin{pmatrix} \mathsf{M}_{11} & \cdots & \mathsf{M}_{1N} & -\mathbf{e} \\ \vdots & \ddots & \vdots & \vdots \\ \mathsf{M}_{N1} & \cdots & \mathsf{M}_{NN} & -\mathbf{e} \\ h_1\mathbf{e}^T & \cdots & h_N\mathbf{e}^T & 0 \end{pmatrix} \begin{pmatrix} \mathbf{B}_1 \\ \vdots \\ \mathbf{B}_N \\ \bar{\phi}_k \end{pmatrix} = - \begin{pmatrix} \delta_{k1}\mathbf{e} \\ \vdots \\ \delta_{kN}\mathbf{e} \\ 0 \end{pmatrix}, \tag{4.14}$$

where $\mathbf{B}_j = (B_{j,1}, \ldots, B_{j,M_j})^T$ are the corresponding splitting probability line densities and the constant $\bar{\phi}_k$ is the spatially averaged splitting probability. After solving the system (4.14), the splitting probabilities are

$$\phi_k(\mathbf{x}) \approx \bar{\phi}_k - 2\pi \sum_{j=1}^{N} h_j \sum_{q=1}^{M_i} B_{j,q}\, G(\mathbf{x}; \mathbf{X}_{j,q}), \qquad \text{dist}(\mathbf{x}, \Gamma_j) \gg \mathcal{O}(\varepsilon) \quad j = 1, \ldots, N. \tag{4.15}$$

Errors in the numerical method. The trapezoidal rule is spectrally accurate for smooth periodic integrands [17]. After the subtraction of the chord kernel, the self-interaction integrands are continuous but have a local behavior of the form $|s - s'|$ at $s' = s$, arising from the curvature of Γ_j and the variations in the line densities, which results in a local discontinuity in the derivative (i.e. a corner). The corner produces an $\mathcal{O}(h^2)$ quadrature error, resulting in a scheme that converges as M^{-2} for $M \to \infty$. All other integrals are smooth and are computed with spectral accuracy. Higher-order accuracy can be obtained by using Richardson extrapolation or locally corrected trapezoidal rules [1, 36]. For the purposes of validating the asymptotic expansions, we find that this second-order method is sufficient.

Non-arclength parameterizations. In the derivation, above we assumed that the filament centerline is parameterized by arc-length $\mathbf{X} = \mathbf{X}(s)$. To treat simple closed filament centerlines $\tilde{\mathbf{X}}(t)$ that are not parameterized by arc-length, but instead on $0 \le t < 2\pi$, our approach is to numerically provide a map between t and s that can be interpolated with high precision. In particular, by computing $s = \int_0^t |\tilde{\mathbf{X}}'(\tau)|\, \mathrm{d}\tau$ and then interpolating the map to obtain equal spacing in arclength, the numerical discretization of the integral equations described above can be used. The map is sufficiently resolved numerically so that we can neglect any interpolation errors in comparison to the errors associated with the trapezoidal rule.

4.1 Examples: Ring filaments

In this subsection we validate our numerical method for a few configurations of ring or loop-type filaments, for which the intrinsic self-energy of the filament is known analytically.

As an example, we first consider one perfectly absorbing ring filament of radius r_0 of circular cross-section of radius ε in the $z = 0$ plane such as shown in Fig. 2(a). The integral system (2.19) was solved explicitly for this case in § 3 and it was determined in (3.2) that the line density is simply $A =\equiv 1/(3\pi D r_0)$. Secondly, we consider two identical perfectly absorbing rings with circular cross-section centered at $(0, 0, \pm z_0)$, in which symmetry implies that $A_1(s) = A_2(s)$ for all s. From (2.29), this implies that $A = 1/(6\pi D r_0)$. We

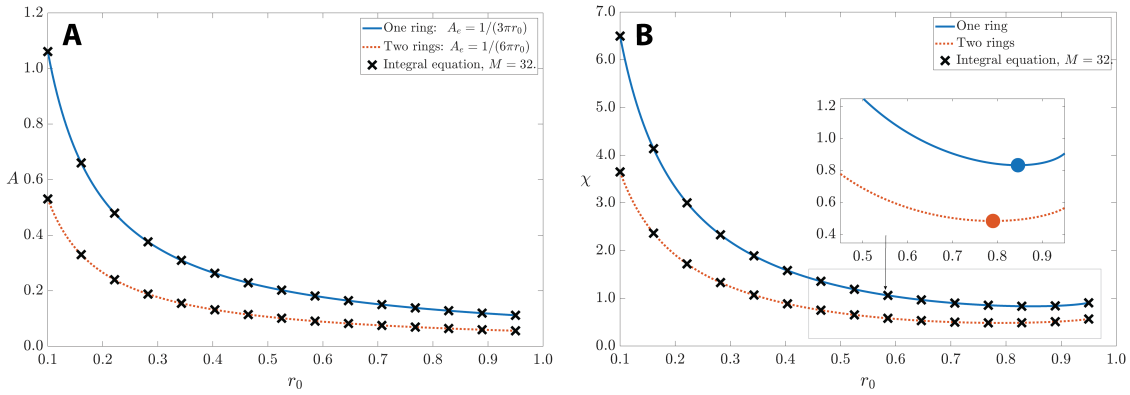


Figure 4: Convergence of the integral method in two examples: a single concentric ring of radius r_0 centered at the origin, and two concentric rings of radius r_0 on planes $z = \pm 0.1$, with $D = 1$ and $\varepsilon = 10^{-3}$. The numerical results by the integral equation solver (crosses) compare favorably with the exact solutions (lines) for A (Panel A) and χ (Panel B). The inset shows the local minimum of the MFRT in r_0.

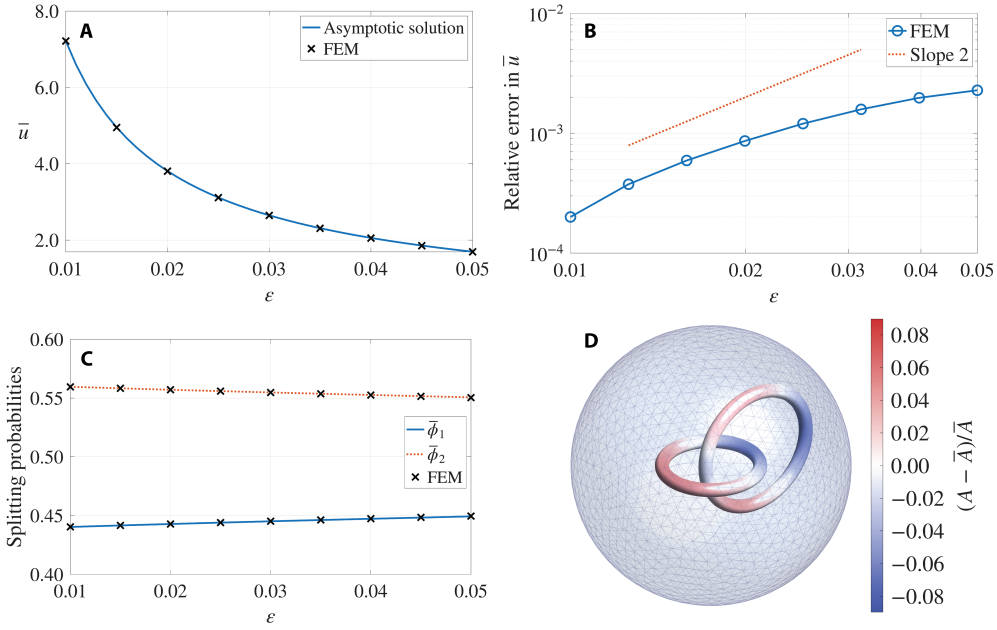


Figure 5: Validation of asymptotic reduction with full numerical solution (FEM) for the two filaments with common reactivity $b = 2$ and $d_c(2) = e^{-\frac{1}{2}}$. Panel A: Agreement between $\bar{u}$ from FEM solution and the χ determined from the solution of the integral equation (2.37). Panel B: The relative error $|\bar{u} - \chi|/\bar{u}$ as $\varepsilon \to 0$ indicating the validity of the leading order approximation. Panel C: Agreement of the splitting probabilities $\bar{\phi}_{1,2}$ with FEM and asymptotic method. Panel D: The spherical domain and filaments for $\varepsilon = 0.05$. The surfaces are shaded with relative fluxes $(A_i(s) - \bar{A}_i)/\bar{A}_i$ showing shielding near the center of the loop.

parameterize the two filament centerlines in terms of arclength as $\mathbf{X}_{\pm}(s) = (r_0 \cos(s/r_0), r_0 \sin(s/r_0), \pm z_0)^T$ with $0 < s < 2\pi r_0$. By scaling out A_e in (2.37), we find that the volume-averaged MFRT is

$$\chi = A_e \chi_0 \,, \quad \text{where} \quad \chi_0 = \log\left(\frac{8r_0}{\varepsilon}\right) + 2\pi \int_0^{2\pi r_0} R(\mathbf{X}_+(s); \mathbf{X}_+(s'))\, \mathrm{d}s' + 2\pi \int_0^{2\pi r_0} G\big(\mathbf{X}_+(s); \mathbf{X}_-(s')\big)\, \mathrm{d}s' \,, \tag{4.16}$$

where the two integral terms are independent of s by symmetry. In deriving (4.16) we used $\nu = -1/\log\varepsilon$, and $\mathcal{E}(s) = 2\log(8r_0)$ for the common intrinsic self-energy of the two filaments. In Figs. 4A-B, we show good agreement between the values of A and χ produced by the integral equation solution and the closed form solutions over a range of r_0 values for $\varepsilon = 10^{-3}$ and both the single ring and the two ring cases ($z_0 = 0.1$). In Fig. 4B, the inset compares the critical radii that minimize the global MFRTs for these two examples.

As a second example, we consider two interlacing ring filaments such as shown in Fig. 5D whose centerlines are given explicitly by

$$\Gamma_1 : \ \{\, z = 0,\ x^2 + y^2 = 0.35^2 \,\}, \qquad \Gamma_2 : \ \{\, y = 0,\ (x - 0.4)^2 + z^2 = 0.45^2 \,\}. \tag{4.17}$$

For this configuration we solve for the MFRT and splitting probabilities at various ε but assuming a uniform common reactivity $b = 2$, for which $d_c = e^{-1/2}$. The results are shown in Fig. 5. We observe in Figs. 5A and C that the asymptotic solution of the MFRT $\bar{u}$ and the splitting probabilities $\{\bar{\phi}_1, \bar{\phi}_2\}$ agree very closely with those computed from a full finite element simulation based on quadratic elements [22]. The relative error in the approximation of $\bar{u}$ is observed in Fig. 5B to exhibit an $\mathcal{O}(\varepsilon^2)$ scaling as $\varepsilon \to 0$. In Fig. 5D we show the geometry together with the filaments shaded by $(A_i(s) - \bar{A}_i)/\bar{A}_i$ for $\bar{A}_i = |\Gamma_i|^{-1} \int_{\Gamma_i} A_i(s)\, \mathrm{d}s$ when $\varepsilon = 0.05$. A shielding effect is observed in which the flux to the filaments is modulated by the competition of the neighboring geometry, through interactions with the other filament and the exterior boundary $\partial\Omega$.

4.2 Examples: torus-knot filaments

In this subsection, we consider torus-knot filaments that do not admit a convenient arclength parameterization and for which we must numerically compute their intrinsic self-energy.

A helical filament centerlines, parameterized by t, has the form

$$\mathbf{X}(t) = \Big(\big(r_0 + \rho_0 \cos(pt)\big) \cos(qt), \big(r_0 + \rho_0 \cos(pt)\big) \sin(qt), \rho_0 \sin(pt) \Big) \,, \qquad t \in [0, 2\pi) \,. \tag{4.18a}$$

For positive integers p and q, the curve (4.18a) is closed on $0 \le t < 2\pi$. Provided $\rho_0 < r_0$, it is a simple closed curve traversed exactly once if and only if $\gcd(p, q) = 1$. It then lies on a torus of major radius r_0 and minor radius ρ_0, winding q times around the z-axis and p times around the centerline, and therefore forms a (q, p) torus knot. This is the *unknot* when $p = 1$ or $q = 1$, and the *trefoil* when $\{p, q\} = \{2, 3\}$. The length of the centerline, with Jacobian $\mathrm{d}s = v(t)\, \mathrm{d}t$ where $v(t) \equiv |\mathbf{X}'(t)|$, is

$$L = \int_0^{2\pi} v(t)\, \mathrm{d}t \,, \qquad \text{and} \qquad v(t) \equiv \Big[\rho_0^2 p^2 + q^2 \big(r_0 + \rho_0 \cos(pt)\big)^2 \Big]^{\frac{1}{2}} . \tag{4.18b}$$

We consider four cases spanning a range of filament undulations parameterized on $0 \le t < 2\pi$ by:

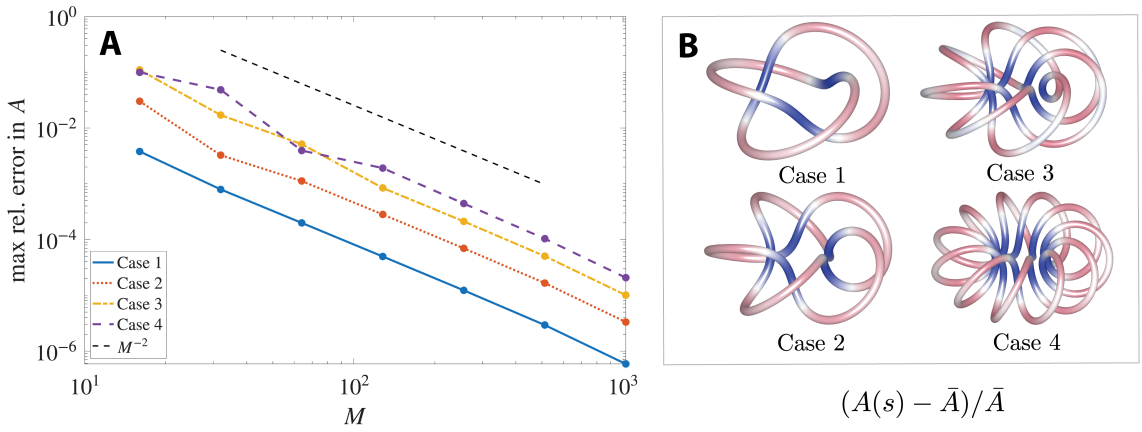


Figure 6: Convergence of the integral method. Panel A: The maximum relative error of A computed by the integral method, as a function of the number of discretization points M, for the four filaments described in (4.18), for $\varepsilon = 10^{-3}$. The expected M^{-2} convergence rate is shown by the dashed line, with larger errors associated with more wavelengths in the centerline. Panel B: plots of $(A(s)-\bar{A})/\bar{A}$ along the filament surface where $\bar{A} = |\Gamma|^{-1}\int_\Gamma A(s)\,\mathrm{d}s$. Red and blue indicates regions of larger and lower relative fluxes respectively.

$$\text{Case 1}: r_0 = 0.50\,, \quad \rho_0 = 0.20\,, \quad p = 3\,, \quad q = 2\,; \tag{4.19a}$$

$$\text{Case 2}: r_0 = 0.50\,, \quad \rho_0 = 0.25\,, \quad p = 5\,, \quad q = 2\,; \tag{4.19b}$$

$$\text{Case 3}: r_0 = 0.55\,, \quad \rho_0 = 0.30\,, \quad p = 7\,, \quad q = 3\,; \tag{4.19c}$$

$$\text{Case 4}: r_0 = 0.55\,, \quad \rho_0 = 0.30\,, \quad p = 11\,, \quad q = 2\,. \tag{4.19d}$$

We choose the cross-sectional radius to be $\varepsilon = 10^{-3}$ and $d_c = 1$ consistent with a perfectly absorbing filament. By setting such a small ε, our goal for this example is to estimate the order of the error in our numerical discretization of the integral equation with respect to the number of sub-intervals. In Fig. 6A we demonstrate the expected $\mathcal{O}(M^{-2})$ convergence rate of the relative errors in the integral method. The surface of each filament is shown in Fig. 6B colored with $(A(s) - \bar{A})/\bar{A}$ for $\bar{A} = |\Gamma|^{-1}\int_\Gamma A(s)\,\mathrm{d}s$ demonstrating filament curvature effects on the density.

For our final example, we will consider two perfectly absorbing helical filaments that have the same length, and we will determine whether the specific type of filament centerline and its location in the unit sphere has an appreciable affect on the global MFRT. We assume that the filaments have a circular cross-sectional radius of either $\varepsilon = 0.02$ or $\varepsilon = 0.05$. We will consider the following two cases:

$$\text{Case 5}: r_0 = 0.40\,, \quad \rho_0 = 0.2000\,, \quad p = 4\,, \quad q = 1\,, \quad \text{(Unknot)}\,; \tag{4.20a}$$

$$\text{Case 6}: r_0 = 0.40\,, \quad \rho_0 = 0.1366\,, \quad p = 3\,, \quad q = 2\,, \quad \text{(Trefoil knot)}\,. \tag{4.20b}$$

For both cases, the length of the filament centerline is $L \approx 5.68$, and so the surface area $2\pi\varepsilon L$ of the capturing set is the same for both helices. The filament centerlines are shown in Fig. 7.

By integrating (2.19) over Γ, we derive for each of the two curves that

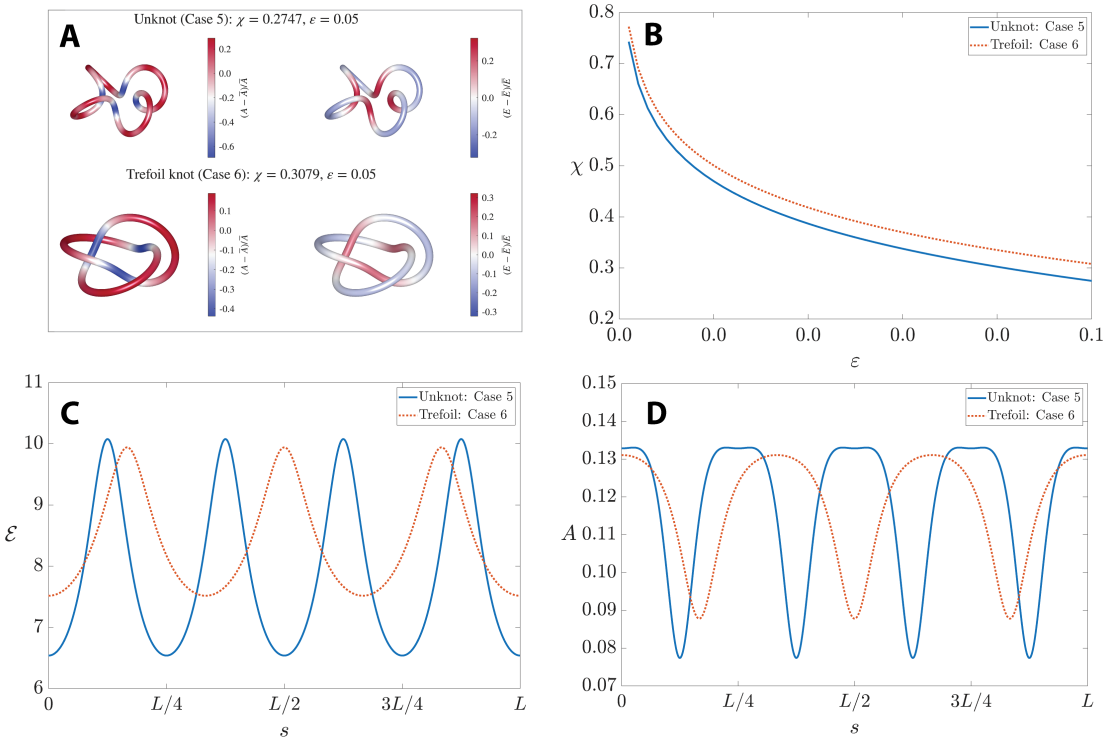


Figure 7: Solutions for the two helical filaments (4.18a) *and* (4.20) *depicting the unknot* (4.20a) *and the trefoil knot* (4.20b)*, respectively. The length of each centerline is* $L \approx 5.68$*. Panel A: The filaments with their relative intrinsic energies* $(\mathcal{E}(s) - \bar{\mathcal{E}})/\bar{\mathcal{E}}$ *and relative flux densities* $(A(s) - \bar{A})/\bar{A}$ *for* $\varepsilon d_c = 0.05$*. A strong shielding effect is observed. Panel B: The MFRT* χ *against* ε *for* $d_c = 1$ *demonstrating that the unknot generates a lower MFRT compared to Trefoil. Panel C: The intrinsic energies* $\mathcal{E}(s)$ *against arclength for the two filaments. Panel D: The flux densities* $A(s)$ *against arclength for the two filaments when* $\varepsilon d_c = 0.02$*.*

$$\chi = \frac{|\Omega|}{2\pi D\nu|\Gamma|} + \frac{1}{2|\Gamma|}\int_\Gamma A(s)\mathcal{E}(s)\,\mathrm{d}s + \frac{2\pi}{|\Gamma|}\int_\Gamma\int_\Gamma A(s)R\left(\mathbf{X}(s);\mathbf{X}(s')\right)\,\mathrm{d}s\,\mathrm{d}s'\,. \tag{4.21}$$

For each of the two examples in (4.20) we have $|\Gamma| \approx 5.68$, and the average distance from the origin does not differ substantially. As a result, we expect that the term associated with the regular part R, which accounts for the filaments interaction with the geometry, should be roughly similar for the two curves. However, the two helices differ considerably in their intrinsic energies owing to the different number of undulations. For these two examples, we show in the results of Fig. 7 that the unknot produces a lower MFRT. In Fig. 7 we show the filaments themselves together with their intrinsic self-energies and the flux densities for $\varepsilon d_c = 0.02$ and $\varepsilon d_c = 0.05$.

5 Extensions to related problems in diffusive capture

In this section we extend the asymptotic theory in two directions. In §5.1 we consider the effect of a heterogeneous diffusivity on the MFRT for a single filament, while in §5.2 we calculate the principal eigenvalue for the Laplacian for a domain with a single filament.

5.1 Heterogeneous diffusivity

We first extend (1.2) by allowing for a smooth heterogeneous diffusivity $D(\mathbf{x}) > 0$, so (with Itô interpretation)

$$\Delta_{\mathbf{x}}u = -\frac{1}{D(\mathbf{x})}\,,\quad \mathbf{x}\in\Omega\setminus\Gamma_\varepsilon\,;\qquad \varepsilon\partial_n u + bu = 0\,,\quad \mathbf{x}\in\partial\Gamma_\varepsilon\,;\qquad \partial_n u = 0\,,\quad \mathbf{x}\in\partial\Omega\,. \tag{5.1}$$

The asymptotic analysis of (5.1) for the single filament Γ_ε is very similar to that for the case of uniform diffusivity. More specifically, the construction of the solution in the inner region is identical up to order $\mathcal{O}(\varepsilon^2)$. As a result, the outer solution that incorporates all logarithmic corrections has the same singularity condition as $\mathbf{x}\to\mathbf{X}(s)$. In this way, we have that the outer solution satisfies

$$\Delta_{\mathbf{x}}u = -\frac{1}{D(\mathbf{x})} + 2\pi\int_\Gamma A(s)\delta(\mathbf{x}-\mathbf{X}(s))\,\mathrm{d}s\,,\quad \mathbf{x}\in\Omega\setminus\Gamma\,;\quad \partial_n u = 0\,,\quad \mathbf{x}\in\partial\Omega\,, \tag{5.2a}$$

$$u - A(s)\log|\mathbf{x}-\mathbf{X}(s)| \to \frac{A(s)}{\nu}\quad\text{as}\quad \mathbf{x}\to\mathbf{X}(s)\,,\quad s\in[0,L]\,, \tag{5.2b}$$

where $\nu = -1/\log[\varepsilon d_c(b)]$. From an application of the divergence theorem to (2.9a) we conclude that

$$\int_\Gamma A(s)\,\mathrm{d}s = \frac{1}{2\pi}\int_\Omega \frac{1}{D(\mathbf{x})}\,\mathrm{d}\mathbf{x}\,. \tag{5.3}$$

By adding and subtracting the term $|\Omega|^{-1}\int_\Omega [D(\mathbf{x})]^{-1}\,\mathrm{d}\mathbf{x}$ to the right-hand side of (5.2a), it is convenient to define $u_p(\mathbf{x})$ to be the unique solution to

$$\Delta u_p = -\frac{1}{D(\mathbf{x})} + \frac{1}{|\Omega|}\int_\Omega \frac{\mathrm{d}\mathbf{x}'}{D(\mathbf{x}')}\,,\quad \mathbf{x}\in\Omega\,;\qquad \partial_n u_p = 0\,,\quad \mathbf{x}\in\partial\Omega\,;\qquad \int_\Omega u_p\,\mathrm{d}\mathbf{x} = 0\,, \tag{5.4}$$

which is given in terms of the Neumann Green's function (1.4) by

$$u_p(\mathbf{x}) = \int_\Omega \frac{1}{D(\mathbf{x}')}G(\mathbf{x};\mathbf{x}')\,\mathrm{d}\mathbf{x}'\,. \tag{5.5}$$

We observe that when $D(\mathbf{x})$ is a constant in Ω, then $u_p \equiv 0$ since $\int_\Omega G(\mathbf{x};\mathbf{x}')\,\mathrm{d}\mathbf{x}' = 0$. By superposition, the solution to (5.2) is determined in terms of an unknown constant χ by

$$u(\mathbf{x}) = \chi + u_p(\mathbf{x}) - 2\pi \int_\Gamma A(s) G(\mathbf{x};\mathbf{X}(s))\,\mathrm{d}s\,, \quad \text{for} \quad \mathbf{x} \notin \Gamma\,, \tag{5.6}$$

from which it follows that $\chi = |\Omega|^{-1}\int_\Omega u(\mathbf{x})\,\mathrm{d}\mathbf{x}$. As a result, we conclude from (1.3) and (5.6) that the global MFRT is

$$\bar{u} = \chi + o(1)\,. \tag{5.7}$$

The remainder of the derivation of the integral equation for $A(s)$ parallels that for the uniform diffusivity case done in §2.2. The result is summarized as follows:

Proposition 7. *Let Γ be any smooth simple closed curve in Ω parameterized by arclength as $\mathbf{X}(s)$, which has an $\mathcal{O}(\varepsilon)$ cross-sectional diameter. In the limit $\varepsilon \to 0$, the asymptotic solution to* (5.1) *in the outer region at $\mathcal{O}(1)$ distances from Γ is*

$$u(\mathbf{x}) \sim \chi + u_p(\mathbf{x}) - 2\pi \int_\Gamma A(s) G(\mathbf{x};\mathbf{X}(s))\,\mathrm{d}s\,, \quad \textit{for} \quad \mathbf{x} \notin \Gamma\,, \tag{5.8}$$

where $u_p(\mathbf{x})$ is the solution (5.5) *to* (5.4)*, and where $A(s)$ and χ are solutions to the integral equation with constraint, defined for all $s \in [0, L]$ where $L = |\Gamma|$, by*

$$(\mathcal{K}A)(s) - u_p\left(\mathbf{X}(s)\right) = \chi\,, \qquad \int_\Gamma A(s)\,\mathrm{d}s = \frac{1}{2\pi}\int_\Omega \frac{\mathrm{d}\mathbf{x}}{D(\mathbf{x})}. \tag{5.9}$$

Here $\mathcal{K}$ is defined in (1.7)*, G is the Neumann Green's function with regular part R satisfying* (1.4).

Example: To illustrate the theory, we consider the unit sphere with an equatorial ring of radius r_0 centered at the origin. We will explore the effect on the global MFRT of a heterogeneous diffusivity that is symmetric with respect to the plane $z = 0$ but that is larger at the poles than it is on the equator. However, we will fix the harmonic mean of $D(\mathbf{x})$ to unity, by the constraint $\int_\Omega [D(\mathbf{x})]^{-1}\,\mathrm{d}\mathbf{x} = |\Omega|$ so that we can contrast our results for the MFRT with that for the case of a uniform diffusivity $D = 1$. For a heterogeneous diffusivity with smaller values near the equatorial filament, one would expect that the average MFRT is smaller (i.e. the expected time for capture is faster), than with a spatially uniform diffusivity.

To explore this idea, we consider the choice $1/D(\mathbf{x}) = \beta_1 - \beta_2 z^2$ where $\beta_1 > \beta_2 > 0$ in the unit sphere. Upon setting $\int_\Omega [D(\mathbf{x})]^{-1}\,\mathrm{d}\mathbf{x} = 4\pi/3$, we obtain that $5\beta_1 - \beta_2 = 5$. With this choice, $u_p(\mathbf{x})$ in (5.4) satisfies

$$\Delta u_p = \beta_2 z^2 - (\beta_1 - 1) = \beta_2\left(z^2 - 1/5\right)\,, \quad \mathbf{x} \in \Omega\,; \qquad \partial_n u_p = 0\,, \quad \mathbf{x} \in \partial\Omega\,; \qquad \int_\Omega u_p\,\mathrm{d}\mathbf{x} = 0\,, \tag{5.10}$$

which has the explicit solution in terms of $r = |\mathbf{x}|$ and z given by

$$u_p(r,z) = \beta_2\left(\frac{9}{700} + \frac{r^2}{70} - \frac{r^4}{140} + \frac{1}{14}(r^2-2)z^2\right)\,. \tag{5.11}$$

Evaluating (5.11) on the ring $r = r_0$ on the plane $z = 0$ we get

$$u_p(r_0) = \frac{\beta_2}{70}\left(\frac{7}{5} - \frac{1}{2}\left(1 - r_0^2\right)^2\right)\,. \tag{5.12}$$

We observe that $u_p(r_0) > 0$ on $0 \le r_0 \le 1$ and that u_p is monotone increasing in r_0.

Finally, upon substituting (5.12) into (5.9) we conclude that the global MFRT χ with this choice of heterogeneous diffusivity is related to that with uniform diffusivity $D = 1$, labeled by $\chi_{\rm unif}$, by a simple shift $\chi = \chi_{\rm unif} - u_{0p}(r_0)$, so that

$$\chi = \chi_{\rm unif} - \frac{\beta_2}{70}\left(\frac{7}{5} - \frac{1}{2}\left(1 - r_0^2\right)^2\right), \tag{5.13}$$

where $\chi_{\rm unif}$ is given in (3.9) when $D = 1$. Here $\beta_2 > 0$ is any solution to $5\beta_1 - \beta_2 = 5$ with $\beta_1 > \beta_2 > 0$. We conclude, as expected, that the global MFRT χ decreases when the Brownian particle experiences a smaller diffusivity near the equatorial plane where the capturing filament is located.

In particular, if we set $\beta_2 = 1$ then $\beta_1 = 6/5$, and the heterogeneous diffusivity is $D(\mathbf{x}) = \left(\frac{6}{5} - z^2\right)^{-1}$, which is 6 times higher at the poles $z = \pm 1$ than on the equatorial plane $z = 0$. Setting $\varepsilon d_c = 0.02$ and evaluating (5.13) at the previously optimal ring radius $r_0 \approx 0.7680$ for the uniform diffusivity $D = 1$ where $\chi_{\rm unif} \approx 0.4406$ (see second row of Table 1), we obtain that $\chi \approx 0.4218$, which is approximately a 4.3% reduction in the global MFRT due to this specific heterogeneous diffusivity.

5.2 The principal eigenvalue of the Laplacian

In this subsection we consider the Laplacian eigenvalue problem in a bounded 3-D domain with one partially reactive filament boundary Γ_ε, formulated, apart from a normalization of the eigenfunction, as

$$\Delta u + \lambda u = 0\,, \quad \mathbf{x} \in \Omega \setminus \Gamma_\varepsilon\,; \qquad \varepsilon \partial_n u + b u = 0\,, \quad \mathbf{x} \in \partial\Gamma_\varepsilon\,; \qquad \partial_n u = 0\,, \quad \mathbf{x} \in \partial\Omega\,. \tag{5.14}$$

We seek to determine an approximation of the lowest eigenvalue of (5.14) that is accurate to all orders in $\nu \equiv -1/\log[\varepsilon d_c]$; i.e. that effectively "sums" all logarithmic terms in ε. Motivated by the related analyses in [58] and [40] for Laplacian eigenvalues in 2-D domains with spatially localized traps, we will expand λ and the corresponding eigenfunction u in the outer region as

$$\lambda = \lambda_0(\nu) + \mathcal{O}(\zeta)\,; \qquad u(\mathbf{x}) = u_0(\mathbf{x};\nu) + \mathcal{O}(\zeta) \quad \text{for} \quad \text{dist}(\mathbf{x},\Gamma) \gg \mathcal{O}(\varepsilon)\,, \tag{5.15}$$

where the correction ζ is transcendentally small with respect to ν in the sense that $\zeta \ll \nu^k$ for any $k > 0$.

The inner expansion near the filament centerline is identical to that for the MFRT problem, and so in place of (2.9) we have in the outer region that

$$\Delta u_0 + \lambda_0 u_0 = 2\pi \int_\Gamma A(s)\delta(\mathbf{x} - \mathbf{X}(s))\,\mathrm{d}s\,, \quad \mathbf{x} \in \Omega \setminus \Gamma\,; \qquad \partial_n u_0 = 0\,, \quad \mathbf{x} \in \partial\Omega\,, \tag{5.16a}$$

$$u_0 - A(s)\log|\mathbf{x} - \mathbf{X}(s)| \to \frac{A(s)}{\nu} \quad \text{as} \quad \mathbf{x} \to \mathbf{X}(s)\,, \quad s \in [0, L)\,, \tag{5.16b}$$

for $L = |\Gamma|$ and some line density $A(s)$. The solution to (5.16) is represented as

$$u_0(\mathbf{x};\lambda_0) = -2\pi \int_\Gamma A(s) G_h(\mathbf{x};\mathbf{X}(s);\lambda_0)\,\mathrm{d}s\,, \tag{5.17}$$

where for convenience below it is useful to enforce the normalization condition $\int_\Gamma A(s)\,\mathrm{d}s = 1$ for the eigenfunction. In (5.17), $G_h(\mathbf{x};\boldsymbol{\xi};\lambda_0)$ is the Helmholtz Green's function satisfying

$$\Delta G_h + \lambda_0 G_h = -\delta(\mathbf{x} - \boldsymbol{\xi})\,, \quad \mathbf{x} \in \Omega\,; \qquad \partial_n G_h = 0\,, \quad \mathbf{x} \in \partial\Omega\,, \tag{5.18a}$$

which can be decomposed into a singular part and a smooth regular part $R_h(\mathbf{x};\boldsymbol{\xi};\lambda_0)$ as

$$G_h(\mathbf{x};\boldsymbol{\xi};\lambda_0) = \frac{1}{4\pi|\mathbf{x} - \boldsymbol{\xi}|} + R_h(\mathbf{x};\boldsymbol{\xi};\lambda_0)\,. \tag{5.18b}$$

When Ω is the unit sphere, an explicit infinite series representation for R_h is given in (E.1) of Appendix E.

The derivation of the integral equation that determines $A(s)$ and λ_0 is the same as in §2.2, and yields

$$\frac{A(s)}{\nu}+\frac{1}{2}A(s)\mathcal{E}(s)-\frac{1}{2}\int_\Gamma \frac{A(s)-A(s')}{|\mathbf{X}(s)-\mathbf{X}(s')|}\,\mathrm{d}s'+2\pi\int_\Gamma A(s')R_h(\mathbf{X}(s);\mathbf{X}(s');\lambda_0)\,\mathrm{d}s'=0\,;\quad \int_\Gamma A(s)\,\mathrm{d}s=1\,, \tag{5.19}$$

where $\nu=-1/\log[\varepsilon d_c(b)]$. To approximate the lowest eigenvalue of λ_0 of (5.14) that includes all logarithmic corrections, we must determine the smallest positive value $\lambda_0=\lambda_0^\star(\nu)$ for which the integral equation (5.19) has a line density $A(s)$ that does not vanish identically on Γ. A numerical discretization of (5.19) would lead to a nonlinear matrix eigenvalue problem to approximate $\lambda_0^\star$. We shall refer to $\lambda_0^\star(\nu)$ as the *log-summed* approximation to the lowest eigenvalue of (5.14).

5.2.1 A two-term expansion

We first derive a two-term-in-ν expansion for the lowest root λ_0 that is applicable to arbitrary Ω, and we will relate it to the two-term expansion of the global MFRT derived in (2.25a) of Proposition 2. To do so, we first readily derive from a perturbation expansion of the PDE (5.18a) (see [40]) that

$$R_h(\mathbf{x};\boldsymbol{\xi};\lambda_0)=-\frac{1}{\lambda_0|\Omega|}+R(\mathbf{x};\boldsymbol{\xi})+\mathcal{O}(\lambda_0)\,,\quad \text{as}\quad \lambda_0\to 0\,, \tag{5.20}$$

where $R(\mathbf{x};\boldsymbol{\xi})$ is the regular part of the Neumann Green's function in (1.4b). Upon substituting (5.20) into (5.19) we obtain for $\lambda_0\ll 1$

$$\frac{A(s)}{\nu}-\frac{2\pi}{\lambda_0|\Omega|}\int_\Gamma A(s)\,\mathrm{d}s+\left(\frac{1}{2}A(s)\mathcal{E}(s)-\frac{1}{2}\int_\Gamma\frac{A(s)-A(s')}{|\mathbf{X}(s)-\mathbf{X}(s')|}\,\mathrm{d}s'+2\pi\int_\Gamma A(s')R(\mathbf{X}(s);\mathbf{X}(s'))\,\mathrm{d}s'\right)=\mathcal{O}(\lambda_0)\,. \tag{5.21}$$

We then substitute the expansions

$$A(s)=A_0(s)+\nu A_1(s)+\mathcal{O}(\nu^2)\,,\qquad \lambda_0=\nu\lambda_{00}+\nu^2\lambda_{01}+\mathcal{O}(\nu^3)\,, \tag{5.22}$$

into (5.21) to obtain, subject to $\int_\Gamma A(s)\,\mathrm{d}s=1$, that

$$\begin{aligned}\frac{A_0}{\nu}-\frac{2\pi}{\nu|\Omega|\lambda_{00}}\left(1+\frac{\nu\lambda_{01}}{\lambda_{00}}\right)^{-1}\int_\Gamma (A_0+\nu A_1)\,\mathrm{d}s'\\ +A_1+\frac{1}{2}A_0\mathcal{E}(s)++2\pi\int_\Gamma A_0(s')R(\mathbf{X}(s);\mathbf{X}(s'))\,\mathrm{d}s'=\mathcal{O}(\lambda_0)\,.\end{aligned} \tag{5.23}$$

From the leading-order $\mathcal{O}(\nu^{-1})$ terms in (5.23) we conclude that

$$A_0(s)=\frac{2\pi}{\lambda_{00}|\Omega|}\int_\Gamma A_0(s)\,\mathrm{d}s\,,\quad \forall\, s\in[0,L)\,. \tag{5.24}$$

As such, $A_0(s)$ must be a constant, and from $\int_\Gamma A_0(s)\,\mathrm{d}s=1$, we get $A_0=1/|\Gamma|$. Then, (5.24) yields that

$$\lambda_{00}=\frac{2\pi|\Gamma|}{|\Omega|}\,. \tag{5.25}$$

By collecting the $\mathcal{O}(1)$ terms in (5.23), and using $\int_\Gamma A_1(s)\,\mathrm{d}s=0$, we conclude that

$$-\frac{2\pi\lambda_{01}}{|\Omega|\lambda_{00}^2}=A_1(s)+\frac{1}{2|\Gamma|}\mathcal{E}(s)+\frac{2\pi}{|\Gamma|}\int_\Gamma R(\mathbf{X}(s);\mathbf{X}(s'))\,\mathrm{d}s'\,,\quad \forall\, s\in[0,L)\,. \tag{5.26}$$

Instead of determining $A_1(s)$, we can obtain λ_{01} by simply integrating (5.26) over Γ after using $\int_\Gamma A_1\,\mathrm{d}s=0$. We summarize our resulting two-term expansion for the lowest eigenvalue of (5.14) as follows:

Proposition 8. *In the limit $\nu = -1/\log[\varepsilon d_c] \to 0$, the lowest eigenvalue for* (5.14) *has the explicit two-term approximation*

$$\lambda_0 \sim \frac{2\pi\nu|\Gamma|}{|\Omega|}\left(1 - \frac{\nu}{2|\Gamma|}\int_\Gamma \mathcal{E}(s)\,\mathrm{d}s - \frac{2\pi\nu}{|\Gamma|}\int_\Gamma\int_\Gamma R\left(\mathbf{X}(s);\mathbf{X}(s')\right)\,\mathrm{d}s\,\mathrm{d}s' + \mathcal{O}(\nu^2)\right). \tag{5.27}$$

Here R is the regular part of the Neumann Green's function in (1.4b) *and $\mathcal{E}(s)$ is the intrinsic self-energy of Γ given by* (2.17).

Upon comparing (5.27) with the corresponding two-term expansion of $\bar{u} \approx \chi$ in (2.25a), we conclude up to two-orders in ν we have the expected correspondence

$$\chi = \frac{1}{D\lambda_0} + \mathcal{O}(\nu)\,, \quad \text{where} \quad \lambda_0 = \nu\lambda_{00} + \nu^2\lambda_{01} + \mathcal{O}(\nu^3)\,. \tag{5.28}$$

It is unclear whether this relation holds for all logarithmic orders. As a result, for a concentric equatorial ring filament of radius r_0 in the unit sphere, we can use (3.9) for χ to obtain the two-term approximation

$$\lambda_0 \sim 3\pi r_0\nu\left[1 + r_0\nu\left(\frac{\log(8r_0)}{r_0} + 2K(r_0^2) + \pi\left(r_0^2 + \log 2 - \frac{14}{5}\right) + \frac{J(r_0)}{2}\right)\right]^{-1}, \tag{5.29}$$

which is asymptotically equivalent to (5.27). In (5.29), $K(m)$ is the complete elliptic integral and $J(r_0)$ is defined in (3.7).

5.2.2 Summing the log expansion for a ring filament

In an arbitrary 3-D domain with an arbitrary filament shape, a full numerical implementation of (5.19) is needed to compute the log-summed appproximation $\lambda_0^\star$ in terms of a numerically computable R_h, e.g., such as from a fast-integral method. For the unit sphere where R_h has an infinite series expansion, a numerical discretization of (5.19) would lead to a nonlinear matrix eigenvalue problem to approximate $\lambda_0^\star$.

However, in the special case when Ω is the unit sphere and when Γ is an equatorial ring of radius r_0, we now show how to determine $\lambda_0^\star$ from a simple root-finding problem. For this configuration, it follows by symmetry that the line density has the constant value $A(s) = 1/L$, with $L = 2\pi r_0$. Therefore, from (5.19) with $\mathcal{E}(s) = 2\log(8r_0)$ we obtain that λ_0 satisfies

$$\int_\Gamma R_h(\mathbf{X}(s);\mathbf{X}(s');\lambda_0)\,\mathrm{d}s' = -\frac{1}{2\pi}\left[\frac{1}{\nu} + \log(8r_0)\right] = -\frac{1}{2\pi}\log\left(\frac{8r_0}{\varepsilon d_c}\right). \tag{5.30}$$

By using an infinite series representation of R_h, in Appendix E we show that the determination of $\lambda_0^\star$ can be reduced to determining the smallest positive root of $\mathcal{N}(\lambda_0) = 0$, defined by

$$\mathcal{N}(\lambda_0) \equiv \frac{1}{2\pi}\log\left(\frac{8r_0}{\varepsilon d_c}\right) + \sum_{k=0}^{\infty} M_k(\lambda_0, r_0)\,; \qquad M_k(\lambda_0, r_0) \equiv \left[\sqrt{\lambda_0}r_0\left(2k + \frac{1}{2}\right)H_{2k} - \frac{1}{2}\right]\left(\frac{(2k)!}{2^{2k}(k!)^2}\right)^2, \tag{5.31a}$$

where $H_{2k} = H_{2k}(\lambda_0, r_0)$ is defined by

$$H_{2k}(\lambda_0, r_0) \equiv \left[y_{2k}'(\sqrt{\lambda_0})j_{2k}(\sqrt{\lambda_0}r_0) - j_{2k}'(\sqrt{\lambda_0})y_{2k}(\sqrt{\lambda_0}r_0)\right]\frac{j_{2k}(\sqrt{\lambda_0}r_0)}{j_{2k}'(\sqrt{\lambda_0})}\,. \tag{5.31b}$$

Here $j_{2k}(z)$ and $y_{2k}(z)$ are the spherical Bessel functions of the first and second kind of order $2k$.

With regards to numerically computing the root to $\mathcal{N}(\lambda_0) = 0$, we can readily estimate that $M_k = \mathcal{O}\left(r^{4k+1}/k\right)$ for large k by using Stirling's approximation and the large-order approximation of the spherical

Bessel functions. As a result, M_k has a power-law decay as k increases when r is not too close to the boundary $r = 1$. For $r_0 = 0.4$, and by retaining only 10 terms in the sum in (5.31a), in Fig. 8(a) we plot $\mathcal{N}(\lambda_0)$ versus λ_0 when $\varepsilon d_c = 0.02$ showing the existence of a root. In fact, retaining only 3 terms in the sum provides three decimal places of accuracy for the root. By tracking this root as εd_c is varied, in Fig. 8(b) and Table 4 we compare the log-summed approximation $\lambda_0^\star(\nu)$ with its corresponding one-term approximation $\lambda \sim 3\pi\nu r_0$ and two-term approximation from (5.29). The full numerical FEM results are also shown. We observe that the one-term approximation is poor unless ε is extremely small, while the two-term appproximation decently predicts $\lambda_0^\star$ to within 3% only for $\varepsilon d_c \leq 0.02$. From this table, we see that the log-summed result is within 4.7% of the full numerical result even when $\varepsilon = 0.10$.

For fixed ε, it was shown in Apppendix A.1 that $d_c(b)$ is monotone increasing in the reactivity b of the filament. As a result, we observe from Fig. 8(b) that the time-scale for capture of a Brownian particle, determined by $1/\lambda_0^\star$, is smaller as b increases, as expected intuitively. Moreover, by changing the cross-sectional shape of the filament from a disk or its reactivity, we can still use Fig. 8(b) after simple computing $d_c(b)$ numerically. For instance for an elliptical cross-section $\partial\mathcal{B}$ of semi-axes $a_1 = 1$ and $a_2 = 2$ with $b = 1$, we calculate $d_c(b) \approx 0.7725$ [26]. As a result, we conclude that a perfectly absorbing filament with a circular cross-sectional radius ε_0 with $\varepsilon_0 \equiv \varepsilon d_c = \varepsilon 0.7725$ would have the same $\lambda_0^\star$ as that for the partially reactive elliptical cross-section.

εd_c	λ_0 (1-term)	λ_0 (2-term)	$\lambda_0^\star$ (log-summed)	λ_0 (num)	% error
0.005	0.7115	0.8543	0.8447	0.8449	0.02
0.01	0.8183	1.0135	0.9975	0.9983	0.08
0.02	0.9637	1.2456	1.2161	1.2196	0.28
0.05	1.2584	1.7865	1.7016	1.7263	1.4
0.10	1.6373	2.6603	2.3993	2.5189	4.7

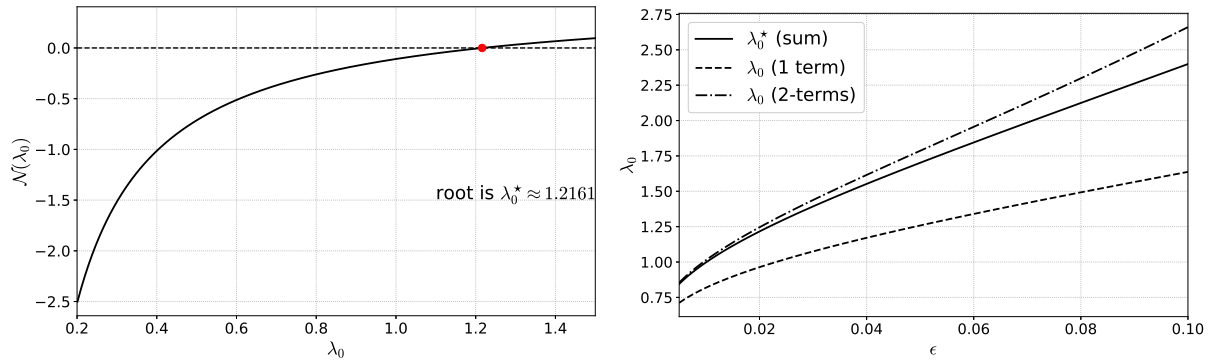
Table 4: Comparison of one-term $\lambda_0 \sim 3\pi\nu r_0$, and the two-term approximation in (5.29) *for the lowest eigenvalue of* (5.14) *for an equatorial ring filament of radius $r_0 = 0.4$ in the unit sphere with the corresponding log-summed approximation $\lambda_0^\star$ given by the smallest root of* (5.31) *and the FEM full numerical result λ_0 (num). The percentage error in the last column is between the log-summed and the FEM numerical result. This error is less than* 1.4% *on the range $\varepsilon \leq 0.05$.*

6 Fragmenting a filament into N uniformly-spaced small targets

We revisit the MFRT problem (1.2) for a perfectly absorbing filament Γ_ε of circular cross-sectional radius ε and of length L satisfying

$$\Delta_{\mathbf{x}} u = -\frac{1}{D}\,, \quad \mathbf{x} \in \Omega \setminus \Gamma_\varepsilon\,; \qquad u = 0\,, \quad \mathbf{x} \in \partial\Gamma_\varepsilon\,; \qquad \partial_n u = 0 \quad \mathbf{x} \in \partial\Omega\,. \tag{6.1}$$

Suppose that we fragment the filament Γ_ε, replacing it by a string of N identical perfectly absorbing small targets $\Omega_{\sigma,j}$ of diameter $\mathcal{O}(\sigma)$, referred to as *microtraps*, that are uniformly spaced in arclength along the filament centerline Γ. Examples of such fragmentation for a straight filament, an equatorial ring filament, and a Trefoil knot filament are shown in Fig. 9 (recall also Fig. 2 of §3). The rescaled canonical shape of a 3-D microtrap is labeled by $\Omega_0 \equiv \Omega_{\sigma,j}/\sigma$ (for example, the unit sphere, or a flat disk in 3-D) having capacitance C. We place N microtraps $\Omega_{\sigma,j}$, with $j = 1, \ldots, N$, along the centerline Γ of the filament Γ_ε, uniformly spaced and with their orientation aligned with the tangent of the centerline. The absorbing set,



(a) $\mathcal{N}(\lambda_0)$ *vs.* λ_0 *(b)* λ_0 *vs.* ε

Figure 8: Approximation of the lowest eigenvalue λ_0 *of the Laplacian in the unit sphere for a perfectly absorbing equatorial filament with ring radius* $r_0 = 0.4$ *and cross-sectional radius* ε*. Left:* $\mathcal{N}(\lambda_0)$*, defined in* (5.31) *versus* λ_0 *for* $\varepsilon = 0.02$ *showing the existence of a root* $\lambda_0^\star$ *for the log-summed approximation. Right: Comparison of the one-term* $\lambda_0 \sim 3\pi r_0 \nu$ *and two-term approximations from* (5.29) *with the log-summed approximation, computed from the zero of* $\mathcal{N}(\lambda_0)$ *in* (5.31)*, as* ε *is varied.*

resulting from the union of these N microtraps, is denoted by F_σ, which we shall refer to as the *fragmented filament.*

Our goal is to establish the relation between ε and σ for which the global MFRT for a filament of circular cross-sectional radius ε is asymptotically the same as that for the fragmented filament F_σ. In particular, we will show that the relation (3.26) derived for the specific case of the fragmentation of an equatorial filament in the unit sphere applies for an arbitrary filament in Ω, but only in the *transition scaling regime* for which $\mathcal{O}(\sigma) \ll L/N \ll \mathcal{O}(1)$. Since for $L/N \ll 1$ the fragmentation of a filament is only felt locally, the filament centerline is nearly straight between adjacent microtraps. The other requirement that $L/N \gg \mathcal{O}(\sigma)$ implies that adjacent microtraps are still separated by distances asymptotically larger than their $\mathcal{O}(\sigma)$ diameters. Owing to the uniform spacing of microtraps on the filament centerline, the considerations above suggest we need only consider a new inner problem on a $L/N \ll 1$ length scale that contains a single microtrap on a smaller $\mathcal{O}(\sigma)$ length-scale but that has a locally straight centerline. This solution can then be extended periodically down the filament. The analysis of this new inner problem shows that the effect of fragmentation in the scaling regime $\mathcal{O}(\sigma) \lesssim L/N \ll \mathcal{O}(1)$ is only to change the logarithmic capacitance of a filament. More specifically, our analysis shows that the MFRT for the fragmented filament is asymptotically equivalent to that for a full unfragmented filament, when the cross-sectional radius ε is appropriately related to N, σ, and the capacitance C of the microtrap. As a result, to determine the MFRT for a fragmented filament we need only redefine ε in $\nu = -1/\log\varepsilon$ in the Fredholm integral equation derived in (2.19) of Proposition 1. Our main result, which we derive systematically in Appendix F, is as follows:

Proposition 9. *Let* $\bar{u}_{\Gamma_\varepsilon}$ *and* $\bar{u}_{F_\sigma}$ *be the global MFRTs for the perfectly absorbing filament* Γ_ε *with a circular cross-section of radius* ε *and for its fragmented version* F_σ*, respectively. Denote by* $2a \equiv L/(N\sigma)$ *the spacing between adjacent microtraps of* F_σ*, scaled relative to the common size* σ *of each microtrap. In the limit* $N/L \gg 1$*,* $\sigma \ll 1$ *we have* $\bar{u}_{\Gamma_\varepsilon} \sim \bar{u}_{F_\sigma}$ *when*

$$\varepsilon = \sigma \exp\left(-\omega\left(a\right)\right) . \tag{6.2}$$

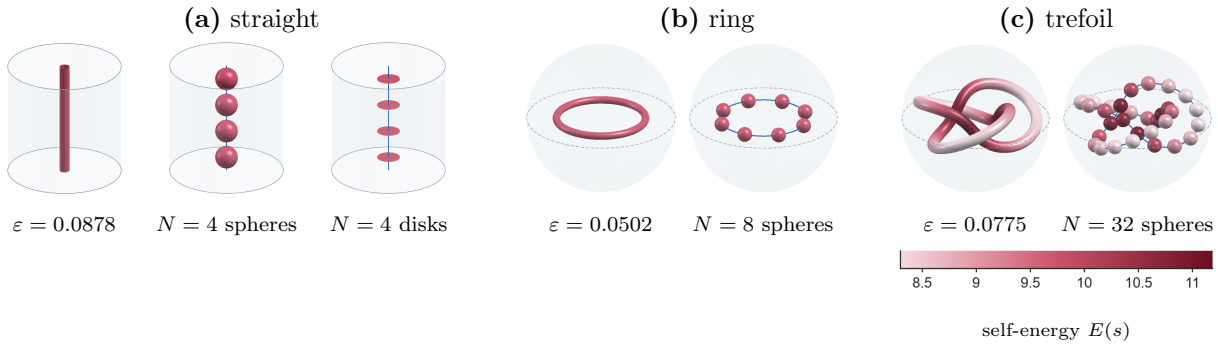


Figure 9: Filaments vs. fragmented filaments. (a) Straight cylinder of height $L = 2$ and unit radius with a thin filament centered on the vertical axis that is fragmented into four small spheres or disks of radius $\sigma = 0.2$. The global MFRT (6.6) *for a circular filament of cross-sectional radius $\varepsilon = 0.0878$ is asymptotically equivalent to that of the four disks. (b) Equatorial filament of radius $\varepsilon = 0.0502$ and its equivalent fragmentation into 8 spherical microtraps of radius $\sigma = 0.1$. (c) Trefoil knot* (4.18a) *with $p = 3$, $q = 2$, $r_0 = 0.6$ and $\rho_0 = 0.25$ and its equivalent fragmentation into 32 spherical microtraps of radius $\sigma = 0.1$. Color-coded by the intrinsic self-energy $\mathcal{E}(s)$ of the filament centerline from* (2.17).

Here $\omega = \omega(a)$, referred to as the infinite slab capacitance, is defined in terms of the far-field behavior of the solution to the new canonical inner problem

$$\begin{aligned} &\Delta V_c = 0\,, \quad |Z| < a\,, \quad (X,Y,Z) \in \mathbb{R}^3 \setminus \Omega_0\,, \\ &V_c = 0\,, \quad (X,Y,Z) \in \partial\Omega_0\,; \qquad V_c(X,Y,a) = V_c(X,Y,-a)\,, \quad V_{cZ}(X,Y,a) = V_{cZ}(X,Y,-a)\,, \\ &V_c \sim \log(\rho) + \omega\,, \quad \text{as} \quad \rho \equiv \sqrt{X^2+Y^2} \to \infty\,, \end{aligned} \tag{6.3}$$

where Ω_0 is centered at the origin $(X,Y,Z) = (0,0,0)$. For $a = \mathcal{O}(1)$, corresponding to $N/L = \mathcal{O}(\sigma^{-1})$, we need to determine $\omega = \omega(a)$ numerically. However, in the transition scaling regime for which $a \gg 1$, we have

$$\omega \sim \frac{a}{C} - \log(4a) + \gamma_e\,, \tag{6.4}$$

where γ_e is Euler's constant, so that

$$\varepsilon \sim \frac{2L}{N} \exp\left(-\frac{L}{2N\sigma C} - \gamma_e\right), \quad \text{for} \quad \frac{L}{N\sigma} \gg 1\,. \tag{6.5}$$

Here C is the capacitance of the microtrap Ω_0 defined by the local problem (3.15). *Two special cases are $C = 1$ if Ω_0 is the unit ball, and $C = 2/\pi$ when Ω_0 is a flat unit disk.*

This new canonical inner problem for V_c for a fragmented filament with perfectly absorbing microtraps replaces the inner problem (2.3) for a full filament of cross-sectional radius ε. Recall from (2.25a) that, to leading-order, we have $\bar{u} \sim \frac{|\Omega|}{2\pi DL}\log(1/\varepsilon)$ for a perfectly absorbing filament of circular cross-sectional radius ε. By using (6.5), in the limit $\sigma \to 0$ we get to leading-order that $-\log\varepsilon \sim L/(2N\sigma C)$ so that for the fragmented filament we have $\bar{u} \sim \frac{|\Omega|}{4\pi DN\sigma C}$. This latter estimate agrees with the leading-order result for N identical microtraps inside a 3-D domain Ω (see [13]). Effectively, filament fragmentation provides a transition between the $\mathcal{O}(-\log\varepsilon)$ behavior in 2-D and the $\mathcal{O}(\sigma^{-1})$ scaling of spatially localized traps in 3-D. We now consider the three specific examples of fragmented filaments in Fig. 9.

Straight vertical filament inside a cylinder. Let Ω be a cylinder of height L and radius 1 that contains a straight vertical filament Γ_ε with circular cross-sectional radius ε that is centered on the axis of

symmetry (see Fig. 9(a) (left)). Owing to radial symmetry, an exact result for the global MFRT for the filament is available, and we calculate from the solution to $(ru_r)_r = -r/D$ with $u_r(1) = 0$ and $u(\varepsilon) = 0$ that

$$\bar{u}_{\Gamma_\varepsilon} = \frac{1}{D}\left[\frac{\log(1/\varepsilon)}{2(1-\varepsilon^2)} - \frac{3}{8} + \frac{\varepsilon^2}{8}\right]. \tag{6.6}$$

To test our main result in Proposition 9 when $D = 1$, we take $L = 2$ and fragment Γ_ε into N small spheres of radius σ, uniformly spaced as shown in Fig. 9(a) (middle). Since $C = 1$ we predict from (6.5) that $\varepsilon \sim \frac{4}{N}\exp\left(-\frac{1}{N\sigma} - \gamma_e\right)$ when $\sigma \ll L/N \ll 1$. To compute full numerical solutions, we observe by symmetry that this problem is equivalent to the MFRT problem for a single sphere at the center of a cylinder of height L/N. The resulting 2-D problem in (r, z) is readily solved numerically to high accuracy (see Appendix F.2). A comparison between the asymptotic predictions and the full numerical results is shown in Table 5.

N	a	ε_{asy}	ε_ω	$\bar{u}_{F_\sigma,\,\text{num}}$	$\bar{u}_{\Gamma_\varepsilon}(\varepsilon_{\text{asy}})$	$\bar{u}_{\Gamma_\varepsilon}(\varepsilon_\omega)$	err_{asy}	err_ω
$\sigma = 0.2$								
1	5.000	0.01513	0.01513	1.75068	1.72097	1.72095	+1.73%	+1.73%
2	2.500	0.09217	0.09226	0.83906	0.82831	0.82787	+1.30%	+1.35%
3	1.667	0.1414	0.1424	0.62373	0.62555	0.62237	−0.29%	+0.22%
4	1.250	0.1609	0.1652	0.55216	0.56611	0.55402	−2.46%	−0.34%
$\sigma = 0.1$								
1	10.000	1.020×10^{-4}	1.020×10^{-4}	4.23418	4.22046	4.22046	+0.33%	+0.33%
2	5.000	0.007566	0.007566	2.07314	2.06718	2.06717	+0.29%	+0.29%
4	2.500	0.04609	0.04613	1.16966	1.16715	1.16669	+0.22%	+0.25%
8	1.250	0.08043	0.08259	0.88040	0.89420	0.88135	−1.54%	−0.11%
9	1.111	0.08215	0.08582	0.86186	0.88396	0.86281	−2.50%	−0.11%
$\sigma = 0.05$								
1	20.000	4.629×10^{-9}	4.629×10^{-9}	9.22963	9.22046	9.22046	+0.10%	+0.10%
2	10.000	5.098×10^{-5}	5.098×10^{-5}	4.56864	4.56703	4.56703	+0.04%	+0.04%
4	5.000	0.003783	0.003783	2.41523	2.41365	2.41364	+0.07%	+0.07%
8	2.500	0.02304	0.02306	1.51158	1.51125	1.51079	+0.02%	+0.05%
16	1.250	0.04022	0.04130	1.22108	1.23456	1.22144	−1.09%	−0.03%
17	1.176	0.04074	0.04217	1.21074	1.22817	1.21110	−1.42%	−0.03%
18	1.111	0.04107	0.04291	1.20213	1.22411	1.20248	−1.80%	−0.03%
19	1.053	0.04125	0.04354	1.19487	1.22193	1.19520	−2.21%	−0.03%

Table 5: MFRT results when $D = 1$ for the straight filament in the cylinder ($L = 2$) versus that for the fragmented filament with N small spheres of radius σ on its axis of symmetry.

In Table 5, $a = 1/(N\sigma)$ is half the distance between the centers of adjacent spheres, rescaled by their common radius σ, while ε_{asy} and ε_ω are given by (6.5) and (6.2), respectively. To determine ε_ω we solved the inner problem (6.3) numerically to obtain $\omega(a)$. In addition, we have defined $\text{err}_{\text{asy}} \equiv \bar{u}_{F_\sigma}/\bar{u}_{\Gamma_\varepsilon,\text{asy}} - 1$ and $\text{err}_\omega \equiv \bar{u}_{F_\sigma}/\bar{u}_{\Gamma_\varepsilon,\omega} - 1$. As expected, we observe that err_ω is always very small, whereas err_{asy} is the largest when the spheres are nearly touching, for which a is not large (last row for each σ).

We now repeat this computation replacing the small spheres by flat disks as shown in Fig. 9a (right). In this case $C = 2/\pi$ so that from (6.5) we now have $\varepsilon_{\text{asy}} = \frac{4}{N}\exp\left(-\frac{\pi}{2N\sigma} - \gamma_e\right)$. Unlike for the case of small spheres, the disks never touch, so that N can be taken arbitrarily large. A favorable comparison between the asymptotic and numerical results are shown in Table 6.

N	a	$\varepsilon_{\rm asy}$	ε_ω	$\bar{u}_{F_\sigma,\,\rm num}$	$\bar{u}_{\Gamma_\varepsilon,\rm asy}$	$\bar{u}_{\Gamma_\varepsilon}(\varepsilon_\omega)$	$\rm err_{asy}$	$\rm err_\omega$
$\sigma = 0.2$								
1	5.000	8.718×10^{-4}	8.788×10^{-4}	3.16545	3.14745	3.14350	+0.57%	+0.70%
2	2.500	0.02212	0.02281	1.52867	1.53152	1.51635	−0.19%	+0.81%
4	1.250	0.07881	0.08776	0.85510	0.90407	0.85196	−5.42%	+0.37%
8	0.625	0.1052	0.1438	0.60892	0.76503	0.61763	−20.41%	−1.41%
$\sigma = 0.1$								
1	10.000	3.385×10^{-7}	3.391×10^{-7}	7.08459	7.07444	7.07344	+0.14%	+0.16%
2	5.000	4.359×10^{-4}	4.394×10^{-4}	3.49342	3.49403	3.49007	−0.02%	+0.10%
4	2.500	0.01106	0.01140	1.86521	1.87739	1.86218	−0.65%	+0.16%
8	1.250	0.03941	0.04388	1.19152	1.24464	1.19139	−4.27%	+0.01%
16	0.625	0.05259	0.07191	0.94474	1.10206	0.94863	−14.27%	−0.41%
$\sigma = 0.05$								
1	20.000	5.101×10^{-14}	5.103×10^{-14}	14.93663	14.92842	14.92817	+0.05%	+0.06%
2	10.000	1.692×10^{-7}	1.696×10^{-7}	7.42086	7.42102	7.42002	+0.00%	+0.01%
4	5.000	2.180×10^{-4}	2.197×10^{-4}	3.83748	3.84060	3.83665	−0.08%	+0.02%
8	2.500	0.005531	0.005702	2.20928	2.22376	2.20853	−0.65%	+0.03%
16	1.250	0.01970	0.02194	1.53555	1.58931	1.53568	−3.38%	−0.01%
32	0.625	0.02629	0.03596	1.28862	1.44555	1.29003	−10.86%	−0.11%

Table 6: MFRT results when $D = 1$ for the straight filament in the cylinder ($L = 2$) versus that for the fragmented filament with N flat disks of radius σ perpendicular to its axis of symmetry.

From Table 6, we observe, as expected, that $\rm err_{asy}$ is the largest for tightly packed disks where a is not large and where the ratio $\varepsilon_\omega/\varepsilon_{\rm asy}$ is the largest. Unlike for small spheres, the flat disks can be taken arbitrary close, which is when that ratio grows the most, and the effect is more pronounced than for spheres (e.g. $\rm err_{asy} = 20\%$ for $N = 8, \sigma = 0.2$). In contrast, $\rm err_\omega$, in which $\omega(a)$ must be computed numerically from the new inner problem (6.3), always closely agrees with the full numerics.

Ring of Small Spheres. Next, we consider an equatorial filament of radius $r_0 = 0.6$ centered on the $z = 0$ plane in the unit sphere and we fragment it into N small spheres of radius $\sigma = 0.1$ as shown in Fig. 9b. To test our asymptotic theory, we take $D = 1$, $r_0 = 0.6$ and $\sigma = 0.1$. For each N we use ε from the large-a asymptotics (6.5), and estimate $\bar{u}_{\Gamma_\varepsilon}$ both from the thin-filament asymptotics (3.9) (with $d_c = 1$) and from the numerical solution of (6.1), which we label by $\bar{u}_{\Gamma_\varepsilon,\rm asy}$ and $\bar{u}_{\Gamma_\varepsilon,\rm num}$, respectively. In Table 7 we compare these results with the corresponding full numerical results $\bar{u}_{F_\sigma,\rm num}$ for the fragmented filament computed using the methodology in Appendix F.2. In this Table, $\omega_{\rm asy}$ is given by (6.4) while $\omega(a)$ is computed from the new inner problem (6.3) numerically using Appendix F.2.

N	a	$\omega_{\rm asy}$	$\omega(a)$	$\varepsilon_{\rm asy}$	$\bar{u}_{\Gamma_\varepsilon,\,\rm asy}$	$\bar{u}_{\Gamma_\varepsilon,\,\rm num}$	$\bar{u}_{F_\sigma,\,\rm num}$	$\frac{\bar{u}_{\Gamma_\varepsilon,\,\rm num}}{\bar{u}_{\Gamma_\varepsilon,\,\rm asy}} - 1$	$\frac{\bar{u}_{F_\sigma,\,\rm num}}{\bar{u}_{\Gamma_\varepsilon,\,\rm asy}} - 1$	$\frac{\bar{u}_{F_\sigma,\,\rm num}}{\bar{u}_{\Gamma_\varepsilon,\,\rm num}} - 1$
5	3.770	1.6338	1.6337	0.01952	0.51077	0.51115	0.51697	+0.07%	+1.21%	+1.14%
10	1.885	0.4420	0.4382	0.06428	0.30001	0.30430	0.30538	+1.43%	+1.79%	+0.36%
15	1.257	0.2191	0.1932	0.08032	0.26060	0.26712	0.26288	+2.50%	+0.87%	−1.59%
16	1.178	0.2051	0.1708	0.08146	0.25813	0.26481	0.25911	+2.59%	+0.38%	−2.15%
17	1.109	0.1964	0.1524	0.08216	0.25659	0.26338	0.25604	+2.65%	−0.21%	−2.79%
18	1.047	0.1920	0.1369	0.08253	0.25581	0.26265	0.25352	+2.68%	−0.89%	−3.48%

Table 7: MFRT results when $D = 1$ for the fragmentation of an equatorial filament of radius $r_0 = 0.6$ into N small spheres of radius $\sigma = 0.1$.

From Table 7 we observe that the largest error of about 3.5% occurs when $a = 1.047$, when the spheres almost touch each other and the large-a asymptotics (6.5) no longer applies. We remark that upon replacing ε_{asy} by $\varepsilon_{\omega(a)}$ in this case reduces the error to only -0.05%. We have also verified that $\bar{u}_{F_\sigma,\text{num}}$ can be in good agreement with the asymptotic approximation $\bar{u}_{F_\sigma,\text{asy}}$ obtained by using the Green's function for the sphere (see (3.20) of Proposition 6). For example, with $N = 15$ spheres, $\bar{u}_{F_\sigma,\text{asy}} = 0.26050$, which is less than a 1% deviation from $\bar{u}_{F_\sigma,\ \text{num}}$.

Fragmented trefoil. As a more challenging non-symmetric test of our main result in Proposition 9, we fragment the Trefoil knot, with centerline defined by (4.18a) with $p = 3$, $q = 2$, $r_0 = 0.6$ and $\rho_0 = 0.25$ as shown in Fig. 9c (left). The filament centerline, of length $L = 8.974$, is fragmented into N equally-spaced small spheres of radius $\sigma = 0.1$, with the center of the first sphere at $t = 0$. When $D = 1$, we tabulate our results for the global MFRT at several values of N in Table 8, following the notation of Table 7. In this Table, $\bar{u}_{\Gamma_\varepsilon,\text{asy}}$ is computed from the numerical solution of the integral equation (2.19).

N	a	ω_{asy}	$\omega(a)$	ε_{asy}	$\bar{u}_{\Gamma_\varepsilon,\,\text{asy}}$	$\bar{u}_{\Gamma_\varepsilon,\,\text{num}}$	$\bar{u}_{F_\sigma,\,\text{num}}$	$\frac{\bar{u}_{\Gamma_\varepsilon,\,\text{num}}}{\bar{u}_{\Gamma_\varepsilon,\,\text{asy}}} - 1$	$\frac{\bar{u}_{F_\sigma,\,\text{num}}}{\bar{u}_{\Gamma_\varepsilon,\,\text{asy}}} - 1$	$\frac{\bar{u}_{F_\sigma,\,\text{num}}}{\bar{u}_{\Gamma_\varepsilon,\,\text{num}}} - 1$
8	5.609	3.0753	3.0753	0.004617	0.32252	0.32255	0.34297	+0.01%	+6.34%	+6.33%
16	2.804	0.9641	0.9636	0.03813	0.16472	0.16610	0.17049	+0.84%	+3.50%	+2.64%
32	1.402	0.2551	0.2394	0.07749	0.11121	0.11592	0.11493	+4.24%	+3.35%	−0.85%
39	1.151	0.2012	0.1633	0.08177	0.10711	0.11227	0.10946	+4.82%	+2.20%	−2.50%
40	1.122	0.1978	0.1557	0.08205	0.10684	0.11203	0.10894	+4.86%	+1.96%	−2.76%
41	1.094	0.1951	0.1487	0.08227	0.10664	0.11185	0.10847	+4.89%	+1.71%	−3.03%
42	1.068	0.1932	0.1421	0.08244	0.10649	0.11172	0.10803	+4.91%	+1.45%	−3.30%

Table 8: MFRT results when $D = 1$ for the fragmentation of the Trefoil filament (4.18a) *with $p = 3$, $q = 2$, $r_0 = 0.6$, and $\rho_0 = 0.25$ into N small spheres of radius $\sigma = 0.1$.*

In Table 8 we observe a close agreement between the equivalent full filament results (both asymptotics and numerics), and the fragmented filament, even with relatively few spheres ($N = 8$). The error begins to grow for small trap separation. For $N = 42$ spheres, $a = 1.068$, and the asymptotic value $\omega \sim a - \log(4a) + \gamma_e = 0.1932$ deviates significantly from an exact value $\omega\,(1.068) = 0.1421$ computed from a numerical solution of the new inner problem (6.3). The latter value for ω changes the equivalent filament cross-sectional radius to $\varepsilon = 0.08675$, and the error between the full computations drops from 3.30% to only 0.25%.

Note on numerics. We initially used the built-in MATLAB FEM solver, with the interface to it written by Claude AI (Opus version 5.5) for numerical work in this section. These numerics were then independently cross-validated by Claude's own numerical solvers that it custom-built for each of the problems, and for which it wrote its own 3D numerics without using MATLAB's FEM solver. Claude's own solver was able to achieve a better convergence and accuracy than the standard MATLAB FEM solver running on a 16gig laptop; Tables 5 to 8 therefore show the more precise values achieved by Claude's own routines. We verified that both methods (MATLAB FEM vs. Claude) agreed to within reported accuracy of MATLAB's FEM computation. For example, for the $N = 40$ trefoil fully 3D numerical computation, Claude was able to compute up to 4 significant digits using its own 3D code (included in Table 8), while the MATLAB FEM package only managed up to 2 significant digits before running out of memory.

7 Discussion

We have introduced a new asymptotic analysis for the mean first-reaction time to thin filaments with reactive boundaries. Each filament is assumed to have a centerline that is a simple closed curve, and the collection of filaments are assumed to be non-intersecting (with themselves and with each other). Our asymptotic analysis reduces the full 3-D problem to one of determining the line densities on each filament and the global MFRT in terms of the solution to a coupled set of 1-D integral equations. Our theory applies to filaments of general cross-sectional shape with the geometry being encoded in the logarithmic reactive capacitance, which can be computed numerically from a Steklov eigenfunction representation. For various configurations of filaments, we validated our asymptotic results using a simple trapezoidal approximation of the integral operator. Our results confirm the expected accuracy of our asymptotic theory as the cross-sectional radius decreases when compared to full finite element simulations. Extensions of the theory to account for heterogeneous diffusivity, the splitting probabilities and to determine the principal eigenvalue of the Laplacian were discussed. Finally, the relationship between the MFRT for filaments and for the related problem of replacing the filament by spatially localized targets equally-spaced on its centerline was analyzed.

We remark that in our initial formulation of the MFPT problem, we have included the scaling factor ε to the Robin condition (1.2) to keep the constant reactivity parameter b in the inner solution. Dividing by ε, one recovers the conventional form of the Robin condition, $D\partial_n u + \mathcal{K}u = 0$, with the dimensional reactivity $\mathcal{K}_b \equiv bD/\varepsilon$ that increases as $\varepsilon \to 0$. In many applications, however, $\mathcal{K}_b$ remains fixed and does not scale with ε. In this case, $b = \varepsilon\mathcal{K}_b/D$ vanishes in the limit $\varepsilon \to 0$ that significantly changes the asymptotic behavior of the MFRT. For instance, in the case of a single filament, substitution of the Taylor expansion (A.7) into (1.5) yields

$$\bar{u} \sim \frac{|\Omega|}{\mathcal{K}_b|\partial\Gamma_\varepsilon|} + \frac{|\Omega|}{D|\Gamma|}\left(\frac{\log(1/\varepsilon)}{|\partial\mathcal{B}|} + \frac{C_1}{2\pi} + \frac{1}{|\Gamma|}\int_\Gamma\int_\Gamma R\left(\mathbf{X}(s);\mathbf{X}(s')\right)\,\mathrm{d}s\,\mathrm{d}s' + \frac{1}{4\pi|\Gamma|}\int_\Gamma \mathcal{E}(s)\,\mathrm{d}s + \mathcal{O}\left(\frac{\varepsilon}{\log(\varepsilon)}\right)\right). \tag{7.1}$$

The first term, which gives the leading-order contribution $1/\varepsilon$, corresponds to the standard kinetics-limited regime; expectedly, the MFRT is inversely proportional to the surface area $|\partial\Gamma_\varepsilon|$ of the reactive boundary and to the reactivity $\mathcal{K}_b$, whereas it does not depend on the diffusion coefficient D. In turn, the logarithmic term gives the subleading contribution. The qualitative change in the scaling of the MFRT, from $\log(1/\varepsilon)$ to $1/\varepsilon$, was discussed previously for circular targets in [29] (see also [30]). The logarithmic reactive capacitance $d_c(b)$ encompasses various scenarios (when b is fixed, vanishing, or infinite) and quantitatively describes transitions between them in (1.5) and related expressions.

There are many avenues for future study which arise from this work. We have demonstrated our theory on closed filaments for which the trapezoidal rule provides accurate quadrature. However, typical biological filaments and fibers are either open at both ends or tethered at one end to the boundary and free at the other. We hypothesize that the results contained in the log-summed integral equation system still hold to leading order. However, the effects of open ends will arise in higher-order corrections through an additional inner problem centered at each tip, which needs to be analyzed. Additional high-order effects will arise at $\mathcal{O}(\varepsilon)$ due to the centerline curvature as seen from the inner problem (2.2). Related rigorous work on finite-end filament conditions in slender-body theory has recently been considered in [50]. The details of obtaining these higher-order corrections is left to future work, as well as generalizations to include drift fields

and directed transport inside the filaments, among others.

Acknowledgments MJW and TK are grateful for the support of the NSERC Discovery Grant Program (Canada). AEL acknowledges support from NSF grant DMS-2052636. This research was supported in part by grants from the NSF (DMS-2235451) and Simons Foundation (MPS-NITMB-00005320) to the NSF-Simons National Institute for Theory and Mathematics in Biology (NITMB). D.S.G. acknowledges the Simons Foundation for supporting his sabbatical sojourn in 2024 at the CRM, University of Montréal, Canada, as well as the Alexander von Humboldt Foundation for support within a Bessel Prize award. We gratefully acknowledge the support of the University of Notre Dame's Kylemore Abbey Global Centre.

Appendix A The inner problem

We first derive (2.1) in terms of the tubular coordinates. The position vector of a point $\mathbf{x}$ in the tubular neighbourhood is written as $\mathbf{x}(s,\eta_1,\eta_2) = \mathbf{X}(s) + \eta_1\mathbf{M}_1(s) + \eta_2\mathbf{M}_2(s)$. Upon taking partial derivatives and using $\mathbf{M}_1'(s) = -\kappa_1(s)\mathbf{T}(s)$ and $\mathbf{M}_2'(s) = -\kappa_2(s)\mathbf{T}(s)$, where $\mathbf{T}(s)$ is the unit tangent and $\kappa_1(s)$ and $\kappa_2(s)$ are curvatures along each respective normal direction, we get $\mathbf{x}_s = (1-\kappa_1\eta_1-\kappa_2\eta_2)\,\mathbf{T}(s)$, $\mathbf{x}_{\eta_1} = \mathbf{M}_1(s)$, and $\mathbf{x}_{\eta_2} = \mathbf{M}_2(s)$. In this way, we obtain the scale factors for the transformation as

$$h_s = |\mathbf{x}_s| = 1-\kappa_1\eta_1-\kappa_2\eta_2\,, \quad h_{\eta_1} = |\mathbf{x}_{\eta_1}| = 1\,, \quad h_{\eta_2} = |\mathbf{x}_{\eta_2}| = 1\,.$$

A sufficient condition to ensure that $h_s > 0$ along the filament is that $\kappa_1\eta_1+\kappa_2\eta_2 < 1$ for $0 \le s \le L$. By using the Cauchy-Schwartz inequality, a sufficient condition for this inequality to hold is that $\sqrt{\eta_1^2+\eta_2^2} < 1/\kappa(s)$ for $0 \le s \le L$, where $\kappa(s) \equiv \sqrt{\kappa_1^2+\kappa_2^2} = |\mathbf{X}''(s)|$ is the curvature of the filament centerline.

By using the general expression for the Laplacian of an arbitrary function Φ in an orthogonal coordinate system, in which we set $h_{\eta_1} = h_{\eta_2} = 1$, we get

$$\Delta_{\mathbf{x}}\Phi = \frac{1}{h_s}\left[\partial_s\left(\frac{1}{h_s}\partial_s\Phi\right) + \partial_{\eta_2}\left(h_s\partial_{\eta_2}\Phi\right) + \partial_{\eta_1}\left(h_s\partial_{\eta_1}\Phi\right)\right],$$

which readily yields (2.1).

A.1 The logarithmic reactive capacitance

The logarithmic reactive capacitance $d_c(b)$ is defined by the far-field behavior of the solution v_c of the boundary value problem (2.3). When the cross-section $\mathcal{B}$ is the unit disk, this problem admits an explicit solution, $v_c = \log|\mathbf{y}| + 1/b$, from which $\log[d_c(b)] = -1/b$. For other domains, the function $d_c(b)$ can be determined in terms of eigenfunctions of the exterior Steklov problem. In this Appendix, we briefly describe this spectral representation by generalizing the approach from [11, 26, 27, 30].

For a given bounded set $\mathcal{B} \subset \mathbb{R}^2$ with a connected Lipschitz boundary $\partial\mathcal{B}$, we search for eigenvalues μ_k and eigenfunctions $\Psi_k(\mathbf{y})$ of the exterior Steklov problem

$$\Delta_{\mathbf{y}}\Psi_k = 0\,; \quad \mathbf{y} \in \mathbb{R}^2 \setminus \mathcal{B}\,; \qquad \partial_n\Psi_k = \mu_k\Psi_k\,, \quad \mathbf{y} \in \partial\mathcal{B}\,; \qquad \Psi_k = \mathcal{O}(1) \quad \text{as} \quad |\mathbf{y}| \to \infty\,. \tag{A.1}$$

This eigenvalue problem has a discrete spectrum [10], i.e, a countable set of eigenvalues μ_k which can be enumerated by the index $k = 0, 1, \ldots$ in an increasing order, $0 = \mu_0 < \mu_1 \le \mu_2 \ldots \nearrow +\infty$. In turn, the

traces of eigenfunctions Ψ_k on $\partial\mathcal{B}$, $(\Psi_k)|_{\partial\mathcal{B}}$, form a complete orthonormal basis in the space $L^2(\partial\mathcal{B})$. Since $v = v_c - v_{c,b=\infty}$ is a harmonic function bounded at infinity, one can expand it over the Steklov eigenfunctions

$$v_c(\mathbf{y}) = v_{c,b=\infty}(\mathbf{y}) + \sum_{k=0}^{\infty} c_k \Psi_k(\mathbf{y})\,, \tag{A.2}$$

where the unknown coefficients c_k are obtained from the boundary condition as

$$0 = \partial_n v_c + b v_c = \partial_n v_{c,b=\infty} + \sum_{k=0}^{\infty} c_k(\mu_k + b)\Psi_k(\mathbf{y})\,, \quad \mathbf{y} \in \partial\mathcal{B}\,. \tag{A.3}$$

Multiplying this relation by Ψ_j and integrating over $\partial\mathcal{B}$, we get from the orthonormality of $\{(\Psi_k)|_{\partial\mathcal{B}}\}$ that

$$c_j = -\frac{1}{\mu_j + b}\big(\partial_n v_{c,b=\infty}\,, \Psi_j\big)_{L^2(\partial\mathcal{B})}\,. \tag{A.4}$$

Upon applying Green's second identity to the problems for Ψ_k and $v_{c,b=\infty}$, we can represent the scalar product in the numerator of (A.4) as $-2\pi\Psi_j(\infty)$ so that

$$c_j = \frac{2\pi\Psi_j(\infty)}{\mu_j + b}\,. \tag{A.5}$$

Since Ψ_k is harmonic and bounded at infinity, its gradient decays as $\mathcal{O}\left(1/|\mathbf{y}|^2\right)$, which ensures the applicability of the Green's second identity as $\lim_{R\to\infty} R\log(R)\partial_R\Psi_k = 0$, with $R = |\mathbf{y}|$.

The logarithmic reactive capacitance is obtained by evaluating the limiting behavior of (A.2) as $\mathbf{y} \to \infty$:

$$-\log[d_c(b)] = -\log[d_c(\infty)] + \sum_{k=0}^{\infty} c_k \Psi_k(\infty)\,,$$

from which

$$-\log[d_c(b)] = -\log[d_c(\infty)] + 2\pi\sum_{k=0}^{\infty}\frac{\Psi_k^2(\infty)}{\mu_k + b}\,. \tag{A.6}$$

The spectral expansion (A.6) is the main result of this Appendix. For instance, when $\mathcal{B}$ is the unit disk, all $\Psi_k(\mathbf{y})$ decay at infinity, except for $\Psi_0(\mathbf{y}) = 1/\sqrt{2\pi}$ so that the above sum has the single term $k = 0$. Since $d_c(\infty) = 1$ and $\mu_0 = 0$, we retrieve the result $\log[d_c(b)] = -1/b$. For a general cross-section $\mathcal{B}$, the eigenvalues μ_k and the coefficients $\Psi_k^2(\infty)$ can be found numerically (see, e.g., [11, 27]). In practice, the computation of a limited number of eigenmodes can be sufficient for an accurate computation of $d_c(b)$. The exterior Steklov problem also admits a natural extension to the degenerate case in which $\mathcal{B}$ is an interval (see below), allowing one to describe the limiting case of highly anisotropic filament cross-sections.

The expansion (A.6) provides the functional dependence of $d_c(b)$ on the reactivity b. In particular, we conclude that $-\log[d_c(b)]$ is a monotonically decreasing function of b: it decreases from $+\infty$ at $b = 0$ up to $-\log[d_c(\infty)]$ at $b = \infty$. The small-b asymptotic behavior of $d_c(b)$ can be obtained by a Taylor expansion as

$$-\log[d_c(b)] = \frac{C_0}{b} + \sum_{n=0}^{\infty} C_{n+1}(-b)^n\,, \tag{A.7}$$

where we use $\Psi_0 = |\partial\mathcal{B}|^{-1/2}$ and $\mu_0 = 0$ to get

$$C_0 = \frac{2\pi}{|\partial\mathcal{B}|}\,, \qquad C_1 = -\log[d_c(\infty)] + 2\pi\sum_{k=1}^{\infty}\frac{\Psi_k^2(\infty)}{\mu_k}\,, \qquad C_n = 2\pi\sum_{k=1}^{\infty}\frac{\Psi_k^2(\infty)}{\mu_k^n} \quad (n = 2, 3, \ldots)\,. \tag{A.8}$$

We now derive alternative representations of the spectral sums that define C_1 and C_2. To do so, we first introduce a new function w_b defined by $w_b = v_c - 2\pi/(b|\partial\mathcal{B}|)$, which satisfies

$$\Delta_{\mathbf{y}} w_b = 0\,, \quad \mathbf{y} \in \mathbb{R}^2 \setminus \mathcal{B}\,; \qquad \partial_n w_b + b w_b = -\frac{2\pi}{|\partial\mathcal{B}|}\,, \quad \mathbf{y} \in \partial\mathcal{B}\,, \tag{A.9}$$

with $w_b(\mathbf{y}) = \log|\mathbf{y}| - \log[d_c(b)] - \frac{2\pi}{b|\partial\mathcal{B}|} + o(1)$ as $|\mathbf{y}| \to \infty$. Upon applying the divergence theorem to (A.9), we find that $\int_{\partial\mathcal{B}} w_b \,\mathrm{d}s = 0$ holds $\forall\ b > 0$.

In the limit $b \to 0$, we expand w_b as

$$w_b = w + b w_2 + \mathcal{O}(b^2)\,. \tag{A.10}$$

Upon substituting (A.10) into both (A.9) and the condition $\int_{\partial\mathcal{B}} w_b \,\mathrm{d}s = 0$, and recalling the expansion of $-\log[d_c(b)]$ in (A.7), we collect powers of b to obtain the following problems for w and w_2:

$$\Delta_{\mathbf{y}} w = 0\,, \quad \mathbf{y} \in \mathbb{R}^2 \setminus \mathcal{B}\,; \qquad \partial_n w = -\frac{2\pi}{|\partial\mathcal{B}|}\,, \quad \mathbf{y} \in \partial\mathcal{B}\,; \qquad \int_{\partial\mathcal{B}} w \,\mathrm{d}s = 0\,, \tag{A.11}$$

and

$$\Delta_{\mathbf{y}} w_2 = 0\,, \quad \mathbf{y} \in \mathbb{R}^2 \setminus \mathcal{B}\,; \qquad \partial_n w_2 = -w\,, \quad \mathbf{y} \in \partial\mathcal{B}\,; \qquad \int_{\partial\mathcal{B}} w_2 \,\mathrm{d}s = 0\,. \tag{A.12}$$

The two constants C_1 and C_2 are calculated from the limiting behaviors:

$$C_1 = \lim_{|\mathbf{y}|\to\infty} \left(w - \log|\mathbf{y}|\right)\,, \qquad C_2 = -\lim_{|\mathbf{y}|\to\infty} w_2\,. \tag{A.13}$$

Upon using Green's second identity between w and w_2, we readily find

$$C_2 = -w_2(\infty) = \frac{1}{2\pi}\int_{\partial\mathcal{B}} w^2 \,\mathrm{d}s\,. \tag{A.14}$$

We remark that C_2 can also be obtained from the Steklov expansion, since from (A.2) we have that

$$w|_{\partial\mathcal{B}} = 2\pi \sum_{k=1}^{\infty} \frac{\Psi_k(\infty)\Psi_k(\mathbf{y})}{\mu_k}\,, \tag{A.15}$$

from which we conclude upon squaring and using orthonormality that

$$C_2 = 2\pi \sum_{k=1}^{\infty} \frac{\Psi_k^2(\infty)}{\mu_k^2} = \frac{1}{2\pi}\int_{\partial\mathcal{B}} w^2 \,\mathrm{d}s\,. \tag{A.16}$$

To determine C_1 and C_2, the key step is to solve (A.11) by using conformal maps after identifying $\mathbb{R}^2 \setminus \mathcal{B}$ as the region $\mathbb{C} \setminus \mathcal{B}$ in the complex plane. To do so, we let $\xi = y_1 + i y_2$ be any point in $\mathbb{C} \setminus \mathcal{B}$, and $\mathcal{D} \equiv \{z \in \mathbb{C}\,|\,|z| < 1\}$ be the unit disk. For a simply connected cross-section $\mathcal{B}$ with sufficiently regular boundary, let $\xi = f(z)$ be a conformal mapping from the exterior of the unit disk, $\mathbb{C} \setminus \mathcal{D}$, onto $\mathbb{C} \setminus \mathcal{B}$. As $|z| \to \infty$, it can be developed in a Laurent series as

$$\xi = f(z) \sim a_0 z + b_0 + b_1/z + b_2/z^2 + \dots\,, \tag{A.17}$$

so that $\log|\xi| \sim \log|z| + \log a_0 + o(1)$ as $z \to \infty$. Since the exact solution for $V_c(z) \equiv v_c(f(z))$ when $b = \infty$ is $\log|z|$, we have $v_c \sim \log|\xi| - \log(a_0)$, which identifies that $a_0 = d(\infty)$, i.e. a_0 is the simply the logarithmic capacity of $\partial\mathcal{B}$.

Moreover, setting $W(z) = w(f(z))$, we obtain in terms of the Jacobian $q(\theta) \equiv |f'(e^{i\theta})|$ of the map on $\partial\mathcal{D}$, that (A.11) transforms to the following problem for W:

$$\Delta_z W = 0\,, \quad z \in \mathbb{C} \setminus \mathcal{D}\,; \qquad \partial_r W = \frac{2\pi}{|\partial\mathcal{B}|} q(\theta)\,, \quad \text{on} \quad r = |z| = 1\,; \qquad \int_0^{2\pi} W(e^{i\theta}) q(\theta)\,\mathrm{d}\theta = 0\,. \tag{A.18}$$

In terms of this solution, we get from (A.13) together with the large z behavior of the map that

$$C_1 = -\log[d_c(\infty)] + \lim_{|z|\to\infty} \left(W(z) - \log|z|\right)\,. \tag{A.19}$$

Next, since $\int_0^{2\pi} q(\theta)\,d\theta = |\partial\mathcal{B}|$, we can represent the solution to the exterior Neumann problem (A.18) in $|z| > 1$ in terms of a constant A as

$$W(z) = \log|z| + A + \frac{2}{|\partial\mathcal{B}|} \int_0^{2\pi} q(\theta')\,\log\left|1 - \frac{e^{i\theta'}}{z}\right|\,\mathrm{d}\theta'\,. \tag{A.20}$$

On the circle $|z| = 1$ we have

$$W(e^{i\theta}) = A + \frac{2}{|\partial\mathcal{B}|} \int_0^{2\pi} q(\theta')\,\log|e^{i\theta} - e^{i\theta'}|\,\mathrm{d}\theta'\,, \tag{A.21}$$

and so the zero-integral constraint in (A.18) determines A as

$$A = -\frac{2}{|\partial\mathcal{B}|^2} \int_0^{2\pi}\int_0^{2\pi} q(\theta)\,q(\theta')\,\log|e^{i\theta} - e^{i\theta'}|\,\mathrm{d}\theta\,\mathrm{d}\theta'\,. \tag{A.22}$$

Finally, since $W(z) \sim \log|z| + A + o(1)$ as $|z| \to \infty$, we identify C_1 from (A.19) as

$$C_1 = -\log[d_c(\infty)] - \frac{2}{|\partial\mathcal{B}|^2} \int_0^{2\pi}\int_0^{2\pi} q(\theta)\,q(\theta')\,\log|e^{i\theta} - e^{i\theta'}|\,\mathrm{d}\theta\,\mathrm{d}\theta'\,. \tag{A.23}$$

Upon using the inverse conformal map f^{-1}, we can write C_1 in an alternative form as

$$C_1 = -\log[d_c(\infty)] - \frac{2}{|\partial\mathcal{B}|^2} \int_{\partial\mathcal{B}}\int_{\partial\mathcal{B}} \log\left|f^{-1}(\mathbf{y}_1) - f^{-1}(\mathbf{y}_2)\right|\,\mathrm{d}\mathbf{y}_1\,\mathrm{d}\mathbf{y}_2\,. \tag{A.24}$$

Next, by using the identity

$$\log|e^{i\theta} - e^{i\theta'}| = -\sum_{n=1}^{\infty} \frac{\cos(n(\theta-\theta'))}{n} = -\sum_{n=1}^{\infty} \frac{\cos(n\theta)\cos(n\theta') + \sin(n\theta)\sin(n\theta')}{n}\,, \tag{A.25}$$

as readily derived from the Taylor expansion of the principal branch of $\log(1-z)$, we can obtain a further expression for C_1. If $q(\theta)$ is even, as in the examples considered below, the sine contributions vanish so that

$$C_1 = -\log[d_c(\infty)] + \frac{2\pi^2}{|\partial\mathcal{B}|^2} \sum_{n=1}^{\infty} \frac{q_n^2}{n}\,, \qquad \text{where} \qquad q_n \equiv \frac{1}{\pi}\int_0^{2\pi} q(\theta)\cos(n\theta)\,\mathrm{d}\theta\,. \tag{A.26}$$

Similarly, we can rewrite (A.16) by using the conformal map as

$$C_2 = \frac{1}{2\pi} \int_0^{2\pi} q(\theta)\,[W(e^{i\theta})]^2\,\mathrm{d}\theta\,, \tag{A.27}$$

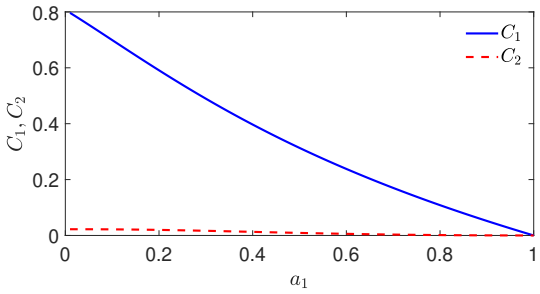


Figure 10: The coefficients C_1 and C_2 as a function of a_1 for the exterior of an ellipse with semi-axes a_1 and $a_2 = 1$.

where $W(e^{i\theta})$ is given in (A.21). Under the same symmetry assumption on $q(\theta)$, C_2 can be expressed in terms of the Fourier cosine coefficients as

$$C_2 = \frac{\pi^2}{|\partial\mathcal{B}|^2} \sum_{m=1}^{\infty} \sum_{n=1}^{\infty} \frac{q_m q_n}{mn} (q_{m+n} + q_{|m-n|}) - \frac{2\pi^3}{|\partial\mathcal{B}|^3} \left(\sum_{n=1}^{\infty} \frac{q_n^2}{n} \right)^2 . \tag{A.28}$$

As an example, let $\mathcal{B}$ be the interval $\mathcal{B} = (-1, 1)$. The Joukowski function $f(z) = \frac{1}{2}(z + 1/z)$ maps $\mathbb{C} \setminus \mathcal{D}$ onto $\mathbb{C} \setminus (-1, 1)$. As a consequence, we have $q(\theta) = |f'(e^{i\theta})| = \frac{1}{2}|1 - e^{-2i\theta}| = |\sin\theta|$, so that with $d_c(\infty) = 1/2$ we obtain from (A.23) that

$$C_1 = -\log(1/2) - \frac{2}{4^2} \int_0^{2\pi} \int_0^{2\pi} |\sin(\theta)|\,|\sin(\theta')|\,\log|e^{i\theta} - e^{i\theta'}|\,\mathrm{d}\theta\,\mathrm{d}\theta' = \frac{3}{2} - \log 2\,, \tag{A.29}$$

in agreement with the result (3.9) in [30] (note that here we used $|\partial\mathcal{B}| = 4$ because two "sides" of the interval do contribute). A brute-force computation of the integral (A.27) yields $C_2 = (21 - 2\pi^2)/(18\pi) \approx 0.0223$, as derived in [30].

For an ellipse with semi-axes a_1 and a_2 (with $a_1 \le a_2$), we have $d_c(\infty) = (a_1 + a_2)/2$. The conformal map is $f(z) = a(z + \beta/z)$, where $a \equiv (a_1 + a_2)/2$ and $\beta \equiv (a_2 - a_1)/(a_2 + a_1)$. Therefore, we get $f(e^{i\theta}) = a_2 \cos\theta + i a_1 \sin\theta$, from which $q(\theta) = \sqrt{a_2^2 \sin^2\theta + a_1^2 \cos^2\theta}$. The perimeter is $|\partial\mathcal{B}| = 4a_2 E(e)$, with $e = \sqrt{1 - (a_1/a_2)^2}$, where $E(e)$ denotes the complete elliptic integral of the second kind. These expressions fully determine C_1, either in terms of the double integral in (A.23), or in terms of (A.26). Numerical results for C_1 and C_2 for an ellipse are shown in Fig. 10.

Appendix B Intrinsic self-energy of a simple closed curve

Let Γ be a simple closed curve in $\mathbb{R}^3$ parameterized by $\mathbf{X}(s')$ where s' is arclength along Γ. For an arbitrary target point $\mathbf{X}(s) \in \Gamma$, let $\mathbf{X}_\eta(s)$ denote any point at a distance $\eta > 0$ from $\mathbf{X}(s)$ where without loss of generality we assume that s is not an endpoint, i.e. that $0 < s < L$. In this appendix we show that the intrinsic self-energy of a curve, defined by the limiting process

$$\mathcal{E}(s) \equiv \lim_{\eta \to 0^+} \left(\int_\Gamma \frac{\mathrm{d}s'}{|\mathbf{X}_\eta(s) - \mathbf{X}(s')|} + 2\log\eta \right) , \tag{B.1}$$

has a finite value. For the special case where Γ is a circular ring of radius r, we will calculate $\mathcal{E}(s)$ analytically. Moreover, we will provide a numerical approach to compute $\mathcal{E}(s)$ for arbitrary simple closed curves.

We first show that the integral I defined by

$$I \equiv \int_\Gamma \frac{\mathrm{d}s'}{|\mathbf{X}_\eta(s) - \mathbf{X}(s')|}\,, \tag{B.2}$$

has a logarithmic singularity as $\eta \to 0^+$. In a neighbourhood of the target point $\mathbf{X}(s) \in \Gamma$, we let $s' = s + \sigma$ where $\sigma \ll 1$. Since Γ is smooth and s' is arclength on Γ we have $\mathbf{X}(s') = \mathbf{X}(s) + \sigma \mathbf{X}'(s) + \mathcal{O}(\sigma^2)$ as $\sigma \to 0$, where $|\mathbf{X}'(s)| = 1$. As a result, by Pythagoras we conclude that $|\mathbf{X}_\eta(s) - \mathbf{X}(s')| \approx \sqrt{\sigma^2 + \eta^2}$ for $|\sigma| = |s' - s| \ll 1$ and $\eta \ll 1$. Next, we decompose I into a local integral and a global part as

$$I \approx \underbrace{\int_{s-\sigma}^{s+\sigma} \frac{\mathrm{d}s'}{\sqrt{\eta^2 + (s'-s)^2}}}_{\text{local part}} + \int_0^{s-\sigma} \frac{\mathrm{d}s'}{|\mathbf{X}_\eta(s) - \mathbf{X}(s')|} + \int_{s+\sigma}^{L} \frac{\mathrm{d}s'}{|\mathbf{X}_\eta(s) - \mathbf{X}(s')|}\,. \tag{B.3}$$

The local integral in (B.3) is calculated exactly as

$$I_{loc} \equiv \int_{-\sigma}^{\sigma} \frac{\mathrm{d}\xi}{\sqrt{\eta^2 + \xi^2}} = -2\log\eta + 2\log\left[\sigma + \sqrt{\sigma^2 + \eta^2}\right]\,. \tag{B.4}$$

Finally, with the ordering $\eta \ll \sigma \ll 1$, we let $\eta \to 0^+$ to obtain that $I_{loc} \sim -2\log\eta$ as $\eta \to 0$. We conclude that the leading-order singular behavior of I is universal and independent of the shape of Γ. The remaining η-independent constant, augmented by the contribution of Γ to I away from the target point $\mathbf{X}(s)$ is precisely the finite part in (B.1) that defines the intrinsic self-energy $\mathcal{E}(s)$ of Γ.

B.1 Intrinsic self-energy of a ring

We now compute $\mathcal{E}(s)$ when Γ is a circular ring of radius r parameterized as

$$\mathbf{X}(s') = r\left(\cos\left(s'/r\right), \sin\left(s'/r\right), 0\right)^T\,, \quad 0 \le s' \le 2\pi r\,. \tag{B.5}$$

By symmetry it follows that $\mathcal{E}(s) = \mathcal{E}_0$, independent of the target point s on the ring. Therefore, without loss of generality we can take $\mathbf{X}_\eta(s) = (r + \eta, 0, 0)^T$ in (B.1), and for this point we calculate that

$$|\mathbf{X}_\eta(s) - \mathbf{X}(s')|^2 = \left(r + \eta - r\cos\left(s'/r\right)\right)^2 + r^2\sin^2\left(s'/r\right) = \eta^2 + 4r(r+\eta)\sin^2\left(s'/(2r)\right)\,. \tag{B.6}$$

Upon introducing θ by $s' = r\theta$, we obtain from (B.6) that

$$I \equiv \int_\Gamma \frac{\mathrm{d}s'}{|\mathbf{X}_\eta(s) - \mathbf{X}(s')|} = \int_0^{2\pi} \frac{r\,\mathrm{d}\theta}{\left[\eta^2 + 4r(r+\eta)\sin^2\left(\theta/2\right)\right]^{1/2}} = 4r\int_0^{\pi/2} \frac{\mathrm{d}\phi}{\left[\eta^2 + 4r(r+\eta)\sin^2\phi\right]^{1/2}}\,. \tag{B.7}$$

By introducing $\psi = \pi/2 - \phi$ and using $\cos^2\psi = 1 - \sin^2\psi$, we identify that

$$I = \frac{4r}{2r+\eta}\int_0^{\pi/2} \frac{\mathrm{d}\psi}{\sqrt{1 - k^2\sin^2\psi}} = \frac{4r}{2r+\eta}K(k) \quad \text{where} \quad k \equiv \frac{2\sqrt{r(r+\eta)}}{2r+\eta}\,, \tag{B.8}$$

and $K(k)$ is the complete elliptic integral of the first kind. In this way, we evaluate from (B.1) the limit

$$\mathcal{E}(s) = \mathcal{E}_0 = \lim_{\eta\to 0}\left(\frac{4r}{2r+\eta}K(k) + 2\log\eta\right)\,, \tag{B.9}$$

where k is defined in (B.8).

We observe that $k \to 1^-$ as $\eta \to 0^+$. For $k \to 1^-$, we use the limiting asymptotics $K(k) \sim \log(4/k')$ with $k' \equiv \sqrt{1-k^2}$. By using (B.8) for k we obtain that $k' = \eta/(2r+\eta)$. In this way, we derive that $K(k) \sim -\log\eta + \log(8r) + o(1)$ as $\eta \to 0^+$. Therefore, from (B.9) we conclude that

$$\mathcal{E}_0 = \lim_{\eta\to 0^+} \left(2\left[-\log\eta + \log(8r) + o(1)\right] + 2\log\eta\right) = 2\log(8r)\,, \tag{B.10}$$

which is the intrinsic self-energy of a loop of radius r.

B.2 Numerical method: Arclength parameterization

Let us consider a disk of radius $\rho = L/(2\pi)$ and perimeter L equivalent to that of the filament. We will use the solution of this case to obtain an integral for $\mathcal{E}(s)$ with a removable singularity. Consider two points of arclengths s and s' for which the chord between them is of length

$$d(s-s') = 2\rho\left|\sin\left(\frac{s-s'}{2\rho}\right)\right| = \frac{L}{\pi}\left|\sin\left(\frac{\pi(s-s')}{L}\right)\right|. \tag{B.11}$$

This expression is L-periodic and even in $s-s'$ and vanishes at $s'=s$ with local behavior

$$d(s-s') = |s-s'| - \frac{\pi^2}{6L^2}|s-s'|^3 + \mathcal{O}(|s-s'|^5)\,. \tag{B.12}$$

Upon adding and subtracting the regularized kernel to (B.1) we have that

$$\mathcal{E}(s) = \underbrace{\lim_{\eta\to 0^+}\int_\Gamma \left[\frac{1}{|\mathbf{X}_\eta(s)-\mathbf{X}(s')|} - \frac{1}{\sqrt{\eta^2+[d(s-s')]^2}}\right]\mathrm{d}s'}_{\text{(I)}} + \underbrace{\lim_{\eta\to 0}\left(\int_\Gamma \frac{\mathrm{d}s'}{\sqrt{\eta^2+[d(s-s')]^2}} + 2\log\eta\right)}_{\text{(II)}}. \tag{B.13}$$

Using the local behavior (B.12) and (B.6), we observe that the first integral is de-singularized and we can pass to the limit as $\eta \to 0^+$. Hence, we obtain for the first integral that

$$\text{(I)} = \int_\Gamma \left[\frac{1}{|\mathbf{X}(s)-\mathbf{X}(s')|} - \frac{1}{d(s-s')}\right]\mathrm{d}s'\,. \tag{B.14}$$

For the second integral in (B.13), we additionally de-singularize with (B.4) to obtain

$$\int_\Gamma \frac{\mathrm{d}s'}{\sqrt{\eta^2+[d(s-s')]^2}} = \int_\Gamma \left[\frac{1}{\sqrt{\eta^2+[d(s-s')]^2}} - \frac{1}{\sqrt{\eta^2+(s-s')^2}}\right]\mathrm{d}s' + \int_{s-L/2}^{s+L/2}\frac{\mathrm{d}s'}{\sqrt{\eta^2+(s-s')^2}}\,. \tag{B.15}$$

Using the periodicity of the curve, we find that as $\eta \to 0^+$, the first integral in (B.15) tends to

$$\begin{aligned}\int_{s-L/2}^{s+L/2}\left[\frac{1}{d(s-s')} - \frac{1}{|s-s'|}\right]\mathrm{d}s' &= 2\int_s^{s+L/2}\left[\frac{\pi/L}{\sin\left(\pi(s'-s)/L\right)} - \frac{1}{s'-s}\right]\mathrm{d}s' \\ &= 2\int_0^{\pi/2}\left[\frac{1}{\sin\theta} - \frac{1}{\theta}\right]\mathrm{d}\theta = 2\Big[\log\tan\left(\frac{\theta}{2}\right) - \log\theta\Big]_0^{\pi/2} = 2\log\left(\frac{4}{\pi}\right),\end{aligned}$$

where we used the substitution $\theta = \pi(s'-s)/L$. For the second integral in (B.15), we have that

$$\int_{s-L/2}^{s+L/2}\frac{\mathrm{d}s'}{\sqrt{\eta^2+(s-s')^2}} = 2\,\mathrm{arcsinh}\left(\frac{L}{2\eta}\right) = 2\log\left(\frac{L}{\eta}\right) + \mathcal{O}\Big(\frac{\eta^2}{L^2}\Big) \quad \text{as} \quad \eta\to 0^+\,. \tag{B.16}$$

Finally, by combining equations (B.14)-(B.16) in (B.13), we obtain the final result

$$\mathcal{E}(s) = 2\log\left(\frac{4L}{\pi}\right) + \int_\Gamma \left[\frac{1}{|\mathbf{X}(s)-\mathbf{X}(s')|} - \frac{\pi/L}{\left|\sin\left(\pi(s-s')/L\right)\right|}\right] \mathrm{d}s' \,. \tag{B.17}$$

In the case where the curve is a circle of radius ρ, we have that $|\mathbf{X}(s)-\mathbf{X}(s')| = d(s-s')$ so the integral term in (B.17) vanishes and we recover $\mathcal{E}_0 = 2\log(8\rho)$ as derived in (B.10). The reduced formulation in (B.17) features an integral that is well behaved and is amenable to standard integration techniques.

Appendix C Optimization of the radius of an equatorial filament

In this appendix we prove Proposition 5 establishing that there is a unique value r_{0min} of the centerline radius r_0 that minimizes the global MFRT for a concentric equatorial filament in the unit sphere. We also approximate r_{0min} for $\varepsilon \ll 1$.

To do so, we first seek properties of the integral $J(r_0)$ in (3.7). Although it appears intractable to evaluate $J(r_0)$ in closed form, we establish in the next result that $J(r_0)$ is monotone decreasing on $0 < r_0 < 1$.

Lemma 2. *On $0 < r_0 < 1$, we have*

$$J'(r_0) = \frac{4\pi}{r_0}\left(1 - \frac{2}{\pi}K\left(r_0^2\right)\right) < 0\,, \tag{C.1}$$

since $K(r_0^2) > \pi/2$ on $0 < r_0 < 1$. Moreover, $J(0) = 2\pi\log 2 \approx 4.3552$ and $J(1) = 8G_c - 2\pi\log 2 \approx 2.9726$, where G_c is Catalan's constant.

Proof. The result for $J(0)$ is immediate. To find $J(1)$ we use $1-\cos\psi = 2\sin^2(\psi/2)$ to get

$$\begin{aligned} J(1) &= \int_0^{2\pi} \log\left[2\sin\left(\frac{\psi}{2}\right)\left(1+\sin\left(\frac{\psi}{2}\right)\right)\right] \mathrm{d}\psi\,, \\ &= 2\pi\log 2 + 2\int_0^\pi \log(\sin x)\ \mathrm{d}x + 2\int_0^\pi \log(1+\sin x)\ \mathrm{d}x\,, \\ &= 2\pi\log 2 + 2\left(-\pi\log 2\right) + 4\left(2G_c - \frac{\pi}{2}\right)\,, \\ &= 8G_c - 2\pi\log 2\,, \end{aligned}$$

where $G_c \equiv -\int_0^{\pi/4}\log[\tan(x)]\ \mathrm{d}x \approx 0.915966$ is Catalan's constant. Next, we label $g \equiv 1 - r^2\cos\psi + C$, where $C \equiv \left(r_0^4 - 2r_0^2\cos\psi + 1\right)^{1/2}$. We calculate that

$$J'(r_0) = \int_0^{2\pi} \frac{\partial_{r_0} g}{g}\ \mathrm{d}\psi \qquad \text{where} \qquad \frac{\partial_{r_0} g}{g} = \frac{2r_0}{C}\left(\frac{r_0^2 - (1+C)\cos\psi}{1 - r_0^2\cos\psi + C}\right)\,. \tag{C.2}$$

Upon multiplying top and bottom by $1 - r_0^2\cos\psi - C$, we calculate the denominator $(1-r^2\cos\psi)^2 - C^2$ to get

$$\frac{\partial_{r_0} g}{g} = -\frac{2r_0}{C}\frac{\left(r_0^2 - (1+C)\cos\psi\right)\left(1 - C - r_0^2\cos\psi\right)}{r_0^4\sin^2\psi}\,. \tag{C.3}$$

By collecting powers of C in the numerator and by using $C^2 = r_0^4 - 2r_0^2\cos\psi + 1$, we obtain after some algebra that (C.3) reduces to

$$\frac{\partial_{r_0} g}{g} = \frac{2}{r_0} - \frac{2}{r_0 C}\,. \tag{C.4}$$

Finally, by substituting (C.4) into (C.2), we evaluate $J'(r_0)$ as

$$J'(r_0) = \int_0^{2\pi} \left(\frac{2}{r_0} - \frac{2}{r_0 \left(r_0^4 - 2r_0^2 \cos\psi + 1\right)^{1/2}} \right) \mathrm{d}\psi = \frac{4\pi}{r_0} - \frac{8K(r_0^2)}{r_0}\,, \tag{C.5}$$

which completes the proof of (C.1). □

Next, we use (C.1) together with

$$\frac{d}{dr_0} K\left(r_0^2\right) = \frac{2}{r_0(1-r_0^4)} E(r_0^2) - \frac{2}{r_0} K\left(r_0^2\right)\,,$$

where $E(m) \equiv \int_0^{\pi/2} \left(1 - m^2 \sin^2\theta\right)^{1/2}\, \mathrm{d}\theta$ is the complete elliptic integral of the second kind of modulus m. In this way, we calculate from (3.9b) in terms of $a_\varepsilon \equiv 8/(\varepsilon d_c)$ that

$$\mathcal{F}_\varepsilon'(r_0) = \frac{1}{r_0}\mathcal{C}_\varepsilon(r_0) \quad \text{where} \quad \mathcal{C}_\varepsilon(r_0) \equiv \frac{1 - \log(a_\varepsilon r_0)}{r_0} + \frac{4E\left(r_0^2\right)}{1-r_0^4} + 2\pi(r_0^2 - 1)\,. \tag{C.6}$$

To show that $\mathcal{C}_\varepsilon(r_0)$ has a unique root on $\mathcal{O}\left(1/a_\varepsilon\right) \ll r_0 \ll 1 - \mathcal{O}\left(1/a_\varepsilon\right)$, we first observe that $\mathcal{C}_\varepsilon(r_0) \to -\infty$ when $r_0 \to 0$ but with $\mathcal{O}\left(1/a_\varepsilon\right) \ll r_0$ and that $\mathcal{C}_\varepsilon(r_0) \to +\infty$ when $r_0 \to 1^-$ but with $r_0 \ll 1 - \mathcal{O}\left(1/a_\varepsilon\right)$. By the intermediate value theorem there must be a root $r_{0\,\min}$ to $\mathcal{C}_\varepsilon(r_0) = 0$ on this interval. To show that this root is unique we now establish that $\mathcal{C}_\varepsilon(r_0)$ is monotone increasing. To do so, we use the identity

$$\frac{d}{dr_0} E(r_0^2) = \frac{2}{r_0}\left[E(r_0^2) - K(r_0^2)\right]\,,$$

to obtain after some algebra that

$$\mathcal{C}_\varepsilon'(r_0) = 4\pi r_0 + \frac{(\log(a_\varepsilon r_0) - 2)}{r_0^2} + \frac{8}{r_0\left(1-r_0^4\right)^2}\left[r_0^4 E(r_0^2) + E(r_0^2) - (1-r_0^4)K(r_0^2)\right]\,. \tag{C.7}$$

By using the well-known identity $E(m) - (1-m^2)K(m) > 0$ on $0 < m < 1$ it follows from (C.7) that $\mathcal{C}_\varepsilon'(r_0) > 0$ on $\mathcal{O}\left(1/a_\varepsilon\right) \ll r_0 \ll 1 - \mathcal{O}\left(1/a_\varepsilon\right)$.

This unique root to $\mathcal{F}_\varepsilon'(r_0) = 0$, given by the zero of $\mathcal{C}_\varepsilon(r_0) = 0$ and labeled by $r_{0\,\min}$, is a global minimum of $\mathcal{F}_\varepsilon(r_0)$ since from (C.6) we have

$$\mathcal{F}_\varepsilon''(r_0) = -\frac{\mathcal{C}_\varepsilon(r_0)}{r_0^2} + \frac{\mathcal{C}_\varepsilon'(r_0)}{r_0} = \frac{\mathcal{C}_\varepsilon'(r_{0\,\min})}{r_{0\,\min}} > 0 \quad \text{when} \quad r_0 = r_{0\,\min}\,.$$

Next, we approximate $r_{0\,\min}$ for $a_\varepsilon \gg 1$ by using a dominant balance argument. We readily observe from (C.1) that this root is close to the boundary and so we set $r_0 = 1 - \delta$ for some $\delta \ll 1$. By using $1 - r_0^4 \sim 4\delta - 6\delta^2$, we obtain

$$-\frac{\log a_\varepsilon}{1-\delta} + \frac{1+\delta}{1-\delta} + \frac{E\left(1 - 2\delta + \mathcal{O}(\delta^2)\right)}{\delta - 3\delta^2/2 + \mathcal{O}(\delta^3)} - 4\pi\delta + \mathcal{O}(\delta^2) = 0\,,$$

which yields that

$$-\log a_\varepsilon + 1 + \delta + \frac{(1-\delta)}{\delta\left(1 - 3\delta/2\right)} E(1-2\delta) - 4\pi\delta \approx 0\,. \tag{C.8}$$

Then by using the well-known asymptotics $E(m) \sim 1 - \frac{(1-m)}{2}\log(1-m) + (3\log 2 - 1)(1-m)/2$ as $m \to 1^-$, we obtain that

$$-\log a_\varepsilon + 1 + \frac{1}{\delta} + \log\left(\frac{4}{\delta}\right) - \frac{1}{2} + \mathcal{O}(\delta) = 0\,, \tag{C.9}$$

which has the approximate root

$$\delta \sim \frac{1}{\log a_\varepsilon} + \frac{[\log(4\log a_\varepsilon) + 1/2]}{(\log a_\varepsilon)^2}\,, \quad \text{where} \quad a_\varepsilon = \frac{8}{\varepsilon d_c}\,, \tag{C.10}$$

which yields (3.11). This completes the derivation of Proposition 5.

Appendix D Large N asymptotics of $\mathcal{S}_N$

In this appendix we establish Lemma 1 for the discrete sum $\mathcal{S}_N$.

Since $\mathcal{S}_N$ is unbounded as $N \to \infty$, we will extract from the sum two terms with known divergent behavior. To do so we define $g(x)$ by

$$g(x) \equiv \frac{1}{\sin(\pi x)} - \frac{1}{\pi x} - \frac{1}{\pi(1-x)}\,, \tag{D.1}$$

so that $g(x)$ is smooth on $0 \le x \le 1$ with removable singularities at $x = 0$ and $x = 1$. By adding and subtracting, and setting $x = j/N$, we then write $\mathcal{S}_N$ in (3.20c) as

$$\mathcal{S}_N = \frac{1}{\pi}\left(N \sum_{j=1}^{N-1} \frac{1}{j} + \sum_{j=1}^{N-1} \frac{1}{1-j/N} \right) + \sum_{j=1}^{N-1} g\left(j/N\right) = \frac{2N}{\pi} H_{N-1} + \sum_{j=1}^{N-1} g\left(j/N\right)\,, \tag{D.2}$$

where H_{N-1} is the $(N-1)$-th harmonic number with the large-N asymptotics (see [25])

$$H_{N-1} \equiv \sum_{j=1}^{N-1} \frac{1}{j} \sim \log(N) + \gamma_e - \frac{1}{2N} - \frac{1}{12N^2} + \mathcal{O}\left(1/N^3\right) \quad \text{as} \quad N \to \infty\,. \tag{D.3}$$

Next, since $g(x)$ is smooth we apply the Euler-Maclaurin summation expansion to obtain

$$\frac{1}{N} \sum_{j=1}^{N-1} g\left(j/N\right) = \int_0^1 g(x)\,\mathrm{d}x - \frac{1}{2N}\left[g(0) + g(1)\right] + \frac{1}{12N^2}\left[g'(1) - g'(0)\right] + \mathcal{O}\left(1/N^3\right)\,, \tag{D.4}$$

as $N \to \infty$. We readily calculate that

$$\int_0^1 g(x)\,\mathrm{d}x = \frac{2}{\pi}\log\left(\frac{2}{\pi}\right)\,, \quad g(0) = g(1) = -\frac{1}{\pi}\,, \quad g'(0) = -g'(1) = \frac{\pi}{6} - \frac{1}{\pi}\,. \tag{D.5}$$

In this way, we obtain from (D.4) and (D.5) that

$$\sum_{j=1}^{N-1} g\left(j/N\right) = \frac{2N}{\pi}\log\left(\frac{2}{\pi}\right) + \frac{1}{\pi} + \left(\frac{1}{6\pi} - \frac{\pi}{36}\right)\frac{1}{N} + \mathcal{O}\left(1/N^2\right) \quad \text{as} \quad N \to \infty\,. \tag{D.6}$$

Upon substituting (D.6) and (D.3) into (D.2) we obtain the limiting asymptotics (3.21) of Lemma 1 as we observe that the $\mathcal{O}(1)$ term vanishes, leaving only an $\mathcal{O}\left(1/N\right)$ error estimate with the small coefficient $-\pi/36$.

Appendix E Ring filament: the lowest eigenvalue of the Laplacian

For the unit sphere, and for $\lambda_0 > 0$ and $j_l'(\sqrt{\lambda_0}) \neq 0$, so that λ_0 is not an eigenvalue of the Laplacian for the filament free-problem in the unit-sphere for radially symmetric eigenfunctions, the regular part of the Helmholtz Green's function in (5.18b) can be obtained from separation of variables as

$$\begin{aligned} R_h(\mathbf{x};\boldsymbol{\xi};\lambda_0) = \frac{1}{4\pi}\sum_{\ell=0}^{\infty}(2\ell+1)\Big[&- \sqrt{\lambda_0}\, j_\ell(\sqrt{\lambda} r_<) y_\ell(\sqrt{\lambda} r_>) + \sqrt{\lambda_0}\frac{y_\ell'(\sqrt{\lambda_0})}{j_\ell'(\sqrt{\lambda_0})} j_\ell(\sqrt{\lambda_0} r) j_\ell(\sqrt{\lambda_0} r_0) \\ &- \frac{r_<^\ell}{(2\ell+1) r_>^{\ell+1}}\Big] P_\ell(\cos\gamma)\,. \end{aligned} \tag{E.1a}$$

Here $j_\ell(x)$ and $y_\ell(x)$ are spherical Bessel functions of the first and second kind of order ℓ, $P_\ell(x)$ is the Legendre polynomial of degree ℓ, and we have labeled

$$r_0 = |\boldsymbol{\xi}|\,, \quad r = |\mathbf{x}|\,, \quad r_< = \min(r, r_0)\,, \quad r_> = \max(r, r_0)\,, \quad \cos\gamma = \frac{\mathbf{x}\cdot\boldsymbol{\xi}}{|\mathbf{x}||\boldsymbol{\xi}|}\,. \tag{E.1b}$$

For an equatorial ring of radius $r_0 < 1$, for which $\mathbf{X}(s) = r_0\,(\cos(s/r_0), \sin(s/r_0), 0)^T$, we use (E.1) in (5.30), after first converting to angular variables, to obtain

$$\begin{aligned} -\log\left(\frac{8r_0}{\varepsilon d_c}\right) &= 2\pi r_0 \int_0^{2\pi} R_h(\mathbf{X}(r_0\theta); \mathbf{X}(r_0\theta'); \lambda_0)\,\mathrm{d}\theta'\,, \\ &= \sum_{\ell=0}^{\infty} \left[\sqrt{\lambda_0} r_0 \left(\ell + \frac{1}{2}\right) H_\ell(\lambda_0, r_0) - \frac{1}{2}\right] \int_0^{2\pi} P_\ell(\cos\psi)\,\mathrm{d}\psi\,, \end{aligned} \tag{E.2}$$

where $H_\ell(\lambda_0, r_0)$ is given in (5.31b) upon replacing l by $2k$. Finally, the integral in (E.2) can be evaluated using an identity in [20]. If ℓ is odd, $\int_0^{2\pi} P_\ell(\cos\psi)\,d\psi = 0$, while if $l = 2k$ and $k = 0, 1, 2, \ldots$, we have

$$\int_0^{2\pi} P_{2k}(\cos\psi)\,\mathrm{d}\psi = 2\pi \left(\frac{(2k)!}{2^{2k}(k!)^2}\right)^2\,. \tag{E.3}$$

Finally, upon substituting (E.3) into (E.2) we conclude that λ_0 must be a root of $\mathcal{N}(\lambda)$ as defined in (5.31).

Appendix F Fragmented filaments: inner problem and numerics

In this appendix we first derive the new inner problem (6.3) in Proposition 9 for a fragmented filament.

Let $\mathbf{X}(s)$ be a smooth simple closed curve of length L parameterized by arclength $s \in [0, L)$ with $\mathbf{X}(0) = \mathbf{X}(L)$, which we discretize into N equal segments with spacing $\triangle s = L/N \ll 1$. At each $s_j = (j-1)L/N$ for $j = 1, \ldots, N$, corresponding to cartesian coordinates $\mathbf{x}_j = \mathbf{X}(s_j)$, we center a microtrap of a common shape Ω_σ and diameter $\mathcal{O}(\sigma) \ll 1$ to generate a fragmented filament. We assume that the collection of microtraps is disjoint.

For any fixed j with $1 < j < N$ (WLOG), the microtrap centered at s_j has two neighbours centered at arclength positions s_{j-1} and s_{j+1}. For this j, we label $s_{j-1/2} = s_j - (\triangle s)/2$ and $s_{j+1/2} = s_j + (\triangle s)/2$. By using Taylor series, the chord distance $|\mathbf{X}(s_{j+1/2}) - \mathbf{X}(s_{j-1/2})|$ for $\triangle s \ll 1$ is

$$|\mathbf{X}(s_{j+1/2}) - \mathbf{X}(s_{j-1/2})| \sim \triangle s - \frac{\kappa_j (\triangle s)^3}{24}\,, \quad \text{for} \quad \triangle s \ll 1\,,$$

where $\kappa_j \equiv |\mathbf{X}''(s_j)|$ is the curvature of $\mathbf{X}(s)$ at $s = s_j$. Upon neglecting the $\mathcal{O}((\triangle s)^3)$ error proportional to the curvature, it follows that the three points $\mathbf{X}(s_j)$, $\mathbf{X}(s_{j+1/2})$ and $\mathbf{X}(s_{j-1/2})$ are all asymptotically colinear for $\triangle s \ll 1$ and so the curve is locally straight.

As a result, we define the unit tangent $\mathbf{t}_Z$ by

$$\mathbf{t}_Z = \frac{\mathbf{X}(s_{j+1/2}) - \mathbf{X}(s_{j-1/2})}{|\mathbf{X}(s_{j+1/2}) - \mathbf{X}(s_{j-1/2})|}\,, \tag{F.1}$$

and we label $\mathcal{P}_j$ to be the 2-D plane orthogonal to $\mathbf{t}_Z$ at $\mathbf{X}(s_j)$. We define two additional planes parallel to $\mathcal{P}_j$ containing $\mathbf{X}(s_{j+1/2})$ and $\mathbf{X}(s_{j-1/2})$ as $\mathcal{P}_{j+1/2}$ and $\mathcal{P}_{j-1/2}$, respectively, where $\mathrm{dist}(\mathcal{P}_{j-1/2}, \mathcal{P}_{j+1/2}) = \triangle s = L/N$. In order to account for the periodicity of the microtraps on the entire curve, we will impose

that the local solution is periodic across these planes. To span the plane $\mathcal{P}_j$ through $\mathbf{X}(s_j)$, we introduce two mutually orthogonal unit vectors $\mathbf{t}_X$ and $\mathbf{t}_Y$.

Next, within an $\mathcal{O}(\sigma)$ neighbourhood of $\mathbf{X}(s_j)$, we introduce the linear transformation

$$\mathbf{x} = \mathcal{L}(X,Y,Z) \equiv \mathbf{X}(s_j) + \sigma X \mathbf{t}_X + \sigma Y \mathbf{t}_Y + \sigma Z \mathbf{t}_Z \,. \tag{F.2}$$

In terms of these local (X,Y,Z) coordinates, the magnified microtrap centered at $(X,Y,Z) = (0,0,0)$ is Ω_0 and has diameter $\mathcal{O}(1)$. In addition, the images of the planes $\mathcal{P}_{j+1/2}$ and $\mathcal{P}_{j-1/2}$ correspond to $Z = a$ and $Z = -a$ respectively, where $a \equiv (\triangle s)/(2\sigma) = L/(2N\sigma)$. Upon labeling the local solution by $V(X,Y,Z) \equiv u\left(\mathcal{L}(X,Y,Z)\right)$, (6.1) transforms to $\Delta V = -\sigma^2/D$, so that to leading-order $V \sim V_0$ where V_0 is harmonic in the slab geometry $|Z| \leq a$, $-\infty < X,Y < \infty$ with V_0 having periodic boundary conditions on $Z = \pm a$. For each Z, we impose that $V_0 \sim A(s_j)\log\rho$ as $\rho \equiv \sqrt{X^2+Y^2} \to \infty$, where $A(s_j)$ is the local line density evaluated at $s = s_j$, which is determined by the outer problem. In this way, by introducing V_c by $V_0 = A(s_j)V_c$, we obtain that V_c satisfies the new canonical inner problem (6.3) with unit logarithhmic growth for which $V_c \sim \log\rho + \omega + o(1)$ as $\rho \to \infty$ for some *infinite slab capacitance* $\omega = \omega(a)$ to be determined.

In terms of the outer variable $\mathbf{x}$, we use (F.2) to estimate for a fixed Z that $\log|\mathbf{x} - \mathbf{X}(s_j)| = \log\rho + \log\sigma + \mathcal{O}\left(Z^2/(2\rho^2)\right)$ as $\rho \to \infty$, so that the asymptotic matching condition to the outer solution becomes

$$V_0 = A(s_j)V_c \sim A(s_j)\log|\mathbf{x} - \mathbf{X}(s_j)| + A(s_j)\left(\omega - \log\sigma\right) \,, \quad \text{as} \quad \mathbf{x} \to \mathbf{X}(s_j) \,. \tag{F.3}$$

Upon equating the far-field behavior (F.3) with the similar matching condition (2.5) for a perfectly absorbing filament of cross-sectional radius ε, we simply enforce $1/\nu = \omega - \log\sigma$ where $\nu = -1/\log[\varepsilon d_c]$ with $d_c = 1$. Solving this expression for ε gives (6.2). With this choice the outer problems for the fragmented and unfragmented filaments are exactly the same, and consequently have the same average MFRT to all logarithmic orders. To treat fragmented filaments we need only replace $\varepsilon = \sigma e^{-\omega}$ in the integral equation (2.19).

F.1 Large-a asymptotics of the new inner problem

Finally, although for general $a = \mathcal{O}(1)$ we must compute $\omega(a)$ numerically from the solution to (6.3) (see below) we now establish the asymptotics (6.4) for $a \gg 1$. This range corresponds to the transition region $\mathcal{O}(\sigma) \ll L/N \ll \mathcal{O}(1)$.

For $a \to \infty$, the boundaries of the slab tend to infinity, and so (6.3) can be solved asymptotically by inner-outer matching. In the inner region near the microtrap Ω_0 the leading-order asymptotic solution is $V_c \sim B\left(1 - w_c\right)$ for some constant B, where w_c solves (3.15). Using the far-field behavior of w_c in (3.15), we obtain that

$$V_c \sim B - \frac{BC}{d} \,, \quad \text{as} \quad d \equiv \sqrt{X^2+Y^2+Z^2} \to \infty \,, \tag{F.4}$$

where C is the capacitance of Ω_0. For the outer region, for $a \gg 1$ we introduce the stretched coordinate $\mathbf{x} = (x,y,z)^T = (X,Y,Z)^T/a$ so that the effect of the microtrap is a point singularity (here $\mathbf{x}$ is a local variable distinct from the $\mathbf{x}$ in the outer region). After matching to (F.4), the outer solution, labeled by $v(\mathbf{x})$ is

$$v(\mathbf{x}) \sim -4\pi B \frac{C}{a} g(\mathbf{x}) + B \,, \tag{F.5}$$

where $g(\mathbf{x})$ is the unique slab Green's function satisfying

$$\begin{aligned} \Delta g = 0\,, \quad |z| < 1\,, \quad -\infty < x, y < \infty\,, \\ g(x,y,1) = g(x,y,-1)\,, \quad g_z(x,y,1) = g_z(x,y,-1)\,, \\ g(\mathbf{x}) = \frac{1}{4\pi|\mathbf{x}|} + o(1)\,, \quad \text{as} \quad |\mathbf{x}| \to 0\,. \end{aligned} \tag{F.6}$$

The uniqueness follows from the $o(1)$ condition as $|\mathbf{x}| \to 0$.

Defining $r \equiv (x^2+y^2)^{1/2}$, the solution to (F.6) has the form $g = g(r,z)$. The far-field asymptotics of $g(r,z)$, established below in Lemma 3, is

$$g(r,z) \sim -\frac{1}{4\pi}\log r + \frac{1}{4\pi}\left(\log(4) - \gamma_e\right)\,, \quad \text{as} \quad r = \sqrt{x^2+y^2} \to \infty\,, \tag{F.7}$$

for each z in $|z| \le 1$. Substituting (F.7) into (F.5), and replacing $r = \rho/a$, we have the following far-field behavior for any fixed $Z = z/a$:

$$V_c \sim \frac{BC}{a}\log\rho + \frac{BC}{a}\left(-\log(4a) + \gamma_e\right) + B\,, \quad \text{as} \quad \rho = \sqrt{X^2+Y^2} \to \infty\,. \tag{F.8}$$

Upon comparing (F.8) with the target far-field behavior in (6.3) we must have $B = a/C$ and $\omega \sim -\log(4a) + \gamma_e + a/C$ as $a \to \infty$. This confirms (6.4) and completes the derivation of Proposition 9.

Our final step is to derive (F.7) for the slab Green's function satisfying (F.6). This Green's function provides the canonical connection between 2-D and 3-D.

Lemma 3. *For $r = \sqrt{x^2+y^2} \to \infty$, the asymptotics* (F.7) *for the solution to* (F.6) *holds for any fixed $|z| \le 1$.*

Proof. Define $\mathbf{e}_z = (0,0,1)^T$. By using the method of images, g can be represented as

$$g(\mathbf{x}) = \frac{1}{4\pi}\frac{1}{|\mathbf{x}|} + \frac{1}{4\pi}\sum_{|k|>0}^{\infty}\left(\frac{1}{|\mathbf{x}-2k\mathbf{e}_z|} - \frac{1}{2|k|}\right)\,. \tag{F.9}$$

By substracting the constant $\frac{1}{2|k|}$ off of each image term, the resulting function automatically satisfies the $o(1)$ condition at the origin in (F.6). Moreover this sum is well defined, since $\frac{1}{|\mathbf{x}-2k\mathbf{e}_z|} - \frac{1}{2|k|} = \mathcal{O}(k^{-2})$ as $k \to \infty$ for any fixed $\mathbf{x}$.

We now determine the far-field behaviour. Suppose first that $z = 0$. We then write (F.9) as

$$4\pi g(\mathbf{x}) = \frac{1}{r} + 2S\,, \tag{F.10}$$

where S is defined by

$$S = \lim_{K\to\infty}\left(\sum_{k=1}^{K}\frac{1}{\sqrt{r^2+4k^2}} - \sum_{k=1}^{K}\frac{1}{2k}\right)\,. \tag{F.11}$$

By using

$$\sum_{1}^{K}\frac{1}{k} = \log K + \gamma_e + \mathcal{O}(K^{-1})\,,$$

we rewrite (F.11) as

$$S = \lim_{K\to\infty}\left(\sum_{k=1}^{K}\frac{1}{\sqrt{r^2+4k^2}} - \frac{1}{2}\log K\right) - \frac{\gamma_e}{2}\,. \tag{F.12}$$

For large r on the range $\mathcal{O}(1) \ll r \ll \mathcal{O}(K)$, we introduce $\triangle\xi = 2/r \ll 1$ and $\xi_k = 2k/r$, to obtain

$$\sum_{k=1}^{K} \frac{1}{\sqrt{r^2+4k^2}} = \frac{1}{2}\sum_{k=1}^{K} \frac{\triangle\xi}{\sqrt{1+\xi_k^2}}\,. \tag{F.13}$$

In terms of the right Riemann sum we identify that

$$\lim_{r\to\infty}\left(\frac{1}{2}\sum_{k=1}^{K}\frac{\triangle\xi}{\sqrt{1+\xi_k^2}}\right) = \frac{1}{2}\int_0^{2K/r}\frac{\mathrm{d}\xi}{\sqrt{1+\xi^2}} = \frac{1}{2}\log\left(\xi+\sqrt{1+\xi^2}\right)\Big|_0^{2K/r} \sim \frac{1}{2}\log\left(\frac{4K}{r}\right)+o(1)\,, \tag{F.14}$$

when $\mathcal{O}(1) \ll r \ll \mathcal{O}(K)$. Upon substituting (F.14) into (F.12) we obtain for $r \gg 1$ that

$$S \sim \lim_{K\to\infty}\left(\frac{1}{2}\log K + \log 2 - \frac{1}{2}\log r - \frac{1}{2}\log K + o(1)\right) - \frac{\gamma_e}{2} \sim -\frac{1}{2}\log r + \log 2 - \frac{\gamma_e}{2}\,. \tag{F.15}$$

Finally, by using (F.15) in (F.10), we obtain the limiting behavior for g in (F.7).

We remark that since we are taking the limit of large r, this derivation remains unaltered even if z is non-zero since $|z| < 1 \ll r$. □

F.2 Numerics of $\omega(a)$.

We used the MATLAB PDE Toolbox (quadratic finite elements) to solve (6.3). For both the disk and the ball, axial symmetry then reduces (6.3) to a two-dimensional problem in the cylindrical coordinates (ρ, Z), with $\rho = \sqrt{X^2+Y^2}$, on the truncated half-strip $0 < \rho < \rho_{\max}$, $0 < Z < a$, where we solve $\nabla\cdot(\rho\nabla V_c) = 0$. For the disk, $V_c = 0$ on $0 < \rho < 1$, $Z = 0$; for the ball, the quarter disk $\rho^2 + Z^2 < 1$ is removed and $V_c = 0$ on the arc $\rho^2 + Z^2 = 1$. On the far boundary $\rho = \rho_{\max}$ we impose the unit flux $\rho\,\partial_\rho V_c = 1$ and homogeneous Neumann conditions on the remaining boundaries. Note that the Z-average $\bar{V}(\rho) \equiv a^{-1}\int_0^a V_c\,dZ$ satisfies $(\rho\bar{V}')' = 0$ exactly and therefore matches the far-field behaviour $\bar{V} \sim \log\rho + \omega$. We therefore read off $\omega = \bar{V}(\rho_{\max}) - \log\rho_{\max}$. We used $\rho_{\max} = 1 + 4a$. Halving the mesh size changed ω by at most 2×10^{-6} (ball) and 6×10^{-5} (disk). Doubling $\rho_{\max}$ changed ω by less than 10^{-7}.

Table 9 compares $\omega(a)$, computed numerically from (6.3) as described above, with the large-a asymptotics (6.4).

ball ($C=1$)			disk ($C=2/\pi$)		
a	$\omega(a)$	ω_{asym}	a	$\omega(a)$	ω_{asym}
1.05	0.1376	0.1921	0.25	0.1171	0.9699
1.10	0.1501	0.1956	0.50	0.2524	0.6695
1.25	0.1913	0.2178	1.00	0.6059	0.7617
1.50	0.2741	0.2855	1.50	1.0633	1.1417
2.00	0.4950	0.4978	2.00	1.5930	1.6394
3.00	1.0919	1.0923	3.00	2.7832	2.8047
5.00	2.5815	2.5815	5.00	5.4275	5.4355

Table 9: The infinite slab capacitance $\omega(a)$ of (6.4), computed by finite elements, compared with the large-a asymptotics $\omega_{\text{asym}} = a/C - \log(4a) + \gamma_e$ from (6.3), for a unit ball and a flat unit disk. The numerical values are accurate to all digits shown.

The agreement is excellent for large a. The asymptotic formula converges very fast for a ball, with a relative error of only 0.56% at $a = 2$. As expected, the convergence is slower for a disk, with a relative error of 2.9% at $a = 2$.

References

[1] B. K. Alpert. Hybrid Gauss-trapezoidal quadrature rules. *SIAM J. Sci. Comput.*, 20(5):1551–1584, 1999.

[2] G. K. Batchelor. Slender-body theory for particles of arbitrary cross-section in Stokes flow. *J. Fluid Mech.*, 44:419–440, 1970.

[3] A. J. Bernoff and A. E. Lindsay. Numerical approximation of diffusive capture rates by planar and spherical surfaces with absorbing pores. *SIAM J. Appl. Math.*, 78(1):266–290, 2018.

[4] A. J. Bernoff and A. E. Lindsay. Kinetic Monte Carlo methods for three-dimensional diffusive capture problems in exterior domains. *Royal Soc. Open Sci.*, 12(2):241033, 2025.

[5] R. L. Bishop. There is more than one way to frame a curve. *The American Mathematical Monthly*, 82(3):246–251, 1975.

[6] P. C. Bressloff. Cellular diffusion processes in singularly perturbed domains. *J. Math. Biol.*, 89(6):58, 2024.

[7] P. C. Bressloff. Asymptotic analysis of the 2d narrow-capture problem for partially accessible targets. *SIAM J. Appl. Math.*, 85(5):2122–2144, 2025.

[8] P. C. Bressloff and J. M. Newby. Stochastic models of intracellular transport. *Rev. Mod. Phys.*, 85:135–196, 2013.

[9] P. C. Bressloff and R. D. Schumm. The narrow capture problem with partially absorbing targets and stochastic resetting. *Multiscale Model. Simul.*, 20(2):857–881, 2022.

[10] L. Bundrock, A. Girouard, D. S. Grebenkov, M. Levitin, and I. Polterovich. The exterior Steklov problem for Euclidean domains. *J. Spect. Th., accepted; preprint is available arXiv:2511.09490*, 2025.

[11] A. Chaigneau and D. S. Grebenkov. A numerical study of the generalized Steklov problem in planar domains. *J. Phys. A: Math. Theor.*, 57:445201, 2024.

[12] S. Chakraborty, J. G. Hoskins, and A. E. Lindsay. High-order integral methods for the Neumann Green's function: applications to capture and signaling problems in two dimensions, 2025.

[13] A. Cheviakov and M. J. Ward. Optimizing the principal eigenvalue of the Laplacian in a sphere with interior traps. *Math. Comp. Model.*, 53(7-8):1394–1409, 2011.

[14] T. Chou and M. R. D'Orsogna. First passage problems in biology. In *First-passage phenomena and their application*, pages 306–345. World Scientific, Singapore, 2014.

[15] M. Ciocanel, J. A. Kreiling, J. A. Gagnon, K. L. Mowry, and B. Sandstede. Analysis of active transport by fluorescence recovery after photobleaching. *Biophys. J.*, 112(8):1714–1725, 2026/10/12 2017.

[16] D. Coombs, R. Straube, and M. J. Ward. Diffusion on a sphere with localized traps: Mean first passage time, eigenvalue asymptotics, and Fekete points. *SIAM J. Appl. Math.*, 70(1):302–332, 2009.

[17] G. Dahlquist and A. Björck. *Numerical Methods*. Prentice-Hall, Englewood Cliffs, NJ, 1974. Translated from the Swedish 'Numeriska metoder'.

[18] U. Dobramysl and D. Holcman. Mixed analytical-stochastic simulation method for the recovery of a Brownian gradient source from probability fluxes to small windows. *J. Comput. Phys.*, 355:22 – 36, 2018.

[19] M. R. D'Orsogna, A. E. Lindsay, and T. Hillen. Mean first passage times of higher-dimensional velocity jump processes. *Phys. Rev. Lett.*, 136:247102, Jun 2026.

[20] A. Erdélyi, W. Magnus, F. Oberhettinger, and F. G. Tricomi. *Higher Transcendental Functions*, volume 1. McGraw-Hill, New York, 1953.

[21] P. W. Fok and T. Chou. Accelerated search kinetics mediated by redox reactions of DNA repair enzymes. *Biophys. J.*, 96:3949—-3958, 2009.

[22] C. Geuzaine and J.-F. Remacle. Gmsh: A 3-d finite element mesh generator with built-in pre- and post-processing facilities. *Inter. J. Numer. Methods Eng.*, 79(11):1309–1331, 2009.

[23] I. G. Gjerde, K. Kumar, and J. M. Nordbotten. A mixed approach to the Poisson problem with line sources. *SIAM J. Numer., Anal.*, 59(2):117–1139, 2021.

[24] I. G. Gjerde, K. Kumar, J. M. Nordbotten, and B. Wohlmuth. Splitting method for elliptic equations with line sources. *ESAIM: Math. Model. Numer. Anal.*, 53(5):1715–1739, 2019.

[25] R. L. Graham, D. E. Knuth, and O. Patashnik. *Concrete Mathematics: A Foundation for Computer Science*. Addison-Wesley Professional, Boston, MA, 2nd edition, 1994.

[26] D. S. Grebenkov. Steklov-Neumann spectral problem: asymptotic analysis and applications to diffusion-controlled reactions. *Multi. Model. Simul.*, 23:1607–1664, 2025.

[27] D. S. Grebenkov and A. Chaigneau. The Steklov problem for exterior domains: asymptotic behavior and applications. *J. Math. Phys.*, 66:061502, 2025.

[28] D. S. Grebenkov, R. Metzler, and G. Oshanin, editors. *Target Search Problems*. Springer Nature Switzerland, Cham, 2024.

[29] D. S. Grebenkov and G. Oshanin. Diffusive escape through a narrow opening: new insights into a classic problem. *Phys. Chem. Chem. Phys.*, 19:2723–2739, 2017.

[30] D. S. Grebenkov and M. J. Ward. Competition of small targets in planar domains: from Dirichlet to Robin and Steklov boundary condition. *Eur. J. Appl. Math.*, 37:1244–1291, 2026.

[31] R. A. Handelsman and J. B. Keller. Axially symmetric potential flow around a slender body. *J. Fluid Mech.*, 28:131–147, 1967.

[32] E. W. Hester and G. M. Vasil. Orthogonal signed-distance coordinates and vector calculus near evolving curves and surfaces. *Proc. Roy. Soc. A*, 479(2277):20230080, 2023.

[33] T. Hillen, M.R. D'Orsogna, J. C. Mantooth, and A. E. Lindsay. Mean first passage times for transport equations. *SIAM J. Appl. Math.*, 85(1):78–108, 2026/10/12 2025.

[34] D. Holcman and Z. Schuss. Escape through a small opening: Receptor trafficking in a synaptic membrane. *J. Stat. Phys.*, 117(5-6):975–1014, 2004.

[35] D. Holcman and Z. Schuss. Time scale of diffusion in molecular and cellular biology. *J. of Physics A: Math. and Theor.*, 47(17):173001, 2014.

[36] S. Kapur and V. Rokhlin. High-order corrected trapezoidal quadrature rules for singular functions. *SIAM J. Numer. Anal.*, 34(4):1331–1356, 1997.

[37] J. B. Keller and S. I. Rubinow. Slender-body theory for slow viscous flow. *J. Fluid Mech.*, 75:705–714, 1976.

[38] H. Kim, Y. Mori, and J. B. Plotkin. Optimality of intercellular signaling: Direct transport versus diffusion. *Phys. Rev. E*, 106:054411, Nov 2022.

[39] L. Koens and E. Lauga. The boundary integral formulation of Stokes flows includes slender-body theory. *J. Fluid Mech.*, 850:R1, 2018.

[40] T. Kolokolnikov, M. S. Titcombe, and M. J. Ward. Optimizing the fundamental Neumann eigenvalue for the Laplacian in a domain with small traps. *Europ. J. Appl. Math.*, 16:161–200, 4 2005.

[41] V. Kurella, J. C. Tzou, D. Coombs, and M. J. Ward. Asymptotic analysis of first passage time problems inspired by ecology. *Bull. Math. Biol.*, 77(1):83–125, 2015.

[42] S. D. Lawley. Channel transport: Gating, geometry, and heterogeneous diffusion. *Bull. Math. Biol.*, 88(6):100, 2026.

[43] S. D. Lawley, A. E. Lindsay, and C. E. Miles. Receptor organization determines the limits of single-cell source location detection. *Phys. Rev. Lett.*, 125:018102, Jul 2020.

[44] A. E. Lindsay, A. J. Bernoff, T. Goodwill, and J. G. Hoskins. The three dimensional Neumann Green's function for general surfaces: singular asymptotics and boundary integral methods, 2026.

[45] A. E. Lindsay, A. J. Bernoff, and A. Navarro Hernández. Short-time diffusive fluxes over membrane receptors yields the direction of a signalling source. *Royal Soc. Open Sci.*, 10(4):221619, 2023.

[46] A. E. Lindsay, T. Kolokolnikov, and J. C. Tzou. Narrow escape problem with a mixed trap and the effect of orientation. *Phys. Rev. E*, 91:032111, Mar 2015.

[47] O. Maxian and A. Donev. A simulation platform for slender, semiflexible, and inextensible fibers with brownian hydrodynamics and steric repulsion. *Physics of Fluids*, 36(12):123320, 12 2024.

[48] H. W. McKenzie, E. H. Merrill, R. J. Spiteri, and M. A. Lewis. How linear features alter predator movement and the functional response. *Interface Focus*, 2:205–216, 2012.

[49] P. J. Mlynarczyk and S. M. Abel. First passage of molecular motors on networks of cytoskeletal filaments. *Phys Rev E*, 99(2-1):022406, Feb 2019.

[50] Y. Mori, L. Ohm, and D. Spirn. Theoretical justification and error analysis for slender body theory with free ends. *Arch. Ration. Mech. Anal.*, 235(3):1905–1978, 2020.

[51] P. Nayak, S. Chatterjee, and R. Paul. Microtubule search-and-capture model evaluates the effect of chromosomal volume conservation on spindle assembly during mitosis. *Phys. Rev. E*, 108:034401, Sep 2023.

[52] J. M. Newby and P. C. Bressloff. Directed intermittent search model of microtubule cargo transport. *BMC Neuroscience*, 10(1):P24, 2009.

[53] L. Ohm. On an angle-averaged Neumann-to-Dirichlet map for thin filaments. *Arch. Ration. Mech. and Anal.*, 249(1):8, 2024.

[54] L. Ohm and S. Strikwerda. A hierarchy of blood vessel models, Part II: 3D-3D to 3D-1D and 1D, 2025.

[55] S. Pillay, M. J. Ward, A. Peirce, and T. Kolokolnikov. An asymptotic analysis of the mean first passage time for narrow escape problems: Part I: Two-dimensional domains. *Multiscale Model. Simul.*, 8(3):803–835, 2010.

[56] C. E. Plunkett and S. D. Lawley. Boundary homogenization for patchy surfaces trapping patchy particles. *J. Chem. Phys.*, 158(9):094104, 03 2023.

[57] S. Redner. *A Guide to First-Passage Processes*. Cambridge University Press, 2001.

[58] M. J. Ward, W. Henshaw, and J. B. Keller. Summing logarithmic expansions for singularly perturbed eigenvalue problems. *SIAM J. Appl. Math.*, 53(3):799–828, 1993.